

Scuola di Scienze  
Corso di Laurea Magistrale in Fisica

**MR spectroscopy in human prostate: in vitro and  
in vivo measurements to optimize new  
quantification algorithms**

**Relatore:**

**Prof. Romano Zannoli**

**Presentata da:**

**Giovanni Bellomo**

**Correlatore:**

**Dott. David Bianchini**

**Dott. Francesco Marcocci**

**Sessione II**

**Anno Accademico 2014/2015**



*A mio padre, per tutte le risposte date ai miei perché e per essere sempre stato un  
esempio di coraggio e gentilezza.*

*A mia madre, per avermi insegnato i valori dell'onestà e del duro lavoro e per essermi  
sempre stata accanto nei momenti più difficili.*



## Abstract

Il cancro della prostata (PCa) è il tumore maligno non-cutaneo più diffuso tra gli uomini ed è il secondo tumore che miete più vittime nei paesi occidentali. La necessità di nuove tecniche non invasive per la diagnosi precoce del PCa è aumentata negli anni.  $^1\text{H}$ -MRS (proton magnetic resonance spectroscopy) e  $^1\text{H}$ -MRSI (proton magnetic resonance spectroscopy imaging) sono tecniche avanzate di spettroscopia in risonanza magnetica che permettono di individuare presenza di metaboliti come citrato, colina, creatina e in alcuni casi poliammine in uno o più voxel nel tessuto prostatico. L'abbondanza o l'assenza di uno di questi metaboliti rende possibile discriminare un tessuto sano da uno patologico. Le tecniche di spettroscopia RM sono correntemente utilizzate nella pratica clinica per cervello e fegato, con l'utilizzo di software dedicati per l'analisi degli spettri. La quantificazione di metaboliti nella prostata invece può risultare difficile a causa del basso rapporto segnale/rumore (SNR) degli spettri e del forte accoppiamento-j del citrato. Lo scopo principale di questo lavoro è di proporre un software prototipo per la quantificazione automatica di citrato, colina e creatina nella prostata. Lo sviluppo del programma e dei suoi algoritmi è stato portato avanti all'interno dell'IRST (Istituto Romagnolo per lo Studio e la cura dei Tumori) con l'aiuto dell'unità di fisica sanitaria. Il cuore del programma è un algoritmo iterativo per il fit degli spettri che fa uso di simulazioni MRS sviluppate con il pacchetto di librerie GAMMA in C++. L'accuratezza delle quantificazioni è stata testata con dei fantocci realizzati all'interno dei laboratori dell'istituto. Tutte le misure spettroscopiche sono state eseguite con il nuovo scanner Philips Ingenia 3T, una delle macchine di risonanza magnetica più avanzate per applicazioni cliniche. Infine, dopo aver eseguito i test in vitro sui fantocci, sono stati acquisiti gli spettri delle prostate di alcuni volontari sani, per testare se il programma fosse in grado di lavorare in condizioni di basso SNR.

## Abstract

Prostate cancer (PCa) is the most common non-cutaneous cancer in male subjects and the second leading cause of cancer-related death in western countries. The necessity of a non-invasive technique for a diagnosis of PCa in early stage has grown through years.  $^1\text{H}$ -MRS ((proton magnetic resonance spectroscopy) and  $^1\text{H}$ -MRSI (proton magnetic resonance spectroscopy imaging) are advanced magnetic resonance techniques that can mark the presence of metabolites such as citrate, choline, creatine and polyamines in a selected voxel, or in an array of voxels in MRSI inside prostatic tissue. Abundance or lack of some of these metabolites can discriminates between pathological and healthy tissue. Although the use of MRS is well established in brain and liver with dedicated software for spectral analysis, quantification of metabolites in prostate can be very difficult to achieve, due to poor signal to noise ratio and strong j-coupling of the citrate. The main aim of this work is to submit a software prototype for automatic quantification of citrate, choline and creatine in prostate. The development of this software was carried out at IRST (Istituto Romagnolo per lo Studio e la cura dei Tumori) with the help of the medical physics unit. The core of the program is an iterative fitting routine that makes use of MRS simulations developed with the GAMMA libraries in C++. The accuracy of the quantifications was tested on homemade phantoms, manufactured in the biological laboratories of the research institute. All the measurements were performed with the new Philips Ingenia 3T, one of the most advanced MR scanner for clinical applications. Finally, we performed acquisitions on healthy volunteers to test the ability of the program to work in low SNR conditions.

# CONTENTS

<b>INTRODUCTION</b> .....	<b>1</b>
<b>1 THEORY OF MRS</b> .....	<b>5</b>
1.1 CLASSICAL EXPLANATION OF MAGNETIC RESONANCE.....	5
1.2 CHEMICAL SHIELDING .....	9
1.3 QUANTUM MECHANICAL TREATMENT OF MRS .....	12
1.3.1 <i>Chemical shift Hamiltonian</i> .....	16
1.3.2 <i>J-Coupling</i> .....	18
1.3.3 <i>Weak coupling approximation and first-order spectra</i> .....	21
1.3.4 <i>Strong coupling</i> .....	23
1.4 DENSITY MATRIX FORMALISM.....	25
1.4.1 <i>One spin system</i> .....	28
1.4.2 <i>Two spins</i> .....	30
1.4.3 <i>Two spins Product Operators</i> .....	36
1.5 RELAXATION.....	38
1.5.1 <i>Spin-lattice relaxation</i> .....	38
1.5.2 <i>Spin-spin relaxation</i> .....	40
1.6 HOW THE SPECTROMETER WORKS .....	43
1.6.1 <i>Magnet and shim coils</i> .....	43
1.6.2 <i>Spectrometer frequency</i> .....	44
1.6.3 <i>Receiver and quadrature detection</i> .....	45
1.6.4 <i>Spectral width and resolution</i> .....	45
1.7 GENERAL DESCRIPTION OF PULSE SEQUENCES.....	47
1.7.1 <i>Localization pulses and gradients</i> .....	47
1.7.2 <i>STimulated Echo Acquisition Mode (STEAM)</i> .....	47
1.7.3 <i>Point REsolved Spectroscopy Sequence (PRESS)</i> .....	48
1.7.4 <i>CHEmical Shift Selective Sequence (CHESS)</i> .....	50

1.7.5 <i>BASING pulse</i> .....	50
1.7.6 <i>Other important parameters in pulse sequences</i> .....	51
<b>2 MATERIALS AND METHODS</b> .....	<b>53</b>
2.1 THE SPECTROMETER.....	53
2.1.1 <i>Scanner Philips Ingenia 3T</i> .....	54
2.2 SOFTWARE FOR SPECTRAL ANALYSIS .....	58
2.2.1 <i>Existing software solutions taken into account</i> .....	58
2.3 DEDICATED SOFTWARE DEVELOPMENT .....	62
2.3.1 <i>Input</i> .....	63
2.3.2 <i>Minimization of the cost function</i> .....	65
2.3.4 <i>Output</i> .....	70
2.4 HOME-MADE PHANTOMS .....	72
2.4.1 <i>Water phantoms with paramagnetic agent</i> .....	72
2.4.2 <i>Phantoms with metabolites</i> .....	73
2.5 SEQUENCES USED .....	77
2.5.1 <i>Sequences used for phantom quantifications</i> .....	77
2.5.2 <i>Sequences used for in vivo acquisitions</i> .....	80
<b>3 RESULTS</b> .....	<b>82</b>
3.1 IN VITRO TESTS ON HOMEMADE PHANTOMS .....	82
3.1.1 <i>Measure of the <math>T_2</math> of water with paramagnetic agent <math>CuSO_4</math></i> .....	82
3.1.2 <i>In vitro estimation of citrate spectral parameters</i> .....	83
3.1.3 <i>Measure of the <math>T_2</math> of metabolites in homemade phantoms</i> .....	85
3.1.4 <i>Quantification of metabolites in homemade phantoms with homemade software</i> .....	88
3.1.5 <i>Quantification of metabolites in homemade phantoms with AMARES</i> .....	96
3.2 IN VIVO TESTS ON HEALTHY VOLUNTEERS.....	100
3.2.1 <i>Assessing the SNR ratio</i> .....	100
3.2.2 <i>Measure of the in vivo parameters of citrate</i> .....	104



3.3.3 <i>Fit of in vivo prostate spectra</i> .....	105
<b>4 CONCLUSIONS</b> .....	<b>114</b>
<b>BIBLIOGRAPHY</b> .....	<b>117</b>
<b>RINGRAZIAMENTI</b> .....	<b>122</b>

# INTRODUCTION

Prostate cancer (PCa) is the most common non-cutaneous cancer in male subjects and the second leading cause of cancer-related death in western countries (1). New techniques for detecting PCa at an early stage without invasive methods involve the use of proton MR spectroscopy ( $^1\text{H-MRS}$ ) and Magnetic Resonance Spectroscopy Imaging (MRSI). Quantification of metabolites such as citrate, choline, creatine and even polyamines with MR spectroscopy showed good sensitivity and specificity for the diagnosis of PCa (2) (3) (4). In particular the ratio between their concentrations ( $\text{choline}[\ ] + \text{creatine}[\ ] / \text{citrate}[\ ]$ ) or the much simpler  $\text{choline}[\ ] / \text{citrate}[\ ]$  are the variables of clinical interest because of their correlation with the Gleason score (5), which is a grading system used to assess the aggressiveness of PCa from the biopsy of the prostate (6).

- Citrate (Cit) is the main product of prostate epithelial cells and one of the main components of prostatic fluid (7), it is involved in the physiological activity of the prostate. In PCa, a decrease in zinc levels leads to activation of m-aconitase with ensuing oxidation of citrate (8).
- Choline (Cho) and choline-containing compounds are involved in the phospholipid metabolism and higher levels of choline are found in PCa due to increased cellular membrane production in the cancerous tissue (9).
- Creatine (Cr) and phosphocreatine, which are seen at the same peaks in  $^1\text{H-MRS}$  with common clinical spectrometers ( $B_0 \leq 3T$ ), have the function of regulating ATP production (10), no significant differences are observed in normal and cancerous tissue, but it is common practice to consider Cr in MRS analysis to use it as a reference compound.
- Spermine, which is the most common polyamine in prostate tissue, plays a role in prostatic growth and differentiation (11). Decrease of polyamines in prostatic tissue occurs in PCa (11). Although it is not always possible to detect polyamines using clinical spectrometers, their quantification is the target of the most recent clinical MRS researches on PCa.

<sup>1</sup>H-MRS in Brain and Liver is well established and software like JMRui (12), LCModel (13), SpectroView (Philips Healthcare) and Tarquin (14) are commonly used in clinical practice. Diagnostics using <sup>1</sup>H-MRS of PCa in prostate is quite difficult at the moment because of the poor Signal to Noise Ratio (SNR) of MRSI, due to the presence of rectum next to the shimming volume. The absence of a dedicated software for the spectrum analysis makes MRS quantification in Prostate not well suited for clinical practice, although JMrui (15) and LCModel (16) provide features and tools for simulation that fit the purpose. Moreover, due to the poor SNR and to lipid contamination, quantification with short echo time sequences, such as Stimulated Echo Acquisition Mode (STEAM), sequence is difficult to achieve (15). Consequently, to achieve an SNR greater than STEAM, Point Resolved Spectroscopy (PRESS) with higher echo times should be used. The hydrogen nuclei of the two magnetically equivalent methylene groups of Cit are strongly coupled, evolution of the system for long echo times leads to a significant j-coupling modulation of the signal; moreover both the chemical shift frequencies and the j-coupling constant depend on pH and cation concentration in the tissue (17). All this variability in the shape of Cit spectrum is difficult to manage with the software available for clinical practice and a rigorous quantum mechanical treatment must be used to predict the correct line-shape, in function of j-coupling and echo time used, to correctly fit the spectrum. Spermine is a coupled spin system and, in addition to its amine groups, contains 10 methylene groups. These methylene protons consist of symmetrical pairs that produce a wired NMR spectrum due to j-coupling between them. Complex line-shape spectrum, low resolution at clinically used magnetic fields, conspicuous number of resonating hydrogens, j-coupling constants and chemical shifts parameters (18), make the quantification of spermine and other polyamines among the most difficult tasks of research in MRS for PCa diagnosis.

The main aim of this work is the development of an algorithm for an accurate quantification of citrate, choline and creatine and the ratio  $\frac{Cho+Cr}{Cit}$  in prostatic tissue that makes use of prior knowledge of the spin system associated with the chemical groups of metabolites with rigorous quantum mechanical calculations. The research and the experiments made to quantify the spectra of the metabolites led to the construction of a homemade software for automatic analysis of the NMR spectroscopy signals (see Fig. 1). To assess the goodness of fits and quantifications, several tests on homemade phantoms

and healthy volunteers were performed by the Unit of Medical Physics of the IRST center, comparing the results with those obtained using other software.

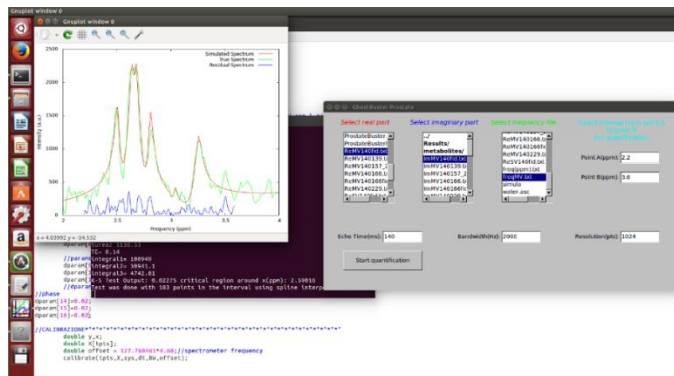


Fig. 1: Screenshot of the homemade quantification software during a quantification.

This work is structured as follows:

1. In chapter one are described some important aspects of magnetic resonance theory, focusing on spectroscopy applications. MR theory is treated starting from a classical view of magnetic resonance until the development of the density matrix formalism. This part of the work has been crucial for the development of the algorithms of the homemade software because density matrices are used in the program to manage metabolites spectra. Some general notions of how a common spectrometer works and a description of the sequences used in common clinical spectrometers are also provided. The reader who is not interested in theory or is already familiar with magnetic resonance spectroscopy can skip this part.
2. In chapter two all the information is provided about the materials used to build and measure the phantoms, the pulse sequences used and the general features of the spectrometer Philips Ingenia 3T. In this chapter there is also a description of the homemade software and some algorithms of the jMRui package.
3. Results of the measurements on phantoms and on two healthy volunteers are showed in chapter 3. First of all, Spectral parameters of citrate were evaluated from phantoms and from in vivo spectra using theory developed in chapter 1, then we measured correction factors for transverse relaxation. Finally the quantities measured with the homemade software were compared with the real molarities of

the metabolites inside the phantoms; the same analysis was done using jMRui for comparison. In the last part of chapter 3 the fitting capabilities of the homemade program was tested on in vivo spectra with low SNR, and then compared with AMARES and QUEST (two algorithms of the jMRui package).

4. Chapter 4 contains the overall considerations on the results shown in chapter 3, their limitations and the prospective for future developments.

# 1 THEORY OF MRS

## 1.1 CLASSICAL EXPLANATION OF MAGNETIC RESONANCE

In a classical way, we can imagine a system of atomic nuclei with a total magnetization  $\mathbf{M}$ . This magnetization vector is the average nuclear magnetic dipole momentum inside an ensemble of nuclei, so it is made by considering the magnetic dipole momentum of all the atom species in the volume. So, for simplicity, let's consider a single nucleus with a nuclear magnetic dipole momentum  $\boldsymbol{\mu} = \gamma \mathbf{J}$ , originated from an intrinsic angular momentum  $\mathbf{J}$ ,  $\gamma$  is called *gyromagnetic ratio* and quantifies the coupling between  $\boldsymbol{\mu}$  and  $\mathbf{I}$  ( $\gamma$  can be either positive or negative). If we put the nucleus inside a static magnetic field  $\mathbf{B}_0$ , which is orientated, for example, along the z-axis, such a system gains an energy:

$$E = -\boldsymbol{\mu} \cdot \mathbf{B}_0 \quad ( 1 )$$

And the field generates a torque on the magnetic moment:

$$\boldsymbol{\Gamma} = \boldsymbol{\mu} \times \mathbf{B}_0.$$

Using the law of conservation of angular momentum, we can describe the motion of  $\boldsymbol{\mu}$ :

$$\boldsymbol{\mu} = \gamma \mathbf{J} \quad ( 2 )$$

$$\boldsymbol{\Gamma} = \frac{d\mathbf{J}}{dt}$$

$$\frac{d\boldsymbol{\mu}}{dt} = \gamma \boldsymbol{\mu} \times \mathbf{B}_0 = -\gamma \mathbf{B}_0 \times \boldsymbol{\mu} \quad ( 3 )$$

Eq.( 3 ) shows a typical motion called Larmor precession which is represented in Fig. 2:  $\boldsymbol{\mu}$  precesses around  $\mathbf{B}_0$  with an angular frequency  $\boldsymbol{\omega}_0 = -\gamma \mathbf{B}_0$  called Larmor frequency,

the negative sign indicates that  $\omega_0$  is antiparallel to the applied field, so  $\mu$  rotates clockwise around the z-axis.

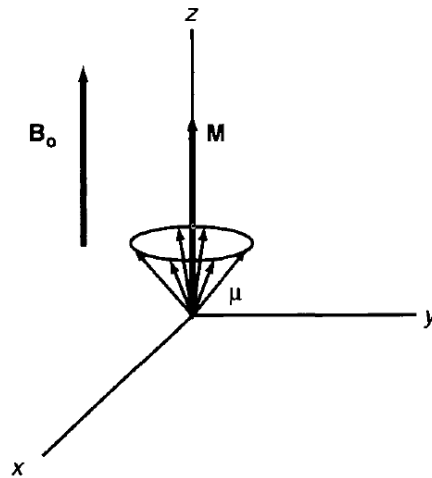


Fig. 2: Larmor precession of nuclear magnetic momentum.

An easy way to understand the magnetic resonance phenomenon, is to look at the system from a rotating frame as the one shown in Fig. 3.

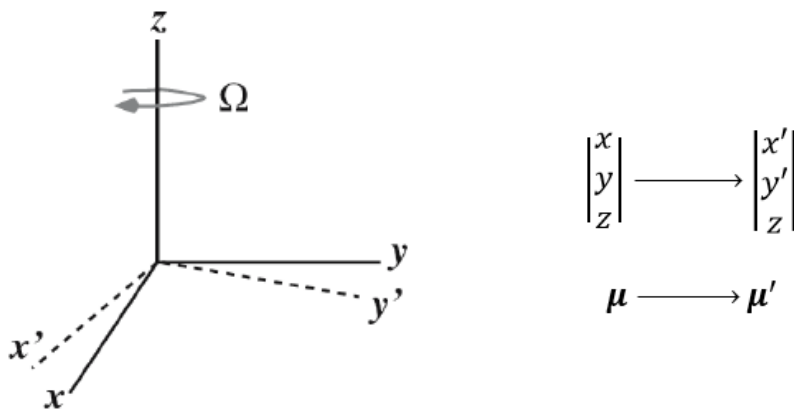


Fig. 3: A frame of reference, rotating with an angular frequency  $\Omega$  clockwise around the z-axis

From the rotating frame point of view,  $\mu'$  is rotating with an angular frequency:

$$\omega' = -B_0 - \frac{\Omega}{\gamma}$$

Then, if we apply a field  $\mathbf{B}_1 = B_1 \hat{\mathbf{x}}'$ , rotating at the same angular frequency of the rotating frame, (see Fig. 4) the nucleus perceives an apparent magnetic field in its precession motion:

$$\mathbf{B}_{app} = \mathbf{B}'_1 + \mathbf{B}_0 + \frac{\Omega}{\gamma} = B_1 \hat{\mathbf{x}}' + \left( B_0 + \frac{\Omega}{\gamma} \right) \hat{\mathbf{z}}$$

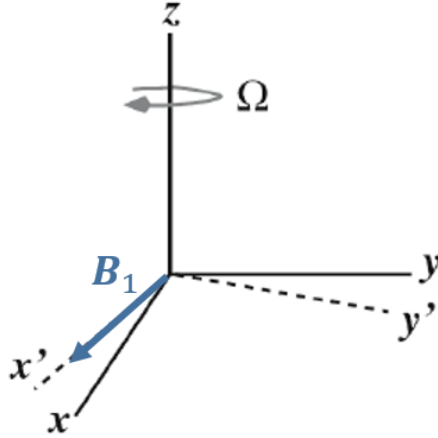


Fig. 4: The  $\mathbf{B}_1$  rotating field.

In this frame of reference, under the effect of the applied field  $\mathbf{B}_1$ , we obtain a new equation of motion for  $\boldsymbol{\mu}'$ :

$$\frac{d\boldsymbol{\mu}'}{dt} = \gamma \boldsymbol{\mu}' \times \left[ \left( B_0 + \frac{\Omega}{\gamma} \right) \hat{\mathbf{z}} + B_1 \hat{\mathbf{x}}' \right]$$

( 4 )

And thus we find the resonance condition:

$$\Omega = -\gamma B_0 = \omega_0 = 2\pi\nu_0$$

( 5 )

When the frequency  $\Omega$  of the applied  $\mathbf{B}_1$  is equal to the Larmor frequency of the nucleus, we meet the *resonance condition* of Eq.( 5 ), the apparent field in the  $z$  component of Eq.( 4 ) is equal to zero and  $\boldsymbol{\mu}'$  precesses totally around the  $x'$ -axis. Thus, we can make the magnetic dipole momentum flip from the  $z$ -axis to the  $x$ - $y$  plane with any nonzero



magnitude of the  $B_1$  field. In Fig. 5 are given the Larmor frequencies of some relevant isotopes under a static field's magnitude of 1, 1.5 and 3 Tesla.

Applied field	$B_0 = 1\text{T}$	$B_0 = 1.5\text{T}$	$B_0 = 3\text{T}$
Isotopic species	$\nu_0(\text{MHz})$		
$^1_1\text{H}$	42.58	63.87	127.74
$^2_1\text{H}$	6.54	9.81	19.62
$^{13}_6\text{C}$	10.71	16.07	32.13
$^{19}_9\text{F}$	40.08	60.12	120.24
$^{31}_{15}\text{P}$	17.25	25.88	51.75

Fig. 5: Table of Larmor frequencies.

In practice it is not necessary to satisfy perfectly Eq.( 5 ) to make the nuclear magnetic momentum to flip, we only need  $\Omega$  to be close enough to the Larmor angular frequency of the nuclei of interest. So we have  $B_1 \gg \Delta B = B_0 + \frac{\Omega}{\gamma}$  and the motion of the magnetization (the average magnetic dipole momentum) can be considered a pure precession around the  $x'$ -axis (see Fig. 6).

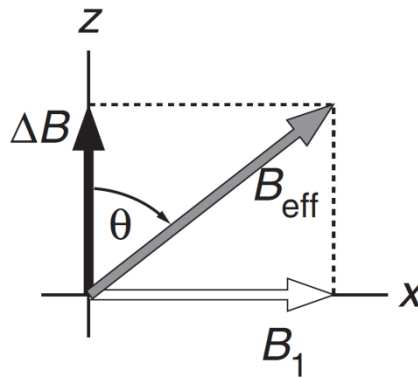


Fig. 6: The more  $\Omega$  is close to the Larmor frequency, the more  $B_1$  dominates on  $\Delta B = B_0 + \frac{\Omega}{\gamma}$ .

The angle  $\theta = \gamma B_1 t$  between  $\mu$  and the  $z$ -axis, after  $B_1$  is applied for a time  $t$ , is called *flip angle*. It is more convenient to use an oscillating magnetic field originated from a linearly polarized radiofrequency pulse, rather than a rotating one. In fact any oscillating field can be represented by the sum of two rotating components, one rotating clockwise

and the other counterclockwise with respect to  $\mathbf{B}_0$  (see Fig. 7). The counterclockwise component, in the rotating frame at the Larmor frequency, seems to rotate with an angular frequency  $-2\Omega$  and it is completely out of resonance; consequently only the clockwise component of the RF oscillating field gives a relevant contribution.

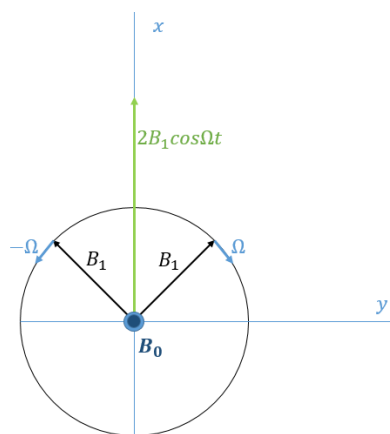


Fig. 7: An oscillating magnetic field on the x-axis is equivalent to the sum of two counter-rotating fields with half of the intensity.

## 1.2 CHEMICAL SHIELDING

The electronic environment of an atom or a molecule has an influence on the static field perceived by the nucleus, which actually senses a decreased field. The phenomenon can be understood easily from Fig. 8, in a classical way we can figure that an external magnetic field, through Lorentz force, induces currents in the electron cloud. These currents generate a magnetic field opposed to  $\mathbf{B}_0$  decreasing the magnetic field experienced by the nucleus. This effect is called *chemical shielding* or *screening* of the nucleus.

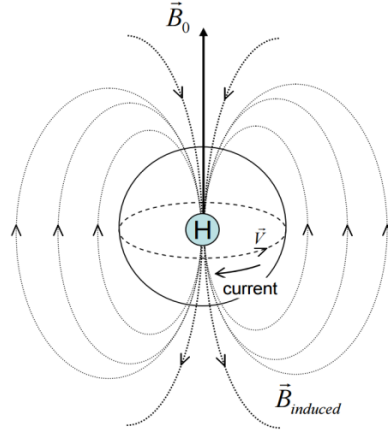


Fig. 8: In this pictorial representation, the overall motion of the electrons, caused by Lorentz force, can be simplified considering a negative charged particle moving with speed  $\vec{V}$  in a circular motion. This particle generates a current, which then generates a field opposed to  $B_0$ .

The shielding is proportional to  $B_0$ , thus the effective field on the nucleus is:

$$\mathbf{B}_{eff} = \mathbf{B}_0 - \mathbf{B}_{induced} = \mathbf{B}_0 - \sigma \mathbf{B}_0$$

( 6 )

$$\sigma = \begin{vmatrix} \sigma_{xx} & 0 & 0 \\ 0 & \sigma_{yy} & 0 \\ 0 & 0 & \sigma_{zz} \end{vmatrix}$$

$\sigma$  is the so-called *shielding factor*, in general it is a second rank tensor (19). However, rapid, random tumbling of molecules in liquids and gases leads to an averaging of the shielding interactions to an isotropic scalar quantity  $\sigma_{iso}$ , this is the case of most biological tissues:

$$\sigma = \sigma_{iso} = \frac{1}{3}(\sigma_{xx} + \sigma_{yy} + \sigma_{zz})$$

$$\mathbf{B}_{eff} = \mathbf{B}_0(1 - \sigma)$$

As  $B_{induced}$  is smaller in magnitude than  $B_0$ ,  $\sigma$  is always less than 1. Considering a spherical symmetric electronic  $S$  state, Lamb (20) gave a first quantification of the shielding factor:

$$\sigma_D = \frac{4\pi e^2}{3m_e c^2} \int_0^\infty r \rho(r) dr$$

Here  $\rho(r)$  is the density of electrons as a function of radial distance from the nucleus, while  $e$ ,  $m_e$  and  $c$  are respectively the charge of the electron, its mass and the speed of light in vacuum. For molecules analytical values for  $\sigma$  are more complicated, like the one found by Ramsey (21). By the way, typical values for  $\sigma$  are  $10^{-5}$  for protons and  $10^{-2}$  for heavier nuclei. Consequently, the frequency at which the nucleus resonates becomes:

$$\nu_{eff} = \frac{\gamma}{2\pi} B_0 (1 - \sigma)$$

So, because the frequencies depend on the applied field, it is more practical to choose a reference compound and use the relative difference in ppm (parts per million) to quantify the chemical shift:

$$\delta(ppm) = \frac{\nu - \nu_{ref}}{\nu_{ref}} \cdot 10^6$$

The rationale of NMR spectroscopy in medicine and biology is to measure the chemical shift of an atom or a molecule and quantify its presence inside a biological tissue, indeed, the reference compound should be chemically inert and the position of its chemical shift should not fluctuate remarkably because of external variables such as temperature and should produce an evident resonance peak, well separated from the other ones. It is a common practice to use tetramethylsilane (TMS) as reference compound in NMR spectroscopy, but, because of its toxicity, in biological applications or in vivo applications the use of Creatine (Cr) or  $\text{CH}_3$  peak of N-acetyl aspartate (NAA) is more suitable.

## 1.3 QUANTUM MECHANICAL TREATMENT OF MRS

As in other branches of spectroscopy, an explanation of many aspects of MRS requires the use of quantum mechanics. Now we can introduce the Spin quantum number  $I$ , responsible for the magnetic dipole momentum  $\mu_n$  of nuclei:

$$\mu_n = \gamma_n \hbar I \quad (7)$$

Where  $\gamma_n$  is the gyromagnetic ratio of the nucleus and  $\hbar$  is the Planck constant divided by  $2\pi$ .  $\gamma_n$  and  $I$  are intrinsic properties of a nucleus, some relevant values are illustrated in Fig. 9. Fluorine is not normally found in biopolymers, so the isotope which generates the highest signal is in general  $^1\text{H}$ , due to its high gyromagnetic ratio ( $\gamma$ ) and its natural abundance in organic compounds. The  $\gamma$  factor influences the population of the excited spin state, as we will see later (see Eq.( 9 )), thus the higher the gyromagnetic ratio, the higher will be the magnetization and then the higher will be the signal.

<i>Nuclei</i>	$\gamma$ (rad $\times$ sec $^{-1}$ $\times$ gauss $^{-1}$ )	$I$	<i>Natural Abundance (%)</i>
$^1\text{H}$	26,753	1/2	99.980
$^2\text{H}$	4,106	1	0.016
$^{19}\text{F}$	25,179	1/2	100.000
$^{13}\text{C}$	6,728	1/2	1.108
$^{15}\text{N}$	-2,712	1/2	0.37
$^{31}\text{P}$	10,841	1/2	100.00

Fig. 9: Spin values and gyromagnetic ratios of common isotopes used in NMR spectroscopy.

In quantum mechanics, energy in Eq.( 1 ), becomes the so-called Zeeman Hamiltonian operator ( $\mathbf{B}_0$  is aligned with z-axis):

$$H_0 = -\boldsymbol{\mu} \cdot \mathbf{B}_0 = -\mu_z B_0$$

Using Eq.( 7 ), we insert the quantum angular momentum operator  $\hbar I$ :

$$H_0 = -\hbar\gamma\mathbf{B}_0 \cdot \mathbf{I} = -\hbar\gamma B_0 I_z$$

Through the quantization of  $I_z$ , the energy levels of the system, eigenvalues of operator  $H$ , become discrete:

$$H_0 = -m\hbar\gamma B_0$$

$$m = -I, -I + 1, \dots, I - 1, I$$

For the purpose of this work we can focus only on systems with spin  $\frac{1}{2}$ , like  $^1\text{H}$ . For  $\frac{1}{2}$  spin systems, there are only 2 energy levels allowed: the lower energy state  $E_\alpha$  and the excited one  $E_\beta$ :

$$E_\alpha = -\frac{\gamma\hbar B_0}{2} = -\frac{\hbar\omega}{2}$$

( 8 )

$$E_\beta = +\frac{\gamma\hbar B_0}{2} = +\frac{\hbar\omega}{2}$$

To prevent ambiguities during calculations, we will consider frequencies and angular frequencies positive from now on. The difference  $\Delta E = \hbar\omega$  between the two levels is  $\gamma\hbar B_0$ , and so, it increases with  $B_0$ , as shown below in Fig. 10.

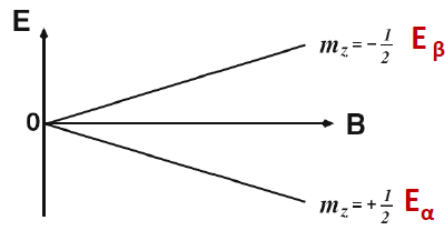


Fig. 10: Energy levels in  $I=1/2$  spin system.

Populations of these energy states are given by the use of Boltzmann distribution (19):

$$\frac{N_\alpha}{N_\beta} = e^{\frac{-\gamma\hbar B_0}{KT}} \simeq 1 - \frac{\gamma\hbar B_0}{KT}$$

( 9 )

Approximation in the last passage is made considering that, for  $B_0$  up to 10 Tesla and  $T^\circ > 1^\circ K$ , the ratio  $\frac{\gamma\hbar B_0}{KT}$  is at least 4 order of magnitude smaller than 1. This approximation justifies the fact that the signal in a clinical spectrometer is proportional to  $B_0$ . This phenomenon can also be understood by considering that the signal, produced by the magnetization  $\mathbf{M}$  of the sample, is proportional to the difference in level populations. From Eq.( 9 ) we find that this difference is proportional to the ratio  $\frac{B_0}{T}$  (Curie law):

$$Signal \propto M \propto \frac{B_0}{T}$$

As we can see in Fig. 11, under the application of the static field, a system of randomly oriented  $\frac{1}{2}$  spins becomes ordered in 2 states, one of lower energy ( $\alpha$ -state) and one of higher energy ( $\beta$ -state).

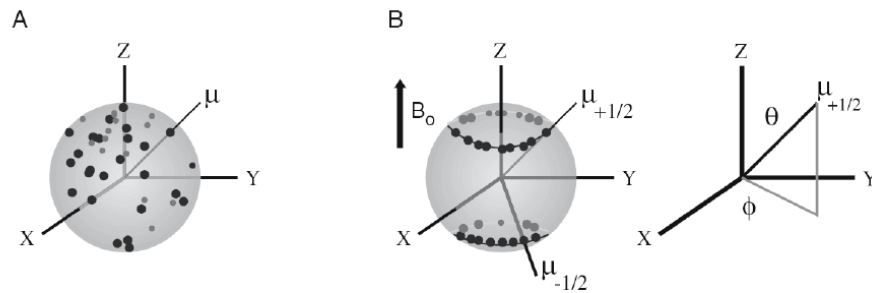


Fig. 11: A) Random orientation of nuclear spins. B) When the static field is applied, the spins orientate themselves in one of the two allowed states.

Although we can figure that also from the “quantistic” point of view the spins are precessing around  $\mathbf{B}_0$  in a mixed  $\alpha$ - $\beta$  state, measuring the state of one of them will make its wave function collapse into one of two states, thus finding it completely parallel or antiparallel to  $\mathbf{B}_0$ .

We will see later that the expectation value of the system follows the classical Larmor precession, thus considering a macroscopic sample we will measure the classical magnetization  $\mathbf{M}$  precessing around  $\mathbf{B}_0$ . We can consider now an oscillating magnetic field, like the one shown in Fig. 7.

If we turn this radiofrequency wave on for a certain time a new term  $H'$  have to be added to the Hamiltonian:

$$H' = 2\pi\mu_x B_1 \cos(2\pi\nu t) = 2\pi\hbar\gamma I_x B_1 \cos(2\pi\nu t)$$

$$H_0 = -\hbar\gamma B_0 I_z$$

$$H = H_0 + H'$$

This new term allows transitions between the energy states of  $H_0$ , it is possible to obtain the transition probability  $P$  for transitions from an initial  $m'$  state to a final  $m$  state by applying the famous *Fermi golden rule* (using first-order perturbation theory (19)):

$$P = \gamma^2 B_1^2 |\langle m | I_x | m' \rangle|^2 \delta(\| \nu_m - \nu_{m'} \| - \nu) \quad ( 10 )$$

It's possible to learn something from Eq.( 10 ):

1. First of all we can understand better the results obtained from classical theory, the precession of the Magnetization can be seen as the gradual flipping of the nuclear spins from the upper Energy states to the lower one.
2. The flipping probability is higher as the excitation field  $B_1$  and the gyromagnetic factor increase.
3. Because of the Dirac function, only a radiofrequency impulse with an energy that matches the difference between energy levels (resonance condition) can make the system flip. In practice the Dirac function (which is really unrealistic) is replaced by a line shape function  $g(\nu)$  that is a Lorentzian or approximately Lorentzian centered on the resonance frequency  $\| \nu_m - \nu_{m'} \|$ .
4. Considering spin  $\frac{1}{2}$  systems, as the one corresponding to Eq.( 8 ), we can see that the difference in energy (in frequency units) between levels corresponds to the Larmor frequency of the system. This fact implies that the classical and the quantum resonance frequency values are the same.
5. Using the properties of quantum angular momentum operators,  $I_x$  can be written as a combination of the ladder operators (a similar approach can be used for  $I_y$ ):



$$I_x = \frac{I_+ + I_-}{2}$$

Considering this last formula and the scalar product in Eq.( 10 ), we find that the allowed levels are the ones with  $\Delta m = \pm 1$  (other values of  $\Delta m$  give a null scalar product).

---

### 1.3.1 CHEMICAL SHIFT HAMILTONIAN

We can now compute the eigenvalues of the Hamiltonian operator considering the presence of various chemical species with screening factor  $\sigma_i$ :

$$H_0 = - \sum_{i=1}^N \gamma_i \hbar (1 - \sigma_i) B_0 I_{zi}$$

For the sake of simplicity only two different chemical shift species of hydrogen can be considered:

$$H_0 = -\hbar\gamma(1 - \sigma_A)B_0I_{zA} - \hbar\gamma(1 - \sigma_B)B_0I_{zB} = -h\nu_A I_{zA} - h\nu_B I_{zB} \quad ( 11 )$$

With  $\nu_A > \nu_B$ . Writing down Schrödinger equation we obtain:

$$(H_0 - E)|\psi\rangle = 0$$

It is easy to compute eigenvalues using a set of standard spin functions, products of the  $|\alpha\rangle$  and  $|\beta\rangle$  states of Fig. 10.

$$|\phi_1\rangle = |\alpha\alpha\rangle, \quad |\phi_2\rangle = |\alpha\beta\rangle, \quad |\phi_3\rangle = |\beta\alpha\rangle, \quad |\phi_4\rangle = |\beta\beta\rangle$$

With this basic functions we can now compute matrix elements of  $H_0$ , as it is shown below.

$$H_{ij} = \langle\phi_i|H_0|\phi_j\rangle$$

$H_0$  becomes diagonal and eigenvalues can be found by solving the secular equation.

$$\det \begin{vmatrix} H_{11} - E & & & \\ & H_{22} - E & & \\ & & H_{33} - E & \\ & & & H_{44} - E \end{vmatrix} = 0$$

( 12 )

The four energy levels (the eigenvalues of the Hamiltonian operator) are showed in Table 1, for brevity, calculations were omitted, but can be easily checked using the book in reference (19). Frequencies, angular frequencies and energies, will be used, from now on, indistinctly due to the fact that are all proportional quantities:  $E = h\nu = \hbar\omega$ .

<i>Energy level</i>	$E_1$	$E_2$	$E_3$	$E_4$
<i>Energy</i>	$-\frac{1}{2}(\nu_A + \nu_B)$	$-\frac{1}{2}(\nu_A - \nu_B)$	$+\frac{1}{2}(\nu_A - \nu_B)$	$+\frac{1}{2}(\nu_A + \nu_B)$
<i>Eigenstate</i>	$ \alpha\alpha\rangle$	$ \alpha\beta\rangle$	$ \beta\alpha\rangle$	$ \beta\beta\rangle$
<i>m</i>	1	0	0	-1

Table 1: Energy levels of the 2-spin system without coupling.

Since, by Eq.( 10 ), only changes of magnetic quantum number with  $\Delta m = \pm 1$  can occur, the allowed transitions are:  $E_1 \leftrightarrow E_2$  with  $\Delta E = \nu_B$ ,  $E_1 \leftrightarrow E_3$  with  $\Delta E = \nu_A$ ,  $E_3 \leftrightarrow E_4$  with  $\Delta E = \nu_B$  and  $E_2 \leftrightarrow E_4$  with  $\Delta E = \nu_A$ . This means that in the NMR spectrum of this system we would see two spectral lines centered in  $\nu_A$  and  $\nu_B$ . The allowed transitions of this system occur with the same probability (2 with energy  $\nu_A$  and 2 with  $\nu_B$ ), thus, we see two peaks of equal magnitude, as showed in Fig. 12.

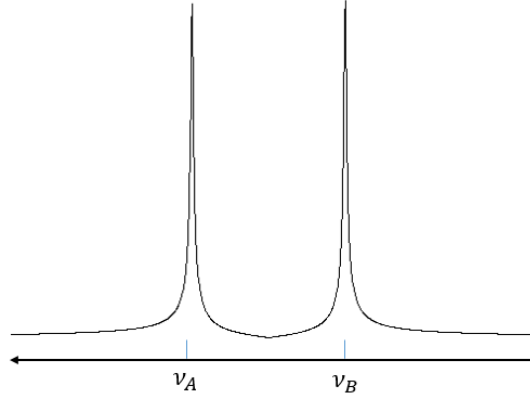


Fig. 12: Modulus of an NMR spectrum of a 2-spins system without coupling.

---

### 1.3.2 J-COUPLING

Magnetic interactions between nuclei can occur through space (dipolar coupling) and through chemical bonds (j-coupling). Dipolar coupling Hamiltonian term is described below:

$$H_{dip} = \frac{\boldsymbol{\mu}_1 \cdot \boldsymbol{\mu}_2}{r^3} - 3 \frac{(\boldsymbol{\mu}_1 \cdot \boldsymbol{r})(\boldsymbol{\mu}_2 \cdot \boldsymbol{r})}{r^5} \quad ( 13 )$$

Where  $\boldsymbol{r}$  is the distance between the two nuclei and  $\boldsymbol{\mu}_1 \boldsymbol{\mu}_2$  are the nuclear magnetic dipole quantum operators of two coupled nuclei. Dipolar coupling is important in relaxation processes and defines line-shapes of peaks. It usually does not affect the number of peaks or the Larmor frequencies in the spectrum of biological tissues, because interacting nuclei are in molecules that are in rapid random motion, as are most small molecules in solution. Consequently, this interaction averages almost completely to zero (19) (22).

Rapid tumbling of molecules does not average to zero j-coupling interaction, which depends on chemical bonds and not on orientation or distances between nuclei, unlike dipolar term in Eq.( 13 ). J-coupling can be either homonuclear or heteronuclear, this interaction involves nuclei mainly through covalent bonds (23) and with less strength through hydrogen bonds (24). The hyperfine interaction between electronic and nuclear spins is governed by the Fermi contact interaction:

$$E_{Fermi} = -\frac{2}{3} \mu_0 \boldsymbol{\mu}_n \cdot \boldsymbol{\mu}_e |\psi(0)|^2$$

Where  $\mu_0$  is the magnetic permeability of vacuum,  $\boldsymbol{\mu}_n$  and  $\boldsymbol{\mu}_e$  are the magnetic dipole moments of nucleus and the electron respectively and  $\psi(0)$  the electronic wave function at the nucleus. Since electrons have negative gyromagnetic ratios, the Fermi contact interaction favors the antiparallel spin configuration that has a lower energy value. Meanwhile Pauli Exclusion Principle says that electronic spins in an orbital must be antiparallel, this might force the system to be in a higher energy configuration, as shown in Fig. 13.

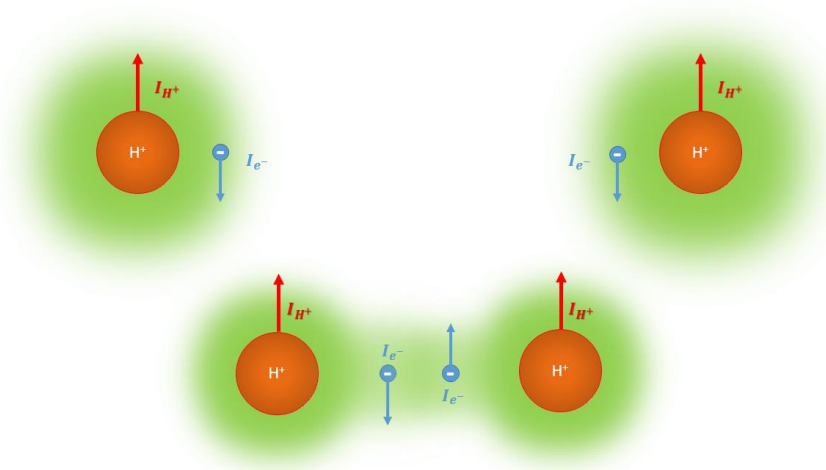


Fig. 13: The Fermi contact interaction and the Pauli Exclusion Principle establish the j-coupling between two nuclei linked by a covalent bond.

Thus, because of j-coupling, another term has to be added to the Hamiltonian, writing it in terms of frequencies we have:

$$H = -\nu_A I_{zA} - \nu_B I_{zB} + j_{AB} \mathbf{I}_A \cdot \mathbf{I}_B \quad ( 14 )$$

As can be seen from Eq.( 14 ),  $\mathbf{I}_A$  and  $\mathbf{I}_B$  are coupled by a scalar factor  $j_{AB}$ . In general, this quantity is a  $3 \times 3$  tensor, but in liquids and biological tissues it averages to a scalar isotropic factor, due to rapid tumbling of nuclei. To find the matrix form of this new Hamiltonian we have to consider the total spin operators:

$$\mathbf{F} = \mathbf{I}_A + \mathbf{I}_B \quad F_z = I_{zA} + I_{zB}$$

With the eigenvectors of  $F_z$ :

$\phi_1$	$\phi_2$	$\phi_3$	$\phi_4$
$ \alpha\alpha\rangle$	$ \alpha\beta\rangle$	$ \beta\alpha\rangle$	$ \beta\beta\rangle$

And its eigenvalues:

$$F_z \phi_m = f_{zm} \phi_m$$

$f_{z1}$	$f_{z2}$	$f_{z3}$	$f_{z4}$
1	0	0	-1

The selection rule becomes  $\Delta f_z = \pm 1$ , consequently only a single spin can flip during a single transition. It's easy to show that  $F_z$  commute with  $H$  of Eq.( 14 ), and thus we have:

$$[F_z, H] = 0 \rightarrow (f_{zm} - f_{zn}) \langle \phi_m | H | \phi_n \rangle = 0$$

( 15 )

From Eq.( 15 ) the Hamiltonian matrix elements that can be non-zero are the terms  $\langle \phi_m | H | \phi_n \rangle$  corresponding to  $f_m = f_n$  . In this way we can write down the secular equation:

$$\det \begin{vmatrix} H_{11} - E & 0 & 0 & 0 \\ 0 & H_{22} - E & H_{23} & 0 \\ 0 & H_{32} & H_{33} - E & 0 \\ 0 & 0 & 0 & H_{44} - E \end{vmatrix} = 0$$

Evaluating the matrix elements, it can be found:

$$H_{11} = -\frac{1}{2}(v_A + v_B) + \frac{1}{4}j_{AB}$$

$$H_{22} = -\frac{1}{2}(v_A - v_B) - \frac{1}{4}j_{AB}$$

$$H_{33} = +\frac{1}{2}(v_A - v_B) - \frac{1}{4}j_{AB}$$

$$H_{44} = +\frac{1}{2}(v_A + v_B) + \frac{1}{4}j_{AB}$$

$$H_{23} = H_{32} = +\frac{1}{2}j_{AB}$$

( 16 )

### 1.3.3 WEAK COUPLING APPROXIMATION AND FIRST-ORDER SPECTRA

In most cases the *weak coupling approximation* can be used to simplify spectral analysis

$$j_{AX} \ll |v_A - v_X|$$

With this approximation, comparing with results from Eq.( 16 ), it is possible to see that eigenvalues of the 2-spin system becomes the ones of a diagonal Hamiltonian with  $H_{23} = H_{32} = 0$ . Weak coupled systems are commonly called AX systems and can be described by the weak coupled Hamiltonian:

$$H = -v_A I_{zA} - v_X I_{zX} + j_{AB} I_{zA} I_{zX} \quad ( 17 )$$

$$\det \begin{vmatrix} -\frac{1}{2}(v_A+v_B) + \frac{1}{4}j_{AB} - E & 0 & 0 & 0 \\ 0 & -\frac{1}{2}(v_A-v_B) - \frac{1}{4}j_{AB} - E & 0 & 0 \\ 0 & 0 & +\frac{1}{2}(v_A-v_B) - \frac{1}{4}j_{AB} - E & 0 \\ 0 & 0 & 0 & +\frac{1}{2}(v_A+v_B) + \frac{1}{4}j_{AB} - E \end{vmatrix} = 0$$

Solving the secular equation we find the energy values of the system:

$E_1$	$E_2$	$E_3$	$E_4$
$-\frac{1}{2}(v_A+v_X) + \frac{1}{4}j_{AB}$	$-\frac{1}{2}(v_A-v_X) - \frac{1}{4}j_{AX}$	$+\frac{1}{2}(v_A-v_X) - \frac{1}{4}j_{AX}$	$+\frac{1}{2}(v_A+v_X) - \frac{1}{4}j_{AX}$

Table 2: Energy values of a weak coupled AX system of a 2-spins system.

The couple of equivalent transitions in Fig. 12 becomes split (Fig. 14 right), since no one of the four allowed transitions (Fig. 14 left) is equivalent to the others.

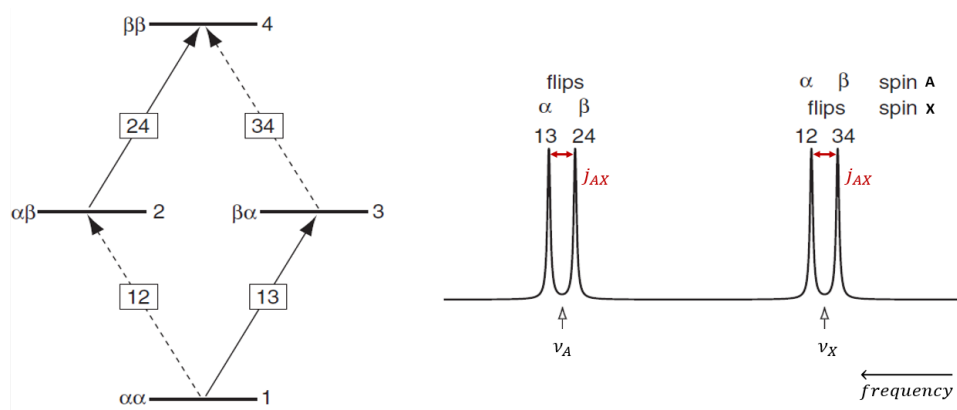


Fig. 14: The four allowed transitions in the AX spin system (left). Visualization of the transitions in a NMR power spectrum (right).

Taking Fig. 14 as a reference, in the right-side we see the typical doublet of doublets line-shape of an AX NMR spectrum. Each doublet is centered on the Larmor frequency of the flipping nucleus while the other remains stable in an  $\alpha$  or  $\beta$  state. Transitions occurs with the same probability, thus magnitude of each peak is the same. Separation in frequency between two peaks of the same multiplet is equal to the value of the coupling of the system. To extend these results to more than two spins we have to introduce *Magnetic equivalence*. Nuclei are said to be *chemically equivalent* when they have the same chemical shift, usually as a result of molecular symmetry. Nuclei in a set are *magnetically equivalent* when they all possess the same chemical shift and all nuclei in the set are coupled equally with any other single nucleus in the molecule. Spectra from magnetically equivalent systems linearly sum together.

## First order analysis

First order spectral analysis is applicable only when at least  $\frac{|\nu_A - \nu_X|}{j_{AX}} \leq 7$  (19).

1. A nucleus or group of nuclei, coupled to a set of  $n$  nuclei with spin  $I$ , will have its resonance split into  $2nI + 1$  lines. For the common case of  $I = 1/2$ , there are then  $n + 1$  lines.
2. The relative intensities of the  $2nI + 1$  lines can be determined from the number of ways each spin status may be formed. For the case of  $I = 1/2$ , the intensities of the  $n + 1$  lines correspond to the coefficients of the binomial theorem (Fig. 15).
3. The  $2nI + 1$  lines are equally spaced, with the frequency separation between adjacent lines being equal to  $j$ , the coupling constant (Fig. 14, right).
4. Coupling between nuclei within a magnetically equivalent set does not affect the spectrum.

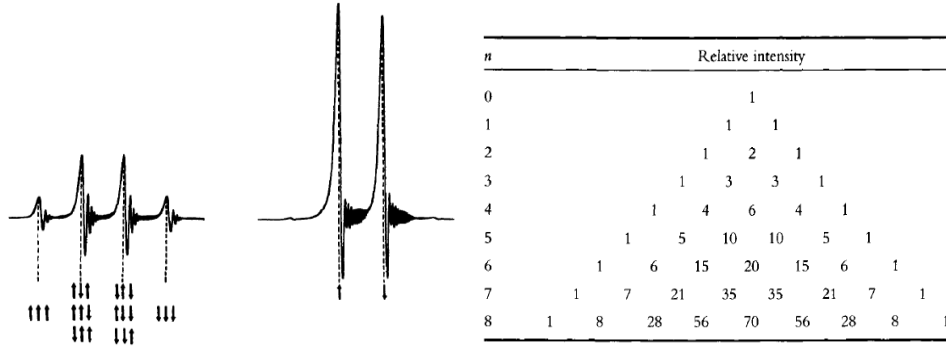


Fig. 15: Example of an  $A_3X$  weak coupled spectrum, where a nucleus is coupled to a set of 3 magnetically equivalent nuclei (left). Relative intensities in a spin  $\frac{1}{2}$  multiplet are given by the coefficients of the binomial theorem.

### 1.3.4 STRONG COUPLING

When weak coupling approximation can't be performed, we have strong coupling and the so called AB spectrum. AB Hamiltonian in Eq.( 16 ) is not diagonal because standard basic functions  $\phi_1 \dots \phi_4$  are not eigenfunctions of the system. To find the solutions of secular equation in Eq.( 18 ), a new basic set is needed.

$$\det \begin{vmatrix} -\frac{1}{2}(v_A+v_B) + \frac{1}{4}j_{AB} - E & 0 & 0 & 0 \\ 0 & -\frac{1}{2}(v_A-v_B) - \frac{1}{4}j_{AB} - E & \frac{1}{2}j_{AB} & 0 \\ 0 & \frac{1}{2}j_{AB} & +\frac{1}{2}(v_A-v_B) - \frac{1}{4}j_{AB} - E & 0 \\ 0 & 0 & 0 & +\frac{1}{2}(v_A+v_B) + \frac{1}{4}j_{AB} - E \end{vmatrix} = 0 \quad ( 18 )$$

The new basic set can be found by linear combination of the old basic functions:

$$\psi_1 = \phi_1, \quad \psi_2 = \frac{1}{\sqrt{1+Q^2}}(\phi_2 + Q\phi_3), \quad \psi_3 = \frac{1}{\sqrt{1+Q^2}}(-Q\phi_2 + \phi_3), \quad \psi_4 = \phi_4 \quad ( 19 )$$

$$Q = \frac{j_{AB}}{(v_A - v_B) + \sqrt{(v_A - v_B)^2 + j_{AB}^2}}$$



From Eq.( 19 ), we see that, also for an AB system, states  $\phi_1$  and  $\phi_4$  do not mix and remain “pure” while  $\phi_2$  and  $\phi_3$  mix together in proportion on how strong is the coupling compared to chemical shift separation ( $\nu_A - \nu_B$ ). When  $j_{AX} \ll |\nu_A - \nu_B|$ ,  $\phi_2$  and  $\phi_3$  do not mix and we obtain the AX spectral pattern, the energy values become the ones depicted in Table 2. Conversely when  $j_{AX} \gg |\nu_A - \nu_B|$  the system becomes a one-spin system and the four energy levels collapse to the  $E_\alpha$  and  $E_\beta$  states of Fig. 10. By the way, using the new basis set it is easy to see that solutions of Eq.( 18 ) are :

$E_1$	$E_2$	$E_3$	$E_4$
$-\frac{1}{2}(\nu_A + \nu_B) + \frac{1}{4}j_{AB}$	$-\frac{1}{2}\sqrt{(\nu_A - \nu_B)^2 + j_{AB}^2} - \frac{1}{4}j_{AB}$	$+\frac{1}{2}\sqrt{(\nu_A - \nu_B)^2 + j_{AB}^2} - \frac{1}{4}j_{AB}$	$+\frac{1}{2}(\nu_A + \nu_B) + \frac{1}{4}j_{AB}$

Table 3: Energy values of a strong coupled AB system.

Relative transition probabilities can also be calculated by Eq.( 10 ), evaluating the matrix elements  $P_{mn} \propto \langle \psi_m | \sum_{i=1}^N \gamma_i I_{xi} | \psi_m \rangle$ . Results are summarized in Table 4 and the AB NMR spectrum is showed in Fig. 16.

$$C = \frac{1}{2} \sqrt{(\nu_A - \nu_B)^2 + j_{AB}^2}$$

Line	Transition	Frequency (Hz)	Relative intensity
1	$T_{2 \rightarrow 4}$	$C + \frac{1}{2}j_{AB}$	$1 - \frac{j_{AB}}{2C}$
2	$T_{1 \rightarrow 3}$	$C - \frac{1}{2}j_{AB}$	$1 + \frac{j_{AB}}{2C}$
3	$T_{3 \rightarrow 4}$	$-C + \frac{1}{2}j_{AB}$	$1 + \frac{j_{AB}}{2C}$
4	$T_{1 \rightarrow 2}$	$-C - \frac{1}{2}j_{AB}$	$1 - \frac{j_{AB}}{2C}$

Table 4: Transition probabilities of an AB spectrum.

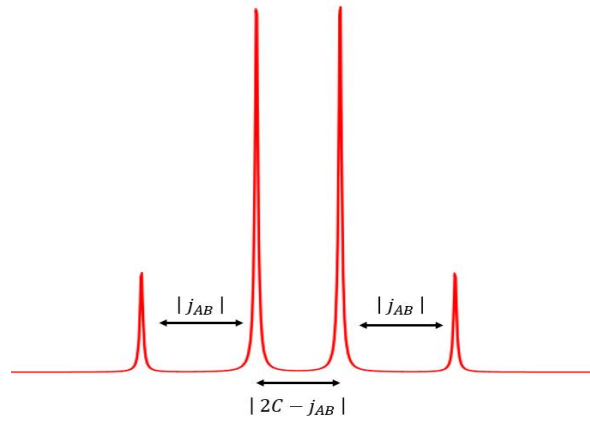


Fig. 16: AB NMR spectrum of two strongly coupled spins.

## 1.4 DENSITY MATRIX FORMALISM

The purpose of this section is to develop, through few calculations, the basic elements of the density matrix formalism, a useful tool to understand and analyze pulse sequences and MRS experiments. The key role of this approach is the ability to predict expectation values of quantum operators also on a macroscopic set of nuclei. If we have a set of  $N$  nuclei in a molecule, the system can be described by  $2^N$  quantum states  $\psi_i$ . Considering the  $2^N$  standard basic functions  $\phi_k$ , products of the  $|\alpha\rangle$  and  $|\beta\rangle$  states of the single nuclei, and considering that these functions constitute a complete orthonormal set, we can represent each eigenstate  $\psi_i$  of the system by a linear combination of the  $\phi_k$ .

$$\psi_i = \sum_{k=1}^{2^N} c_k \phi_k$$

Thus, considering a macroscopic sample, the total quantum state  $\mathcal{E}$  will be the average of the possible “pure” states  $\psi_i$ , each one weighted on its occurrence probability  $p_i$ .

$$\mathcal{E} = \sum_{i=1}^{2^N} p_i \psi_i$$

If we want then to get the expectation value of an observable on the pure state  $\psi_i$  we have:

$$\langle A \rangle_i = \langle \psi_i^* | A | \psi_i \rangle = \sum_{k,l=1}^{2^N} c_{ik}^* c_{il} \langle \phi_k^* | A | \phi_l \rangle = \sum_{k,l=1}^{2^N} c_{ik}^* c_{il} A_{kl}$$

( 20 )

Where the  $A_{kl}$  are the matrix elements of the operator  $A$ , evaluated on the standard basis functions. If we know the occurrence probability  $p_i$  of each pure state  $\psi_i$ , we can also compute the expectation value of  $A$  on the macroscopic sample:

$$\langle A \rangle_{\mathcal{E}} = \sum_{i=1}^{2^N} p_i \langle A \rangle_i = \sum_{i=1}^{2^N} \sum_{k,l=1}^{2^N} p_i c_{ik}^* c_{il} A_{kl}$$

$$\rho_{lk} = \sum_{i=1}^{2^N} p_i c_{ik}^* c_{il}$$

( 21 )

Eq.( 21 ) defines the density matrix of the macroscopic set  $\mathcal{E}$ . Having the density matrix of a system means knowing all the knowable of that system, since all the observables can be evaluated as shown below in Eq. ( 22 ).

$$\langle A \rangle_{\mathcal{E}} = \sum_{k=1}^{2^N} \sum_{l=1}^{2^N} \rho_{lk} A_{kl} = \sum_{l=1}^{2^N} [\rho A]_{ll} = Tr(\rho A)$$

$$\langle A \rangle_{\mathcal{E}} = Tr(\rho A) = Tr(A \rho)$$

( 22 )

As time evolution of wave functions is described by Schrödinger equation, it can be demonstrated (19) that the time evolution of a density matrix is described by Eq.( 23 ), in which  $H$  is written in terms of angular frequency units.

$$\rho(t) = e^{-iHt} \rho(0) e^{iHt}$$

( 23 )

$$\frac{d\rho_{lk}}{dt} = H \rho_{lk} = (E_l - E_k) \rho_{lk}$$

The meaning of the exponential operators can be understood by representing them in Taylor series:

$$e^A = \sum_{n=0}^{\infty} \left( \frac{A^n}{n!} \right) = 1 + A + \frac{A^2}{2!} + \frac{A^3}{3!} + \dots$$

Considering the fact that the total spin operator  $F_z = \sum_n I_{nz}$  is the generator of rotations around z-axis, it is possible to change the reference and watch the system from a rotating frame:

$$R_z(-\theta) = e^{iF_z\theta}$$

$$\rho' = e^{-iF_z\theta t} \rho e^{iF_z\theta t} = e^{-i\omega_0 t F_z} \rho e^{i\omega_0 t F_z}$$

( 24 )

Moreover, applying a radiofrequency pulse on the x-axis of this frame of reference makes the system rotate around the axis of an angle  $-\gamma B_1 \tau$ . Using Eq.( 23 ), we obtain:

$$\rho(\tau) = e^{-i\gamma B_1 \tau F_x} \rho(0) e^{i\gamma B_1 \tau F_x} = e^{-i\gamma B_1 \tau F_x} \rho(0) e^{i\gamma B_1 \tau F_x}$$

Where  $F_x = \sum_n I_{nx}$  is the total x-spin operator in the rotating frame. Thus, making some algebra, we can express the transformations with a simpler formula:

$$e^{i\theta F_x} = \prod_n e^{i\theta I_{nx}}$$

$$\begin{aligned} e^{i\theta I_{nx}} &= 1 + i\theta I_{nx} + \frac{(i\theta I_{nx})^2}{2!} + \frac{(i\theta I_{nx})^3}{3!} + \dots \\ &= \left[ 1 - \frac{(\theta I_{nx})^2}{2!} + \dots \right] + 2i \left[ (\theta I_{nx}) - \frac{(\theta I_{nx})^3}{3!} + \dots \right] I_{nx} \\ &= \mathbf{1} \cos\left(\frac{\theta}{2}\right) + 2i \sin\left(\frac{\theta}{2}\right) I_{nx} \end{aligned}$$

$$e^{i\theta I_{nx}} = \mathbf{1} \cos\left(\frac{\theta}{2}\right) + 2i \sin\left(\frac{\theta}{2}\right) I_{nx}$$

( 25 )

---

### 1.4.1 ONE SPIN SYSTEM

Considering a system made of magnetically equivalent nuclei (one-spin system), omitting  $\hbar$ , the spin operators are:

$$\mathbf{1} = \begin{vmatrix} 1 & 0 \\ 0 & 1 \end{vmatrix} \quad I_x = 1/2 \begin{vmatrix} 0 & 1 \\ 1 & 0 \end{vmatrix} \quad I_y = 1/2 \begin{vmatrix} 0 & -i \\ i & 0 \end{vmatrix} \quad I_z = 1/2 \begin{vmatrix} 1 & 0 \\ 0 & -1 \end{vmatrix}$$

( 26 )

And the quadrature detection operators:

$$I_+ = I_x + iI_y = \begin{vmatrix} 0 & 1 \\ 0 & 0 \end{vmatrix} \quad I_- = I_x - iI_y = \begin{vmatrix} 0 & 0 \\ 1 & 0 \end{vmatrix}$$

We can now compute the equilibrium density matrix of the one-spin system. This system has two eigenvectors  $|\phi_1\rangle = |\alpha\rangle$  and  $|\phi_2\rangle = |\beta\rangle$ , with eigenvalues  $E_\alpha$  and  $E_\beta$ ; evaluating the matrix elements, from Eq.( 21 ), we obtain:

$$c_{12} = c_{21} = 0, \quad c_{11} = c_{22} = 1$$

Using the fact that, in a macroscopic system, the occurrence probability of the two eigenvectors is given by Boltzmann distribution (25), and using the approximation  $\frac{E_\alpha - E_\beta}{KT} \ll 1$ , previously applied in Eq.( 9 ), we can compute the equilibrium density matrix:

$$\frac{p_1}{p_2} = e^{-(E_\alpha - E_\beta)/KT} \simeq 1 - \varepsilon$$

$$p_1 \simeq \frac{1 + \varepsilon/2}{2} \quad p_2 \simeq \frac{1 - \varepsilon/2}{2}$$

$$\rho = \frac{1}{2} \begin{vmatrix} 1 + \varepsilon/2 & 0 \\ 0 & 1 - \varepsilon/2 \end{vmatrix} = \frac{1}{2} \begin{vmatrix} 1 & 0 \\ 0 & 1 \end{vmatrix} + \frac{\varepsilon}{4} \begin{vmatrix} 1 & 0 \\ 0 & -1 \end{vmatrix} = \frac{1}{2} \mathbf{1} + \frac{\varepsilon}{2} I_z$$

( 27 )

We would have reach the same results by using the Boltzmann distribution quantum operator:

$$\rho_{mn} = \langle \phi_m | e^{-\frac{H}{kT}} | \phi_l \rangle = \langle \phi_m | e^{-\varepsilon I_z} | \phi_l \rangle \implies \rho = \begin{vmatrix} e^{+\varepsilon/2} & 0 \\ 0 & e^{-\varepsilon/2} \end{vmatrix} \simeq \langle \phi_m | \frac{1}{2} \mathbf{1} - \frac{1}{2} \varepsilon I_z | \phi_l \rangle$$

( 28 )

The identity operator  $\mathbf{1}$  has no effect on the observables of interest in NMR studies, so it is common practice to subtract it from the equilibrium density matrix. Moreover, since NMR experiments concerns only changes in the individual elements during time evolution, we can also ignore constants (26) and find a much simpler form for the equilibrium density matrix:

$$\rho_{eq} = I_z$$

Applying a  $\pi/2$  radiofrequency pulse on the x-axis in the rotating frame with angular frequency  $\omega_{RF} = \omega_0$ , contributions of the frame rotation and free precession under  $H_0 = -\omega_0 I_z$  are opposed and cancel each other out:

$$e^{-i\omega_0 \tau I_z} e^{i\omega_0 \tau I_z} \rho e^{-i\omega_0 \tau I_z} e^{i\omega_0 \tau I_z} = \rho$$

The only term that gives contributions is the one containing the radiofrequency pulse, that appears static in this rotating frame:  $H' = \gamma B_1 I_x$ . With the aim of Eq.( 23 ), we can bring the magnetization in the x-y plane by applying the pulse for a time  $\tau = \frac{\pi}{2} / \gamma B_1$  and evaluate the magnetization:

$$H' = \gamma B_1 I_x$$

$$\rho_{eq} = I_z \xrightarrow{90^\circ \text{ Pulse}} e^{-\frac{i\pi I_x}{2}} I_z e^{\frac{i\pi I_x}{2}} = \frac{\sqrt{2}}{2} \begin{vmatrix} 1 & -i \\ -i & 1 \end{vmatrix} \frac{1}{2} \begin{vmatrix} 1 & 0 \\ 0 & -1 \end{vmatrix} = \frac{\sqrt{2}}{2} \begin{vmatrix} 1 & i \\ i & 1 \end{vmatrix} = \frac{1}{2} \begin{vmatrix} 0 & i \\ -i & 0 \end{vmatrix}$$

$$= -I_y$$

$$M_z = \frac{N\gamma^2 \hbar^2 B_0}{2KT} I_z \quad M_{xy} = \frac{N\gamma^2 \hbar^2 B_0}{2KT} I_+$$

$$\langle M_z \rangle \propto Tr(-I_z I_y) = 0 \quad \langle M_{xy} \rangle = \langle M_x + iM_y \rangle \propto Tr(-I_+ I_y) = Tr[-(I_x + iI_y) I_y]$$

$$= -i$$

After the pulse, in the laboratory frame of reference, the Hamiltonian becomes:

$$H = -\gamma B_0 I_z = -\omega_0 I_z$$

Using the relation in Eq.( 29 ) (which is easy to demonstrate since the basis vectors are eigenvectors of  $I_z$ ), we find the magnetization rotating, like in the classical case, in the x-y plane:

$$e^{i\omega_0 t I_z} = \begin{vmatrix} e^{i\omega_0 t/2} & 0 \\ 0 & e^{-i\omega_0 t/2} \end{vmatrix}$$

( 29 )

$$-I_y \xrightarrow{\text{Free evolution } t} e^{i\omega_0 t I_z} I_y e^{-i\omega_0 t I_z} = \frac{1}{2} \begin{vmatrix} 0 & ie^{+i\omega_0 t} \\ -ie^{-i\omega_0 t} & 0 \end{vmatrix}$$

$$\begin{aligned} \langle M_{xy}(t) \rangle &\propto \text{Tr} \left( \frac{1}{2} \begin{vmatrix} 0 & ie^{+i\omega_0 t} \\ -ie^{-i\omega_0 t} & 0 \end{vmatrix} \begin{vmatrix} 0 & 1 \\ 1 & 0 \end{vmatrix} \right) \\ &= \frac{1}{2} \text{Tr} [-I_y I_+ \cos(\omega_0 t) - I_x I_+ \sin(\omega_0 t)] = \frac{-ie^{-i\omega_0 t}}{2} \end{aligned}$$

( 30 )

In this way we demonstrated the phenomena of NMR and Larmor precession, previously seen in section 1.1 and 1.3, also with the density matrix formalism.

---

### 1.4.2 TWO SPINS

Dealing with more than one kind of spin means working with matrices of  $2^N \times 2^N$  elements, where  $N$  is the number of different kinds of protons resonating. By the way, most of the results that can be obtained in the case of one and two spins are generalizable for a system of  $N$  spins. We can use 1-spin operators in Eq.( 26 ) to obtain the spin operators for the two spins  $I$  and  $S$ ; this task can be achieved through the use of direct product  $\otimes$  in the following way:

$$O_A \otimes O_B = \begin{bmatrix} a & b \\ c & d \end{bmatrix} \otimes \begin{bmatrix} e & f \\ g & h \end{bmatrix} = \begin{bmatrix} a \begin{bmatrix} e & f \\ g & h \end{bmatrix} & b \begin{bmatrix} e & f \\ g & h \end{bmatrix} \\ c \begin{bmatrix} e & f \\ g & h \end{bmatrix} & d \begin{bmatrix} e & f \\ g & h \end{bmatrix} \end{bmatrix}$$

With this method, it is easy to evaluate the two spin operators in the two spin system, for example:

$$2I_x S_x = 2I_x \otimes S_x = \frac{1}{2} \begin{vmatrix} 0 & 0 & 0 & 1 \\ 0 & 0 & 1 & 0 \\ 0 & 1 & 0 & 0 \\ 1 & 0 & 0 & 0 \end{vmatrix}$$

For one spin operators in the 2 spin system, the identity matrix  $\mathbf{1}$  has to be used in the direct product, like in the examples below:

$$I_z = I_z^{1\text{ spin}} \otimes \mathbf{1} = \frac{1}{2} \begin{vmatrix} 1 & 0 & 0 & 0 \\ 0 & 1 & 0 & 0 \\ 0 & 0 & -1 & 0 \\ 0 & 0 & 0 & -1 \end{vmatrix}$$

$$S_z = \mathbf{1} \otimes I_z^{1\text{ spin}} = \frac{1}{2} \begin{vmatrix} 1 & 0 & 0 & 0 \\ 0 & -1 & 0 & 0 \\ 0 & 0 & 1 & 0 \\ 0 & 0 & 0 & -1 \end{vmatrix}$$

For more than one spin, the equilibrium density matrix becomes the sum of the single spin density matrices, for the two spins I and S, from Eq.( 27 ) we obtain:

$$\rho_{eq} = \omega_I I_z + \omega_S S_z$$

Since chemical shift differences ( $\sim 500$  Hz) are small compared to the hydrogen's resonance frequency ( $\sim 128$  MHz for a 3T spectrometer), it possible to simplify and rescale the equilibrium density matrix. Treatment of spin systems without considering this approximation can also be developed (19), but for the purposes of this work we can consider:

$$\rho_{eq} = I_z + S_z$$



$$\rho_{eq} = \begin{vmatrix} 1 & 0 & 0 & 0 \\ 0 & 0 & 0 & 0 \\ 0 & 0 & 0 & 0 \\ 0 & 0 & 0 & -1 \end{vmatrix}$$

( 31 )

We already saw that the application of a radiofrequency pulse, of a frequency equal to the Larmor frequency of a nucleus, for a time  $\tau = \frac{\pi}{2}/\gamma B_1$ , makes a spin flip on the x-y plane. To make both the spins flip we need to apply a pulse containing the two Larmor frequencies of the nuclei. The application of this *non-selective pulse* can be formalized by the use of the rotation operator  $R_{\frac{\pi}{2}x} = e^{i\frac{\pi}{2}I_x}e^{i\frac{\pi}{2}S_x}$  on the equilibrium matrix. With the use of Eq.( 25 ), we can evaluate the matrix elements of this operator:

$$R_{\frac{\pi}{2}x} = \left(\frac{\sqrt{2}}{2}\mathbf{1} + i\sqrt{2}I_x\right)\left(\frac{\sqrt{2}}{2}\mathbf{1} + i\sqrt{2}S_x\right) = \frac{1}{2} \begin{vmatrix} 1 & i & i & -1 \\ i & 1 & -1 & i \\ i & -1 & 1 & i \\ -1 & i & i & 1 \end{vmatrix}$$

Proceeding like in section 1.3.1, we obtain the density matrix of the system after a non-selective  $\frac{\pi}{2}$  pulse.

$$R_{\frac{\pi}{2}x}^\dagger \rho_{eq} R_{\frac{\pi}{2}x} = \frac{1}{2} \begin{vmatrix} 0 & i & i & 0 \\ -i & 0 & 0 & i \\ -i & 0 & 0 & i \\ 0 & -i & -i & 0 \end{vmatrix} = -I_y - S_y$$

( 32 )

The use of a selective pulse instead, for example using only frequency  $\omega_I$  in the radiofrequency, brings  $I$  along y-axis leaving  $S$  unaffected:

$$R_{\frac{\pi}{2}Ix}^\dagger \rho_{eq} R_{\frac{\pi}{2}Ix} = \frac{1}{2} \begin{vmatrix} 1 & 0 & i & 0 \\ 0 & -1 & 0 & i \\ -i & 0 & 1 & 0 \\ 0 & -i & 0 & -1 \end{vmatrix} = -I_y + S_z$$

( 33 )

There is something more to say about the elements of these density matrices:

- Occurrence probabilities: keeping into account Table 1 and Fig. 17 we see that density matrix elements are associated with transitions between energy levels

(26). Diagonal elements are connected to conserved quantities and populations of energy levels, see Schrödinger equation for matrix elements in Eq.( 23 ) to understand it. Indeed, without scaling or approximating the equilibrium density matrix of Eq.( 28 ) diagonal elements correspond to the occurrence probability of the quantum state. Populations of diagonal elements tells us that there are uncorrelated spins, for example the  $S$  spins in Eq.( 33 ).

- Single quantum coherences: The non-diagonal terms are called coherences, suggesting that they are linked to correlations between spins. Looking at Fig. 17,  $\Omega_{21}$ ,  $\Omega_{31}$ ,  $\Omega_{42}$ ,  $\Omega_{43}$ ,  $\Omega_{12}$ ,  $\Omega_{13}$ ,  $\Omega_{24}$  and  $\Omega_{34}$  are terms produced by single-quantum transitions that involves changes in  $\Delta f_z = \pm 1$  and are known as single quantum coherences.
- Zero and double quantum coherences:  $\Omega_{41}$ ,  $\Omega_{14}$  and  $\Omega_{32}$ ,  $\Omega_{23}$  are called double quantum coherences and zero quantum coherences respectively. Double quantum coherences are produced by double quantum transitions between energy levels with  $\Delta f_z = \pm 2$ , for example from  $|\alpha\alpha\rangle$  to  $|\beta\beta\rangle$  and vice versa. Zero quantum transitions concern transitions between energy levels with  $\Delta f_z = 0$ , for example from  $|\alpha\beta\rangle$  to  $|\beta\alpha\rangle$  and vice versa. Both kinds of transitions are not allowed using selection rules developed by using first order perturbation theory, as we saw from Eq.( 10 ), but it does not mean that they do not occur in reality. In fact magnetization transfer and Nuclear Overhauser Effect (NOE) involve double and zero quantum transitions (25). Zero and double quantum coherences cannot be measured directly through the application of operators like  $I_+$  and  $I_-$  but, under certain types of NMR sequences (for example NOESY (25)), they produce measurable changes in observables.

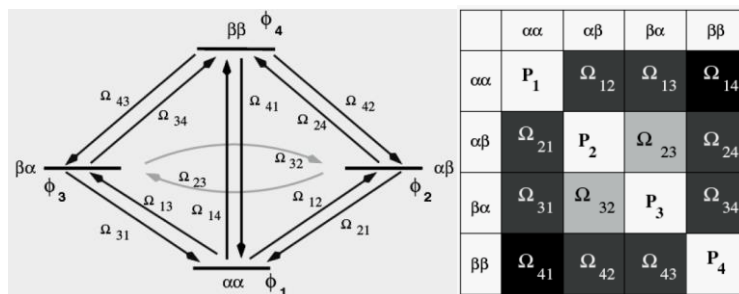


Fig. 17: connections between transitions and density matrix elements for a 2-spins system, using standard basis functions  $\phi_k$ .

After the application of the  $\frac{\pi}{2}$  pulse, the system changes due to Hamiltonian evolution, for example considering weak j-coupling between the nuclei:

$$H = -\omega_I I_z - \omega_S S_z + 2\pi j I_z S_z$$

$$\begin{aligned} \rho_1(0) = -I_y - S_y &\xrightarrow{t} \rho_1(t) \\ &= e^{i(\omega_I I_z + \omega_S S_z - 2\pi j I_z S_z)t} (-I_y - S_y) e^{-i(\omega_I I_z + \omega_S S_z - 2\pi j I_z S_z)t} \end{aligned}$$

The calculation of the matrix elements of the operators is quite a tedious task: it can be done evaluating them one by one, since we are working on the regular basis  $\phi_k$  whose elements are eigenvectors of  $I_z$  and  $S_z$ . Considering then Schrödinger equation on  $\rho_1(0) = -I_y - S_y$ , we have:

$$\frac{d\rho_{nm}}{dt} = -i(\omega_n - \omega_m)\rho_{nm}$$

Using the values in Table 2, we obtain for example:

$$\rho_{13} = c_1 c_3^*(t) = c_1 c_3^*(0) e^{i(+\omega_I - \pi j)t}$$

And thus, here it is the complete matrix:

$$\rho_1(t) = \frac{1}{2} \begin{vmatrix} 0 & ie^{i(+\omega_S - \pi j)t} & ie^{i(+\omega_I - \pi j)t} & 0 \\ -ie^{i(-\omega_S + \pi j)t} & 0 & 0 & ie^{i(+\omega_I + \pi j)t} \\ -ie^{i(-\omega_I + \pi j)t} & 0 & 0 & ie^{i(+\omega_S + \pi j)t} \\ 0 & -ie^{i(-\omega_I - \pi j)t} & -ie^{i(-\omega_S - \pi j)t} & 0 \end{vmatrix}$$

We can now measure the x-y magnetization through quadrature detection:

$$\rho_1(t)I_+ = \frac{1}{2} \begin{vmatrix} 0 & ie^{i(+\omega_S - \pi j)t} & ie^{i(+\omega_I - \pi j)t} & 0 \\ -ie^{i(-\omega_S + \pi j)t} & 0 & 0 & ie^{i(+\omega_I + \pi j)t} \\ -ie^{i(-\omega_I + \pi j)t} & 0 & 0 & ie^{i(+\omega_S + \pi j)t} \\ 0 & -ie^{i(-\omega_I - \pi j)t} & -ie^{i(-\omega_S - \pi j)t} & 0 \end{vmatrix} \begin{vmatrix} 0 & 0 & 1 & 0 \\ 0 & 0 & 0 & 1 \\ 0 & 0 & 0 & 0 \\ 0 & 0 & 0 & 0 \end{vmatrix}$$

$$\rho_1(t)I_+ = \frac{1}{2} \begin{vmatrix} 0 & 0 & 0 & ie^{i(+\omega_S - \pi j)t} \\ 0 & 0 & -ie^{i(-\omega_S + \pi j)t} & 0 \\ 0 & 0 & -ie^{i(-\omega_I + \pi j)t} & 0 \\ 0 & 0 & 0 & -ie^{i(-\omega_I - \pi j)t} \end{vmatrix}$$

$$\rho_1(t)S_+ = \frac{1}{2} \begin{vmatrix} 0 & ie^{i(\omega_S - \pi j)t} & ie^{i(\omega_I - \pi j)t} & 0 \\ -ie^{i(-\omega_S + \pi j)t} & 0 & 0 & ie^{i(\omega_I + \pi j)t} \\ -ie^{i(-\omega_I + \pi j)t} & 0 & 0 & ie^{i(\omega_S + \pi j)t} \\ 0 & -ie^{i(-\omega_I - \pi j)t} & -ie^{i(-\omega_S - \pi j)t} & 0 \end{vmatrix} \begin{vmatrix} 0 & 1 & 0 & 0 \\ 0 & 0 & 0 & 0 \\ 0 & 0 & 0 & 1 \\ 0 & 0 & 0 & 0 \end{vmatrix}$$

$$\rho_1(t)S_+ = \frac{1}{2} \begin{vmatrix} 0 & 0 & 0 & ie^{i(\omega_I - \pi j)t} \\ 0 & -ie^{i(-\omega_S + \pi j)t} & 0 & 0 \\ 0 & -ie^{i(-\omega_I + \pi j)t} & 0 & 0 \\ 0 & 0 & 0 & -ie^{i(-\omega_S - \pi j)t} \end{vmatrix}$$

$$\begin{aligned} M_{xy} &\propto \text{Tr}[\rho_1(t)I_+ + \rho_1(t)S_+] = \\ &= -i(e^{-i(\omega_I + \pi j)t} + e^{-i(\omega_S + \pi j)t} + e^{-i(\omega_I - \pi j)t} + e^{-i(\omega_S - \pi j)t}) \end{aligned}$$

Ignoring the  $-i$  phase and the sign of the angular frequencies we have:

$$M_{xy} \propto e^{i(\omega_I + \pi j)t} + e^{i(\omega_S + \pi j)t} + e^{i(\omega_I - \pi j)t} + e^{i(\omega_S - \pi j)t}$$

By inserting a transverse relaxation damping (see section 1.5) we obtain:

$$M_{xy} \propto (e^{i(\omega_I + \pi j)t} + e^{i(\omega_S + \pi j)t} + e^{i(\omega_I - \pi j)t} + e^{i(\omega_S - \pi j)t})e^{\frac{t}{T_2}}$$

Fourier transformation of those exponentials would produce Lorentzian (due to the damped exponential) doublet of doublets spectral pattern, like the one previously showed in Fig. 14.

## Strong Coupling

The formalism developed so far is directly applicable to strong coupled systems by making a basis change from standard functions  $\phi_k$  to the eigenstates of the strong coupled Hamiltonian, the  $\psi_k$  in Eq.( 19 ). This transformation makes the algebra more difficult since the equilibrium density matrix becomes as the one displayed in Eq.( 31 ) but all the other operators have to be modified! So, it is common practice to start with a non-diagonal equilibrium matrix (thus using the basis  $\phi_k$ ), evaluate Hamiltonian time evolution by considering values in Table 3 and then do the basis change at the end of the pulse sequences, but before evaluating expected values of observables (19).

---

### 1.4.3 TWO SPINS PRODUCT OPERATORS

Writing down terms of density matrices or exponential operators, like the ones used to describe rotations caused by radiofrequency pulses, can be very tedious. In many cases it is not necessary to exactly calculate all the elements of the matrices or to write them explicitly. Expressing matrices and rotations by combinations of spin operators can be sufficient to understand changes in a spin system after a pulse sequence. To apply this formalism, called *product operators formalism*, we have to consider some rules (26):

- 1) If two operators commute, then the exponential of one of these operators commutes with the other. Consequently, rotations made with operators that commute with a density matrix have no effect on it:

$$[A, B] = 0 \implies e^{-i\theta A} B e^{i\theta A} = e^{-i\theta A} e^{i\theta A} B = B$$

- 2) Single spin components of an evolving product operator can be treated separately. For example if we want to apply a rotation of an angle  $\theta$  on the matrix  $2I_y S_z$  around x-axis:

$$2I_y S_z \xrightarrow{\text{rotation of } \theta(I_x + S_x)} 2[I_y \cos(\theta) + I_z \sin(\theta)][S_z \cos(\theta) - S_y \sin(\theta)]$$

- 3) To evaluate rotations produced by a product of operators, like the j-evolution of a pair of coupled spins, we can consider one of them as a constant in the expression:

$$e^{-i2\pi j I_z S_z t} = e^{-i(2\pi j t S_z) I_z}$$

Trigonometric functions, as the ones previously found in rule 2, have to be evaluated through the use of Taylor series, since now  $\theta = 2\pi j t S_z$  is an operator:

$$\begin{aligned} \cos(2\pi j t S_z) &= 1 - \frac{(2\pi j t)^2}{2!} S_z^2 + \frac{(2\pi j t)^4}{4!} S_z^4 + \dots \\ &= 1 - \frac{(2\pi j t)^2}{2!} \frac{\mathbf{1}}{4} + \frac{(2\pi j t)^4}{4!} \left(\frac{\mathbf{1}}{4}\right)^2 = \cos(\pi j t) \end{aligned}$$

Similarly:

$$\sin(2\pi j t S_z) = \frac{2\pi j t}{1} S_z - \frac{(2\pi j t)^3}{3!} S_z^3 + \frac{(2\pi j t)^5}{5!} S_z^5 + \dots = 2\sin(\pi j t) S_z$$

Thus, we have, for example:

$$I_x \xrightarrow{2\pi jt I_z S_z} I_x \cos(\pi jt) + 2I_y S_z \sin(\pi jt)$$

- 4) We can describe the evolution of a 2-spins product operator under j-coupling by the combination of rule 2 and 3, for example:

$$2I_x S_y \xrightarrow{2\pi jt I_z S_z} 2[I_x \cos(\pi jt) - 2I_y S_z \sin(\pi jt)][S_y \cos(\pi jt) - 2I_z S_x \sin(\pi jt)]$$

## Spin Echo

Most of the sequences used in NMR spectroscopy are based on the spin echo refocalization sequence. This pulse sequence is made by a  $90^\circ$  pulse that brings the magnetization on the x-y plane followed by a  $180^\circ$  pulse that refocus the spins that might have loss coherence during Hamiltonian evolution (this commonly happens because of field inhomogeneity). The sequence can be schematized as follows:

$$90^\circ_x \longrightarrow \tau \longrightarrow 180^\circ_x \longrightarrow \tau$$

Since we have  $[I_i, S_j] = 0$  for every  $i$  and  $j$ , for rule 1 of product operators we can process Hamiltonian evolution separately for the two spins:

$$\begin{aligned} -I_y &\xrightarrow{\omega_I \tau I_z} -\cos(\omega_I \tau) I_y + \sin(\omega_I \tau) I_x \xrightarrow{\pi I_x} \cos(\omega_I \tau) I_y + \sin(\omega_I \tau) I_x \\ -S_y &\xrightarrow{\omega_S \tau S_z} -\cos(\omega_S \tau) S_y + \sin(\omega_S \tau) S_x \xrightarrow{\pi S_x} \cos(\omega_S \tau) S_y + \sin(\omega_S \tau) S_x \\ &\cos(\omega_I \tau) I_y + \sin(\omega_I \tau) I_x \xrightarrow{\omega_I \tau I_z} I_y \\ &\cos(\omega_S \tau) S_y + \sin(\omega_S \tau) S_x \xrightarrow{\omega_S \tau S_z} S_y \end{aligned}$$

The overall effect of the sequence is to refocus the magnetization at time  $2\tau$ , eliminating the phase accumulated in time  $\tau$ . This feature is frequently used in experiments to bring the magnetization into the acquisition window, refocusing the different phases of the spins produced by the lack of spatial homogeneity of the static field  $B_0$ . Considering two coupled nuclei, we can start by considering, for example, the system in the state  $I_x + S_x$ , since the choice of the reference is arbitrary and the global phase is not an important

parameter. Moreover we can focus our treatment on the coupling term in the Hamiltonian because we already saw that the effect of spin echo on a system without coupling is to reset the phases of the nuclei, restoring the initial state of the system.

$$\begin{aligned}
 I_x &\xrightarrow{2\pi j\tau I_z S_z} \cos(\pi j\tau) I_x + 2 \sin(\pi j\tau) I_y S_z \xrightarrow{\pi I_x} \cos(\pi j\tau) I_x \\
 &\quad - 2 \sin(\pi j\tau) I_y S_z \xrightarrow{\pi S_x} \cos(\pi j\tau) I_x + 2 \sin(\pi j\tau) I_y S_z \xrightarrow{2\pi j\tau I_z S_z} \cos(2\pi j\tau) I_x \\
 &\quad + 2 \sin(2\pi j\tau) I_y S_z
 \end{aligned}$$

( 34 )

Last passage required the use of rule 4. The 180° pulse has left the spins unaffected and the evolution under j-coupling was not refocused! Similar result can be found for  $I_y$ :

$$I_y \xrightarrow{\tau-180^\circ-\tau} -\cos(2\pi j\tau) I_x + 2 \sin(2\pi j\tau) I_y S_z$$

This result has to be taken into account while working with substances that have coupled chemical groups, since the phasing of the spectrum can't be achieved so easily.

## 1.5 RELAXATION

The phenomenon of relaxation occurs due to loss of coherence between spins, for the purposes of this work only simple principles of spin-spin relaxation and spin-lattice relaxation will be explained; treatment of other effects, like cross-relaxation or Nuclear Overhauser Effect, is beyond the purposes of this work.

### 1.5.1 SPIN-LATTICE RELAXATION

Spin-lattice relaxation involves the loss of energy that passes from the nuclei, excited with radiofrequency pulses, to the lattice until the thermal equilibrium is reached. This process of decoherence is characterized by a time constant  $T_1$ .  $T_1$  quantifies the rate at which the longitudinal component of magnetization  $M_z$  returns to its equilibrium value, determined by Boltzmann distribution in Eq.( 9 ).

In general we have:

$$M_z(t) = M_{z,eq} - [M_{z,eq} - M_z(0)]e^{-t/T_1}$$

In particular, after a  $90^\circ$  pulse that brought the magnetization on the  $xy$ -plane:

$$M_z(t) = M_{z,eq}(1 - e^{-t/T_1})$$

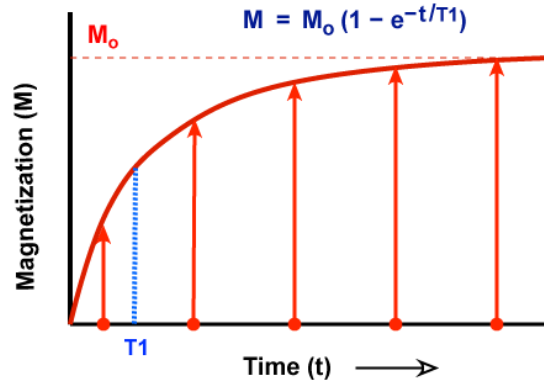


Fig. 18: Spin-lattice relaxation after a  $90^\circ$  pulse, the magnetization recovers from the  $x$ - $y$  plane and returns to its equilibrium value on the  $z$ -axis.

The relaxation time  $T_1$  can be considered the average lifetime of nuclei in the higher energy state. It depends on the gyromagnetic ratio of the nucleus and the mobility of the lattice: the vibrational and rotational motions can absorb energy from spins if their frequencies correspond to the energy gap between states (determined by the Larmor frequency). This fact can be understood better by considering BPP theory of relaxation (19). Considering biological applications of NMR, different tissues have different  $T_1$  values. For example, fluids have long spin lattice relaxation (1500-2000 ms), since rotational motions of molecules have frequencies sufficiently greater than the Larmor ones. Water based tissues are in the 400-1200 ms range, while fat based tissues are in the shorter 100-150 ms range. The presence ferromagnetic or paramagnetic ions or particles can strongly alter  $T_1$ , making it decrease.



---

## 1.5.2 SPIN-SPIN RELAXATION

The spin–spin relaxation is the mechanism, in which, the transverse component of the magnetization vector  $M_{xy}$ , exponentially decays towards its equilibrium value, this process is called *Free Induction Decay* (FID). The decay of the signal is characterized by a time constant  $T_2$ , known as the spin–spin relaxation time. For example, by considering a spin system on the x-y plane, after the application of a  $90^\circ$  pulse, the transverse component of the magnetization decays as follows:

$$M_{xy}(t) = M_{xy}(0)e^{-t/T_2}$$

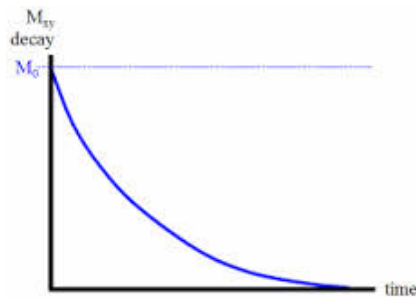


Fig. 19: Exponential decay of transverse magnetization over time.

Transverse relaxation is produced by dephasing of the spins that rotate with different Larmor frequencies in the x-y plane. Relative phases accumulated during rotation create a destructive interference between them. This phenomenon can be understood by looking at Fig. 20:

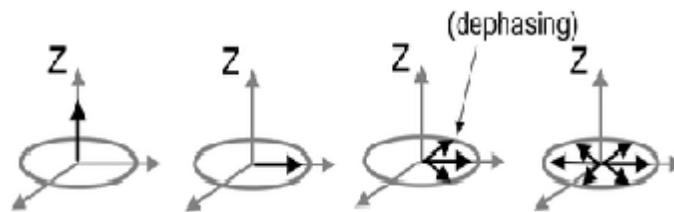


Fig. 20: Dephasing of the spins in the x-y plane produced destructive interference and loss of signal.

Mainly, two factors contribute to the decay of transverse magnetization:

1. Molecular interactions (pure  $T_2$  molecular effect): Excited nuclear spins, brought in the x-y plane, interact with each other by experiencing local magnetic field variations. This happens due to short-lived interactions such as collisions and diffusion. Usually, all the rotational or vibrational motions with  $\omega \leq \omega_{Larmor}$  contributes to spin-spin relaxation (27).
2. Lack of homogeneity in  $B_0$  (inhomogeneous  $T_2$  effect): nuclei that perceive different static  $B_0$  fields, due to imperfect shimming of the magnet, rotate at different Larmor frequencies. In clinical applications, the loss of phase is mainly due to this phenomenon.

Moreover, since in most cases  $T_2 \leq T_1$  (27), many factors that alter  $T_1$  (like the presence of ferromagnetic or paramagnetic substances) alter  $T_2$  too.

It is common practice to consider the time constant relative to the molecular effects as the “true”  $T_2$ . The apparent  $T_2$  resulting from combination of molecular effects and inhomogeneity of  $B_0$  is called  $T_2^*$  and can be expressed in terms of  $T_2$  and  $T_2^{in ho.}$  as follows:

$$\frac{1}{T_2^*} = \frac{1}{T_2} + \frac{1}{T_2^{in ho.}}$$

( 35 )

Effects of field inhomogeneity can be compensated through the use of pulse sequences based on spin-echo, since a group of spins that gained relative phases during a time  $\tau$ , will be refocused, after the application of a  $180^\circ_x$  pulse at time  $2\tau$  (see Fig. 21). On the other hand effects of molecular interaction and diffusion will not be canceled, since these events are mainly random and non-repetitive.

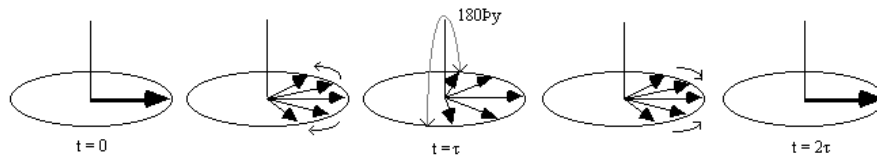


Fig. 21: Re-phasing of the magnetization in a spin-echo sequence.

After the pulse sequence displayed in Fig. 21, from a set of magnetically equivalent nuclei, we will measure a signal proportional to the one in Eq. ( 30 ). Considering a

generic phase term  $e^{i\varphi}$  and ignoring some constants, at time  $t$  after the spin echo sequence, we will measure:

$$S(2\tau + t) = e^{i\varphi} e^{-2\tau/T_2} e^{-t/T_2^*} e^{i\Omega t}$$

The Signal at  $t=0$  is the proportional to  $e^{-2\tau/T_2}$  and not to  $e^{-2\tau/T_2^*}$ . By the use of Fourier transform we obtain the spectrum:

$$F(\omega) = e^{i\varphi} e^{-2\tau/T_2} \frac{T_2^*}{1 + [T_2^*(\omega - \Omega)]^2} + ie^{i\varphi} e^{-2\tau/T_2} \frac{(T_2^*)^2(\omega - \Omega)}{1 + [T_2^*(\omega - \Omega)]^2} \quad ( 36 )$$

The yellow part of the spectrum is a Lorentzian function centered in  $\Omega$  with a damping parameter equal to  $T_2^*$ . Its maximum value, at  $\omega = \Omega$ , is proportional to  $e^{-2\tau/T_2}$  and depends on the echo time of the spin-echo sequence. When we acquire this part on the real part of the magnetization signal (that for operator  $M_{xy}$  is  $M_x$ ) the spectrum is said to be in *absorption mode* (Fig. 22 top). Absorption mode acquisition is preferred to the *dispersion mode* (green part of Eq.( 36 ), Fig. 22 bottom ), since the peaks are more visible to the user. Absorption mode acquisition can be fully achieved for singlets, through correct preprocessing or post processing (phasing) of the spectrum, while for weakly j-coupled multiplets it can be achieved only for certain echo times ( $2\tau = k\pi/j$  where  $k$  is an integer, look at Eq.( 34 )).

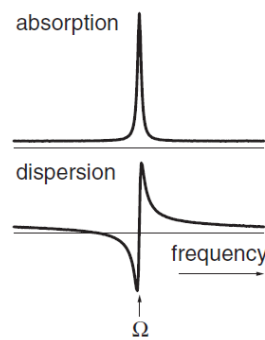


Fig. 22: Absorption (top) and dispersion (bottom) line-shapes of an NMR spectrum.

## 1.6 HOW THE SPECTROMETER WORKS

In this section a brief description of some parts of a common NMR spectrometer is provided, further technical details are beyond the purpose of this work.

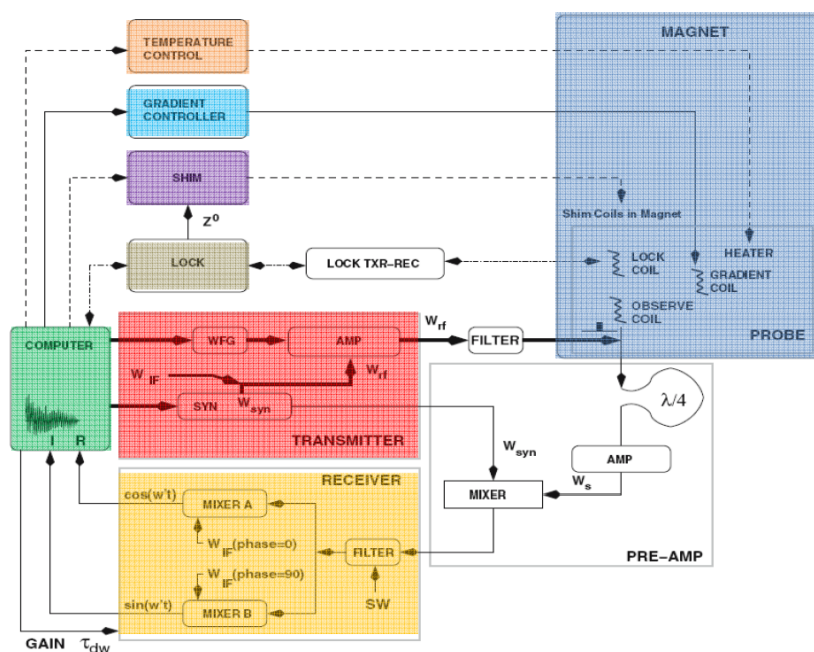


Fig. 23: Scheme of a common spectrometer and its individual components.

### 1.6.1 MAGNET AND SHIM COILS

Modern spectrometers use persistent and superconducting magnets to produce high static magnetic fields. Such fields are generated by superconducting coils in which very intense currents pass without resistance when a critical temperature is reached. These temperatures are generally below  $6^\circ \text{K}$  and to achieve superconducting state the wires are put in a bath of liquid helium. To keep the liquid helium isolated from the external environment there is another compartment filled with liquid nitrogen at approximately  $77^\circ \text{K}$  that works as a “heat shield”. Obviously the sample is maintained at room temperature and is isolated from the magnet. Superconductive currents and the cryogenic systems are usually never switched off to avoid boiling of the liquid helium and the consequent quench of the magnet. From section 1.5.2 and Eq. ( 36 ), we saw that in absorption mode the signal is a Lorentzian function with an Full Width at Half Maximum (FWHM) proportional to  $T_2^*$ . Since the  $T_2^*$  decay parameter depends mostly by the

homogeneity of  $B_0$ , an accurate shim of the static field must be achieved to have a sufficient spectral resolution (Fig. 24). Shim coils work together with the main magnet to compensate local field differences in the volume of interest.

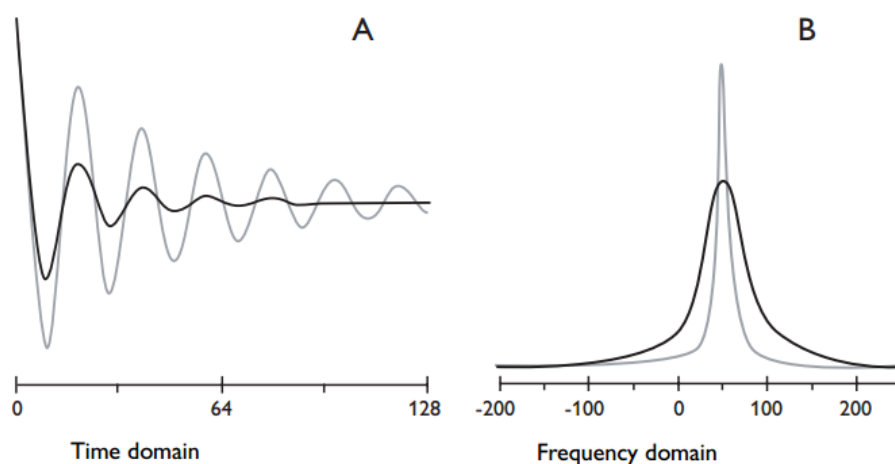


Fig. 24: Effects of shimming on the water signal in time (A) and frequency domain (B). The black curve corresponds to a signal obtained with a poor shim. Gray curve corresponds to a signal obtained with a better shim of the magnet.

---

### 1.6.2 SPECTROMETER FREQUENCY

A 3T  $H^1$ -MRS spectrometer is said to work at  $\sim 127.8$  MHz, this fact does not mean that the system is capable only to excite or receive electromagnetic waves of that frequency, it is a feature related to electronics of the spectrometer and the ADC converter. It is not convenient to sample a FID signal from 0 to 200 MHz, since the nuclei we are interested in have chemical shift differences of few KHz. This problem can be solved by the use of a mixer: this electronic component (see Fig. 23) mixes the FID with an oscillating wave and makes the resulting signal pass through a low-pass filter to subtract a reference frequency and optimize in this way the use of channels of the ADC converter:

$$\begin{aligned}
 \text{signal} &\propto \cos(\omega t) \xrightarrow{\text{signal passes through mixer}} \cos(\omega t) \cos(\omega_{ref} t) \\
 &= \frac{1}{2} \{ \cos[(\omega - \omega_{ref})t] + \cos[(\omega + \omega_{ref})t] \} \\
 &\xrightarrow{\text{low-pass filter}} \frac{1}{2} \cos[(\omega - \omega_{ref})t]
 \end{aligned}$$

---

### 1.6.3 RECEIVER AND QUADRATURE DETECTION

To determine if a detected compound has a positive or a negative frequency shift respect to the reference, the detection of two transverse components of magnetization is needed (quadrature detection), since cosine function do not discriminate between positive and negative arguments. Sometimes the use of two distinct coils provides technical difficulties in the arrangement of the experiment but the use of mixers can solve this problem. With reference to Fig. 23, we can take the filtered signal from the first mixer and make it pass through mixer A and mixer B and then filter the high frequency component:

$$\begin{aligned} & \cos[(\omega - \omega_{ref})t] \xrightarrow{\text{mixer A}} \frac{1}{2} \cos[(\omega - \omega_{ref})t] \\ & \cos[(\omega - \omega_{ref})t] \xrightarrow{\text{mixer B}} -\cos[(\omega - \omega_{ref})t] \sin(\omega_{ref}t) \\ & = \frac{1}{2} \{-\sin[(\omega + \omega_{ref})t] + \sin[(\omega - \omega_{ref})t]\} \\ & \xrightarrow{\text{low-pass filter}} \frac{1}{2} \sin[(\omega - \omega_{ref})t] \end{aligned}$$

In this way we obtain information about the sign of  $(\omega - \omega_{ref})$  with the use of a single receiver coil, since the sine function discriminates between positive and negative arguments.

---

### 1.6.4 SPECTRAL WIDTH AND RESOLUTION

Spectrum is obtained from Discrete Fourier Transform (DFT) of the FID signal:

$$S_j = FID_k \sum_{k=0}^{N-1} \cos\left(\frac{2\pi jk}{N}\right) + i \sin\left(\frac{2\pi jk}{N}\right)$$

DFT transformation is a very time-consuming algorithm with  $t \propto N^2$  and it is usually replaced by Fast Fourier Transform (FFT) (28), whose execution time is rather proportional to  $N \cdot \ln(N)$ . By Fourier transforming the signal, the bandwidth (BW) of the acquisition becomes:

$$BW = \frac{1}{t_s}$$

Where  $t_s$  is the sampling time of the FID, consequently the spectral resolution  $\Delta\nu$  becomes:

$$\Delta\nu = \frac{1}{t_{ac}}$$

Where  $t_a$  is the total acquisition time of the FID. We know from Nyquist theorem that the bandwidth should be greater than the double of the greatest frequency sampled ( $BW > \nu_{max}$ ). Since sampled frequencies are shifted by spectrometer frequency by the use of mixers, band-pass filters are commonly used in all the spectrometers to avoid aliasing.

Effective spectral resolution is usually determined, at least in clinical spectrometers, by the  $T_2^*$  decay parameter (see Fig. 25), thus by the homogeneity of the static field. Consequently, in many cases the use of 1024 or 2048 points in frequency domain (with the same bandwidth) produces similar results due to intrinsic resolution of the signal.

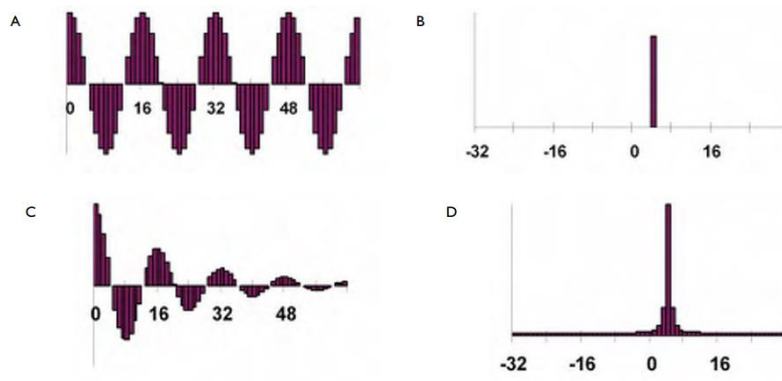


*Fig. 25: Sampled FID with transverse decay can have intrinsically less spectral resolution than the one set by the user.*

## 1.7 GENERAL DESCRIPTION OF PULSE SEQUENCES

### 1.7.1 LOCALIZATION PULSES AND GRADIENTS

In MRS there is the necessity of acquiring the signal from a well-defined volume of space, this can be achieved with the use of gradients and RF localization pulses. For example if we want to make flip on the x-y plane only the spins contained in a certain voxel, we can apply a series of field gradients to change the resonance frequency of the nuclei:

$$\omega_0(x, y, z) = \gamma(B_{z0} + G_z z + G_x x + G_y y)$$

In this way, each location in the space inside the bore of the scanner has a typical Larmor frequency that can be excited to bring the magnetization on the transverse plane. Considering for simplicity only one coordinate, it is possible so select a slice of thickness  $\Delta z$  of the total volume by sending a non-selective  $90^\circ$  RF pulse with a bandwidth of  $G_z \Delta z$ :

$$\omega_0(z) = \gamma(B_{z0} + G_z z)$$

$$\Delta z = \frac{\Delta\omega - \gamma B_{z0}}{\gamma G_z}$$

### 1.7.2 STIMULATED ECHO ACQUISITION MODE (STEAM)

STEAM is a single-shot localization sequence. The scheme of the pulse sequence can be found in Fig. 26. It consists of three  $90^\circ$  RF pulses in association with field gradients, a combination which originates a stimulated echo (STE) (29) which is recorded. STEAM is the best choice when small echo time are needed since it makes use only of  $90^\circ$  pulses which are shorter than  $180^\circ$  ones ( $\theta = \gamma B_1 t$ ). The mixing time (TM), is a period during which magnetization transfer between the spin systems is allowed through NOE cross-relaxation, if cross-relaxation is not investigated (like in our case) TM can be shortened almost to zero. As it can be viewed in Fig. 26, the stimulated echo is generated after a TE + TM delay. Application of the  $90^\circ$  pulses produces 3 FIDs and 2 echoes (29) before the STE is generated, superimposition of these signals to the STE is avoided with the use of crusher gradients that dephase the nuclei whose magnetization is located on the x-y plane after the two  $90^\circ$  pulses.



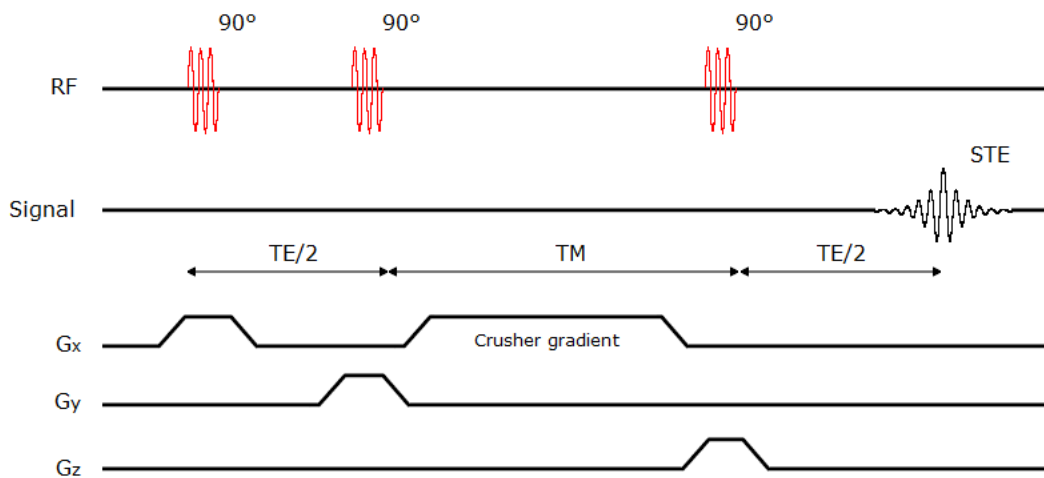


Fig. 26: Scheme of a basic STEAM pulse sequence.

It can be shown that the amplitude of a STE is expected to be half of the equilibrium magnetization value  $M_0$  (29) notwithstanding relaxation and diffusion effects. This happens because the second  $90^\circ$  pulse only rotates half of the transverse magnetization to the longitudinal plane, while the other half is dephased by the crusher gradients. Thus, the use of this method implies a decreased SNR by a factor of 2 respect to pulse sequences like PRESS which is briefly described in the next paragraph.

### 1.7.3 POINT RESOLVED SPECTROSCOPY SEQUENCE (PRESS)

PRESS is a single-scan sequence based on spin echo. With reference to Fig. 27, the initial  $90^\circ$  pulse selects the slice of interest while the first  $180^\circ$  pulse refocuses the spins of the nuclei located in the intersection between the slices perpendicular to  $z$  and  $y$ . The first echo appears at time  $t = TE_1$  and it is dephased by a crusher gradient. Then, after the second  $180^\circ$  pulse the magnetization is refocused again at time  $t = TE_1 + TE_2$ . The second echo contains signal from the intersection of slices perpendicular to  $z$ ,  $y$  and  $x$ , as shown in Fig. 28.

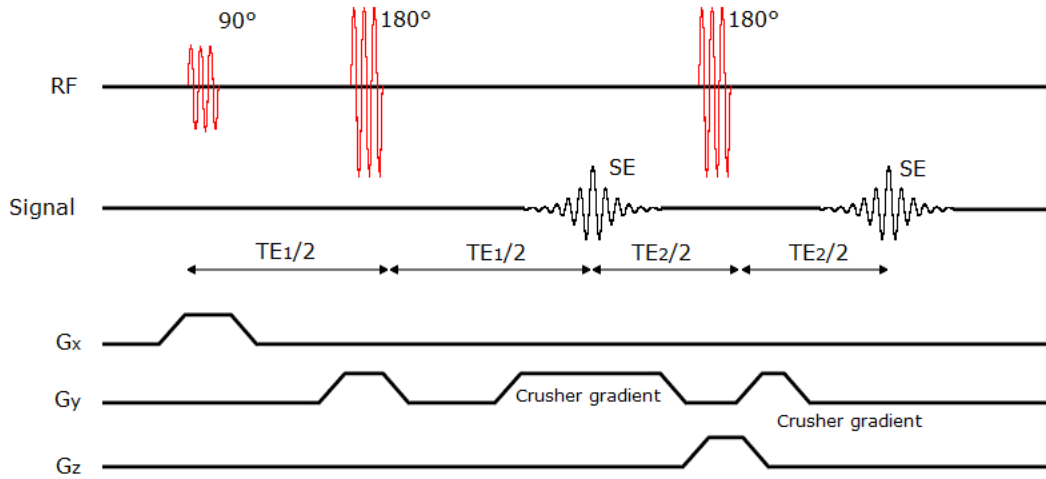


Fig. 27: Scheme of a basic PRESS pulse sequence.

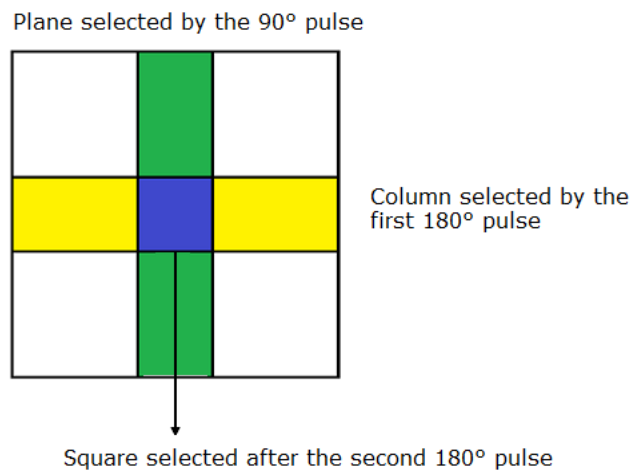


Fig. 28: 2-D representation of the voxel selection in a PRESS sequence.

In this work the PRESS sequences used are all symmetric with  $TE_1 = TE_2 = TE/2$ . PRESS is the most used sequence in clinical MRS since it produces a signal that is approximately two times greater than STEAM, so it is the most appropriate sequence to obtain spectra in low SNR conditions.

---

### 1.7.4 CHEMICAL SHIFT SELECTIVE SEQUENCE (CHESS)

CHESS is a water suppression technique that eliminates the water (or fat) signal before other acquisition sequences. Through the use of three chemical shift selective pulses of  $90^\circ$  (see Fig. 29), this sequence brings the spins of water in a transverse plane respect to other compounds and dephases the residual magnetization with the crusher gradients. Selective  $90^\circ$  pulses are centered on the frequency of the compound we want to remove from the spectrum ( $\sim 4.7$  ppm for water) and their bandwidth is a parameter of the sequence. With a poor shim of the static field,  $T_2^*$  of water is shortened, consequently a larger bandwidth for CHESS  $90^\circ$  pulses has to be set to remove the water signal from spectrum.

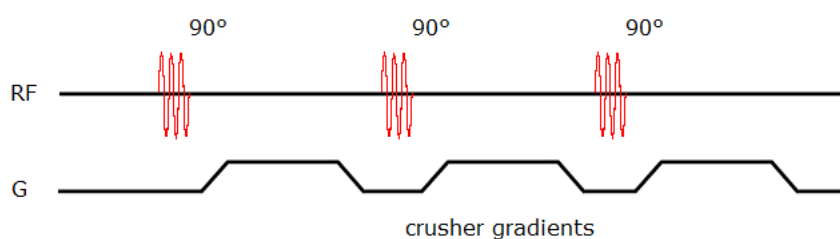


*Fig. 29: Scheme of a CHESS sequence for water suppression.*

---

### 1.7.5 BASING PULSE

A BASING pulse is used for frequency selective suppression by dephasing the excited signal with spoiler gradients, while leaving signals from other nuclei unaffected. The BASING pulse adds two gradients and a frequency selective inversion pulse during the echo time of a localization sequence. The inversion pulse has to be applied for a certain inversion time and gradients should be applied for a sufficiently long interval  $\tau$  to dephase correctly the signal. As a result, the shortest possible available TE increases. BASING pulses can be added to any localization sequence with sufficiently long echo time, to serve as water or fat suppression method.

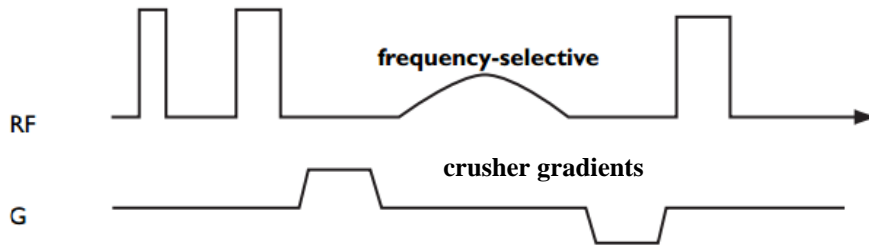


Fig. 30: Scheme of a BASING pulse inserted in a PRESS sequence.

In Fig. 30 there is a graphical scheme of the BASING pulse added into a PRESS sequence. A crusher gradient is applied for a time  $\tau$ , after the first  $180^\circ$  pulse, to dephase all the spins in the selected volume. After that, a frequency selective inversion pulse is sent to the sample inverting only the spins selected (for example water). Next, a second gradient is applied for a time  $\tau$ , with equal magnitude but opposite in sign. The spins are thus refocused, except the ones previously inverted by the RF pulse. These dephased spins will not generate echo signal after the second  $180^\circ$  pulse of the PRESS sequence.

$$\text{relative phase of not selected spins} = e^{-iG \cdot r \tau} e^{+iG \cdot r \tau} = 1$$

$$\text{relative phase of selected spins} = e^{-iG \cdot r \tau}$$

Since STEAM uses very short echo times, application of the BASING pulses in these sequences is usually foreclosed.

---

## 1.7.6 Other important parameters in pulse sequences

### Iterative Shimming

This technique consists on the repetitive acquisition of water spectra to optimize the homogeneity of the static field. At each iteration, shimming fields are adjusted to minimize the FWHM of the water peak.

### NSA

The NSA is the Number of Signal Averaged to obtain a better signal to noise ratio during an acquisition. Increasing NSA in a pulse sequence will lead to a better quality of the spectrum but will increase execution time too, this fact imposes limitations of the possible number of averages during in vivo acquisitions.

## Phase cycles

Phase cycles are used in advanced NMR to set a predetermined coherence pathway, in clinical spectroscopy it is commonly used to compensate for the imperfections in  $180^\circ$  pulses (30).

## Gradient spoiling

Gradient spoiling is used to compensate for incomplete magnetization recovery. In system with long relaxation times magnetization might not return to equilibrium from an acquisition to one other. Thus, forced dephasing of the transversal magnetization through spoiler gradients is needed to avoid unwanted  $T_1$ -weighting of the signal.

## SAR

SAR, the Specific Absorption Rate, is the mass normalized rate at which RF power is coupled to biological tissue and is typically indicated in units of watts per kilogram (W/kg). SAR value depends on the strength of the RF field and can be evaluated by this formula:

$$SAR = \int_{sample} \frac{\sigma(\mathbf{r})E_{RMS}(\mathbf{r})}{\rho(\mathbf{r})} d\mathbf{r}$$

Where  $\sigma(\mathbf{r})$  is the electrical conductivity of the tissue,  $E_{RMS}(\mathbf{r})$  the root mean square of the electrical field and  $\rho(\mathbf{r})$  is the density of the tissue in point  $\mathbf{r}$ . Values of SAR are automatically calculated by the MR scanner by inserting the weight of the patient and should be kept low (below  $\sim 2$  W/kg) for in vivo acquisitions to avoid local heating.

## PNS

The Peripheral Nerve Stimulation occurs when high values of gradient fields and high switching rates are used. Stimulation provokes involuntary muscular contractions, this happens when high gradients are applied with frequencies similar to the ones used by neurons for transmitting signals which are about 1-70 Hz. To avoid nerve stimulation low-varying gradients (low values of  $\frac{\partial B}{\partial t}$ ) should be used in in vivo acquisition.

## 2 MATERIALS AND METHODS

All the measurements for this work were made at IRST (Istituto per lo Studio e la Cura dei Tumori) with the collaboration of the medical physics unit and the biological laboratory. Test phantoms were constructed in the laboratories, while MRS spectra of healthy volunteers and phantoms were acquired with the new Philips Ingenia 3T scanner, one of the most advanced and recent instruments for clinical NMR. We needed a full week training course, provided by Philips Healthcare, and a lot of practice with the sequences to correctly configure the experiments. This chapter is divided as follows:

- In section 2.1 some innovative features of the spectrometer are described, like the MultiTrasmit technology that is fundamental to obtain a homogenous RF excitation at 3 T.
- A brief description of the pulse sequences used for in vitro and in vivo acquisitions is also provided in section 2.5.
- In 2.4 you can find all the information about the manufacturing of the phantoms and some considerations about the incompatibility between citrate and  $\text{CuSO}_4$ .
- The description of the homemade software and the algorithms behind it can be found in section 2.3.
- The description of the other software used is located in section 2.2.

### 2.1 THE SPECTROMETER

The use of a 3T spectrometer gives some advantages in terms of quality of NMR spectra:

- Better SNR: Curie law in Eq.( 9 ) tells us that the difference in population between the upper and lower energy states, thus the magnetization itself, is proportional to  $B_0$ . This fact implies that when the longitudinal magnetization is brought on the x-y plane by the use of radiofrequency pulses, we will measure a higher signal from excited protons compared to the one of a common 1.5 Tesla magnet.

- Better spectral resolution: we know that chemical shift differences between protons of different chemical groups are proportional to  $B_0$ :

$$\nu_i = \frac{\gamma}{2\pi} B_0 (1 - \sigma_i) \rightarrow \nu_1 - \nu_2 \propto B_0 (\sigma_2 - \sigma_1)$$

This feature makes discrimination of peaks, originated from different compounds, a simpler task, since distances in frequency between nuclei are doubled, compared to the ones obtained with a 1.5 T spectrometer.

- Changes in spectral parameters of citrate: with spectral resolution provided by the 3T field in prostate spectra it is possible to distinguish peaks of choline, creatine, citrate and in some cases polyamines. An aspect that has to be considered in spectral analysis is that citrate spectrum changes a lot, in the passage from the 1.5T to the 3T static field. Since the difference in chemical shielding parameters of the methylene protons is small, at 1.5 T citrate might be seen as a singlet, due to the fact that ratio  $Q$  of Eq.( 19 ) is almost zero. At 3T, as chemical shift differences increase, the typical line-shape of a strong coupled AB spectrum of Fig. 16 can be recognized instead.

---

### 2.1.1 SCANNER PHILIPS INGENIA 3T

The MR scanner used for the in vitro and in vivo acquisition was a new Philips Ingenia 3T, one of the best clinical instruments available for MRI and MRS diagnostics nowadays. The scanner has many interesting characteristics that might be described, some of them are beyond the purpose of this work, other ones instead are under copyright (like detailed description of pulse sequences) of Philips Healthcare and without a research collaboration with the company it is almost impossible to get quantitative information. However in this section some innovative and useful characteristics of the MR scanner are supplied.



*Fig. 31: Magnet-room view of Philips Ingenia 3T MR scanner at IRST.*

General features of the MR scanner:

- Magnet system: 3T Magnet delivering a full 55 cm field of view and cooled to cryogenic temperatures by liquid helium. Typical homogeneity  $\Delta\nu_0$  at 50 x 50 x 45 cm  $\leq$  1.8 ppm.
- Patient environment: 70 cm open bore diameter, maximum weight capacity of 250 Kg.
- RF transmitter: MultiTrasmit, Patient-adaptive. Fully flexible for each source, real time feedback loop.

Receiver coils:

- Head coil for phantom acquisitions: 30 cm coverage, 15 channels, DirectDigital data sampling.



*Fig. 32: Head coil, used for all phantom acquisitions.*

- Whole-body coil for in vivo acquisitions: 200 cm maximum coverage (2 coils), 108 channels (52 per coil), flexible connections between sub-coils, Direct Digital data sampling.





*Fig. 33: Whole body coils, only one of those was used to acquire prostate spectra from healthy volunteers.*

### **MultiTrasmit RF coils**

Since the wavelengths of the radiofrequency pulses used in a 3T scanner are in the order of 1 meter (two times smaller than the ones used in a 1.5T scanner), there can be non-uniformity in the illumination of the patient's region of interest. The problem of non-uniform illumination is similar to that found while cooking a chocolate bar in a microwave oven without a rotating plate (see Fig. 34).



*Fig. 34: Non uniform cooking of a chocolate bar in a microwave oven due to the fact that the wavelength of the microwaves used is comparable to the size of the chocolate bar.*

MultiTrasmit 4D technology consists of parallel RF transmission using two independent radiofrequency amplifiers, enabling patient-adaptive RF shimming. This feature makes use of constructive and destructive interference between waves to provide adjustment of individual RF sources, thus generating a uniform field distribution and local RF deposition in each individual patient. A graphical explanation can be found in Fig. 35.

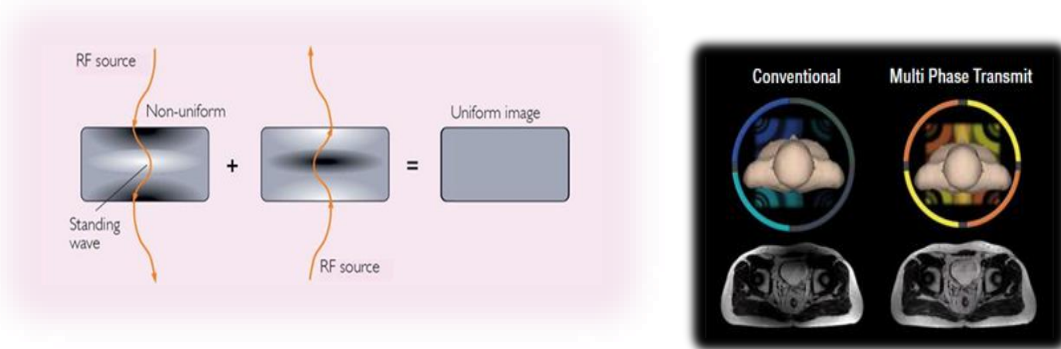


*Fig. 35: Through the use of radiofrequency waves with different phases and amplitudes the MR scanner is capable to illuminate uniformly the area of interest and produce more accurate images and spectra.*

This feature provides a better quality of prostate MR spectra, especially from multi-voxel acquisitions where the signal is more uniform from voxel to voxel. Moreover, the use of multi-phase transmitters permits to avoid the use of endorectal coil and simplify the preparation of the patient before the exam.

## **DirectDigital**

DirectDigital is another Philips technology; it consists in a miniaturized ADC converter that samples the MR signal directly in the RF coil on the patient. This configuration prevents signal loss on the cable since it is directly digitalized in the small ADC (Fig. 36) and sent through optical fibers to the console.



*Fig. 36: Miniaturized analog-to-digital converter integrated in the receiver coils captures the MR signal at its purest form and transmits data through the fiber-optic chain.*

## 2.2 SOFTWARE FOR SPECTRAL ANALYSIS

### 2.2.1 EXISTING SOFTWARE SOLUTIONS TAKEN INTO ACCOUNT

#### **SpectroView**

SpectroView is a software developed by Philips Healthcare for visualization and analysis of NMR spectra. At IRST this program is installed on the NMR console for fast visualization and elaboration of the acquired signals. The program has several scripts built up to quantify the presence of a certain metabolite inside the spectrum, at a certain TE, for different tissues, after an “appropriate” post-processing of the signal. This software was not used for the analysis of the prostate spectra, since it provided no description of the filters used for post-processing and it did not show impressive capabilities to analyze *in vivo* or *in vitro* spectra (see Fig. 37 and Fig. 38). The algorithm inside the program fits the real part of the spectrum with a linear combination of Lorentzian and Gaussian functions, ignoring completely that multiplets like citrate can't easily have a Lorentzian line-shape because of *j*-coupling. Since the results provided were controversial and the company did not give us quantitative information about how to use it better, we decided not to use it for quantitative analysis. Rather, SpectroView was used to give a first look at the acquired spectra and to export them outside the NMR console.

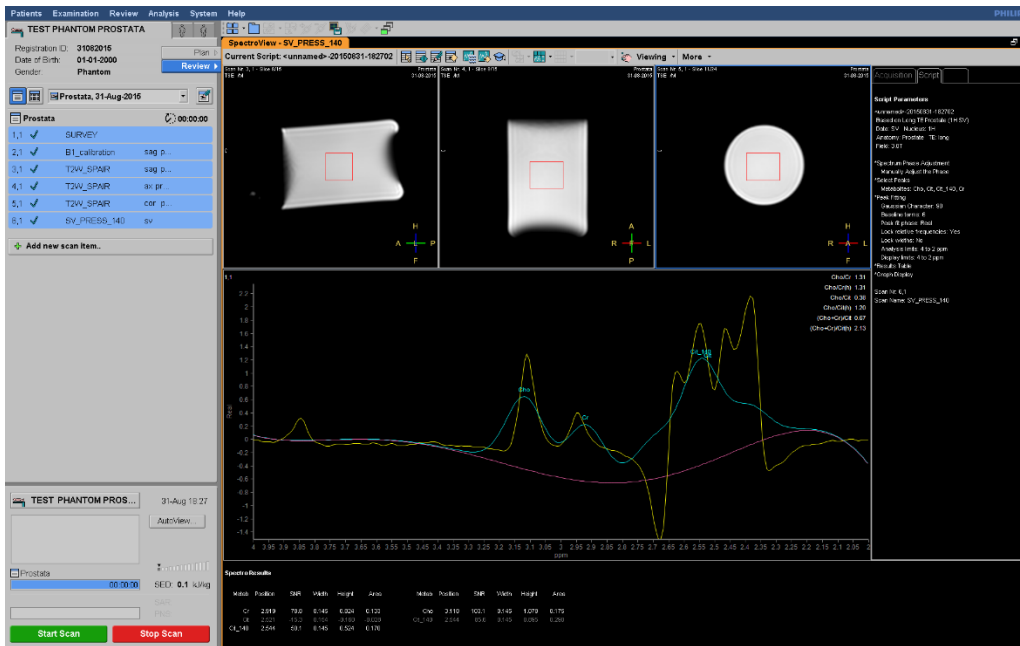


Fig. 37: Example of an analysis made with SpectroView of a homemade phantom. The program did not take into account the dispersion line-shape of citrate and made a controversial quantification.

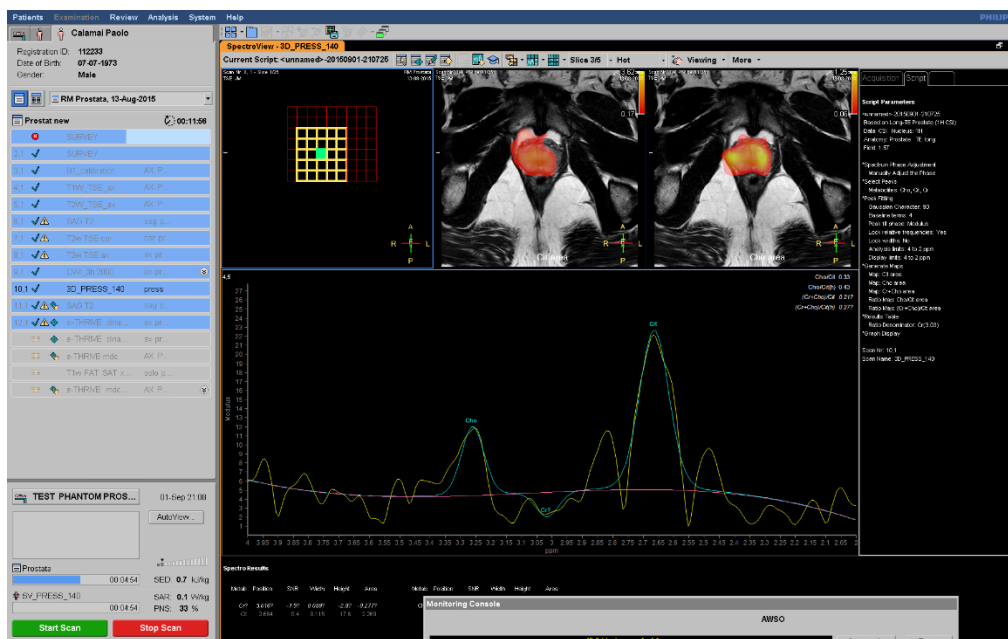


Fig. 38: Example of an analysis made with SpectroView of a prostate spectrum acquired with a multi-voxel sequence. Effects of a hidden post-processing of the signal through apodization and Gaussian smoothing can be seen by comparing it to a row spectrum file (for example the one in Fig. 107).

## jMRui

jMRui is a software package for advanced time-domain analysis of MR spectroscopy data and even MR spectroscopy imaging data. It is one of the most used software for spectral analysis due to the abundance of tools for quantification, post-processing and simulation inserted in the package. Moreover the program is freely available for registered users. In this work three features of the package were used:

- AMARES (31), which stands for Advanced Method for Accurate, Robust and Efficient Spectral fitting, is an iterative algorithm that uses nonlinear least squares method to quantify peaks from a MRS spectrum. This algorithm fits the spectrum using a linear combination of damped oscillating functions, minimizing a cost function expressed in the following way:

$$Cost\ function = G(\mathbf{c}, \alpha, \omega, \varphi) = \sum_{n=1}^{N-1} \left| y_n - \sum_{k=1}^K c_k e^{(-\alpha_k + i\omega_k)t_n + i\varphi_k} \right|^2 \quad ( 37 )$$

Where  $\mathbf{c}, \alpha, \omega, \varphi$  are the amplitudes, dampings, frequencies and phases, respectively. Prior knowledge is inserted in the analysis through a peak-picking interface (Fig. 39) where the user can select the peaks and their FWHM and insert them into the analysis.

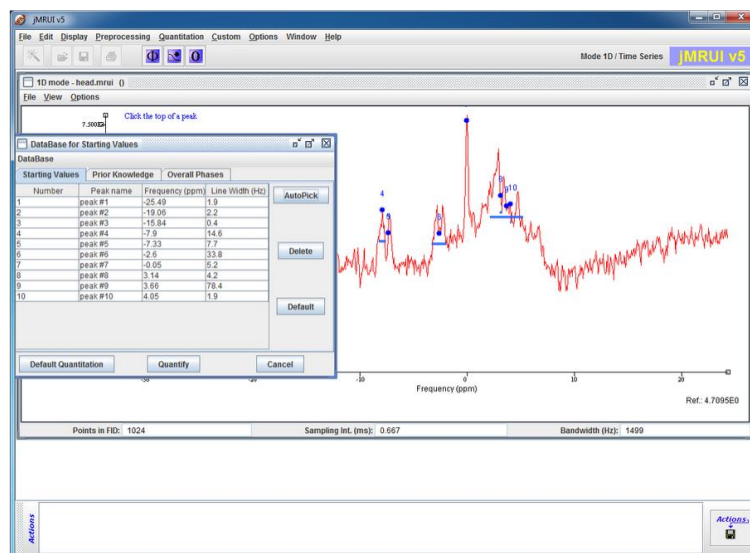


Fig. 39: Peak-picking interface for AMARES in jMRui.

From the frequency-domain point of view the algorithm fits the real part of the spectrum with a combination of Lorentzian functions, thus the fitting of a multiplet should be done with a set of peaks with a fixed ratio. Once the analysis is finished the user can estimate the quantity of a compound by the amplitude parameters  $c$  of Eq.( 37 ).

- NMRScopeB (32) is quantum-mechanical signal simulator based on numerical solution of Liouville-von Neumann equation. Through the use of this tool it is possible to build different types of spin systems (coupled, strong coupled etc.) and simulate the acquisition of the FID by configuring a pulse sequence. The simulated FIDs can be used as a basis for QUEST algorithm.

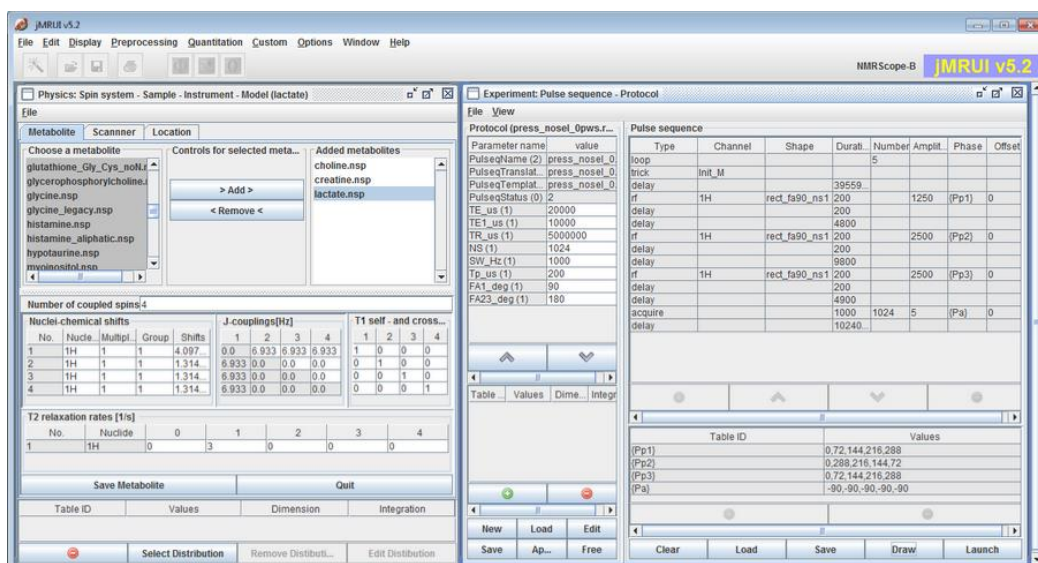


Fig. 40 : Graphical interface of NMRScopeB simulation tool, on the left side there is the environment to build up the spin system, on the right side there is the sequence configuration.

- QUEST (33), which stands for Quantum ESTimation, is a time domain algorithm which fits a weighted combination of metabolite signals directly to the in vivo data. It uses a basis set of FIDs that can be acquired in vitro or can be simulated with the use of NMRScopeB.

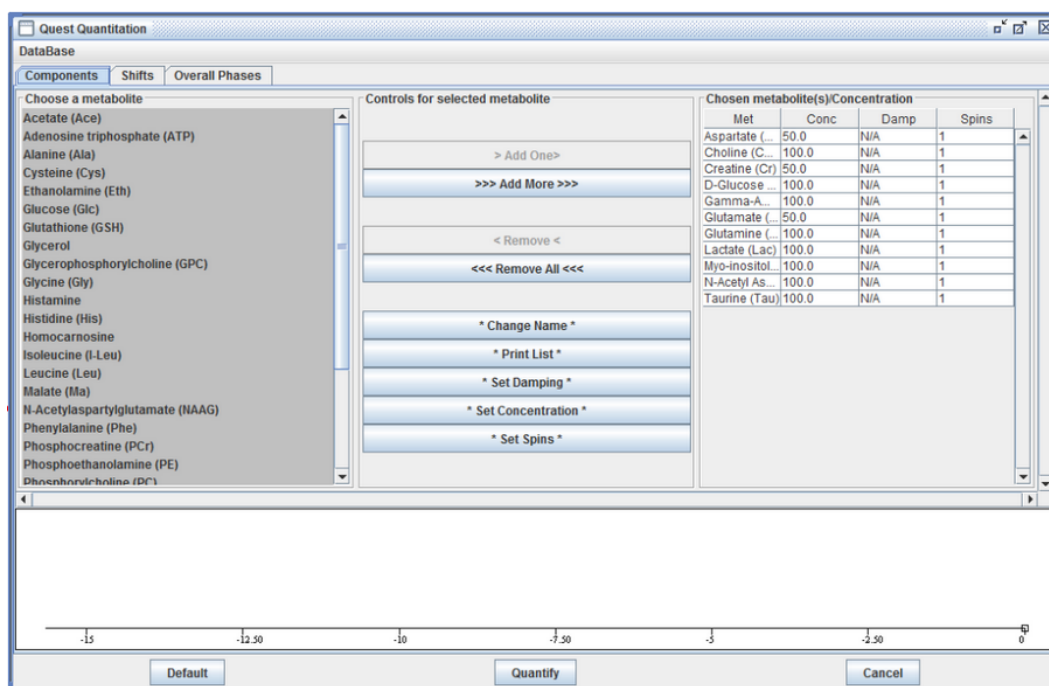


Fig. 41: QUEST quantitation start window.

## 2.3 DEDICATED SOFTWARE DEVELOPMENT

The homemade software for analysis of prostate spectra is based on the GAMMA C++ libraries (34) and on a preconditioned gradient descent algorithm. GAMMA is a package for NMR spectroscopy simulations, it uses density matrix calculations (in the formalism developed in section 1.4). Density matrix formalism is a useful tool to describe the behavior of strong coupled spins systems, like the two equivalent methylene groups of citrate. The core of the program is an iterative simulation of spectra whose parameters are changed at each iteration to correctly fit the acquired data by minimization of a cost function. An essential graphical interface is provided by the use of Fast Light ToolKit

(FLTK). Some packages of the GNU scientific libraries were also used to perform interpolations. The software works on Linux operating system and needs all the libraries to be correctly installed. All the C++ packages used for the realization of this program have a free license for non-commercial purposes and can be easily downloaded from the internet. The list of the included libraries is shown below in Fig. 42.

```
#include <gamma.h>
#include <iostream>
#include <math.h>
#include <gsl/gsl_spline.h>
#include <gsl/gsl_interp.h>
#include <stdlib.h>
#include <stdio.h>
#include <gsl/gsl_errno.h>
#include <fstream>
#include <string>
#include <limits>
#include <FL/FL.H>
#include <FL/FL_Window.H>
#include <FL/FL_Button.H>
#include <FL/FL_Progress.H>
#include <FL/FL_File_Browser.H>
#include <FL/fl_ask.H>
#include <FL/FL_Input.H>
#include <FL/FL_Box.H>
```

*Fig. 42: Included libraries for the homemade software.*

---

### 2.3.1 INPUT

As can be seen from Fig. 43, the program takes as inputs:

- Real and imaginary part of the FID from folders, in .txt format.
- A frequency file that can be substituted if a shift reference is added during the acquisition (it is used to give a reference to the Fourier transform).
- Echo time of the PRESS sequence used for acquisition.
- The bandwidth of the FID.
- Resolution, usually 1024 or 2048 points.
- The interval in ppm where the spectrum will be fitted and quantified.



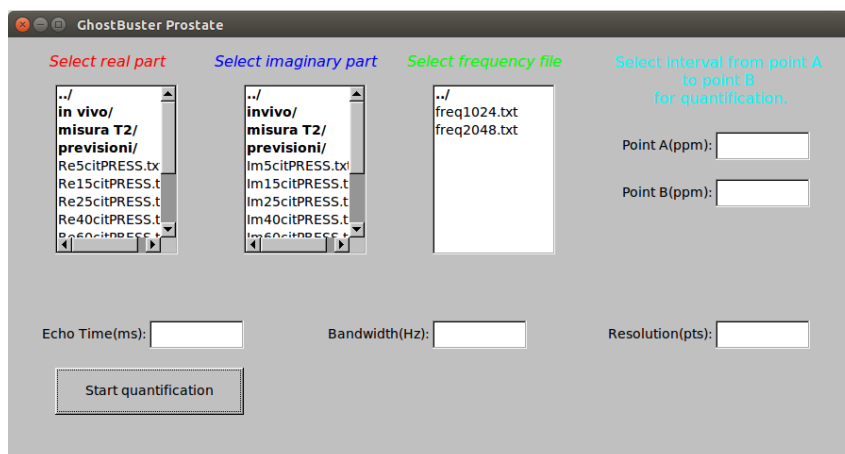


Fig. 43: Input window of the homemade software.

To simulate correctly the spin systems, the program uses text files containing the spectral parameters of the metabolites: creatine.sys, choline.sys and citrate.sys. Such files provide information about the NMR properties of the chemical groups like the number of spins, the chemical shift of the nuclei, j-coupling between them and the spectrometer frequency. An example of those files is shown in Fig. 44. Only one group among all the magnetically equivalent groups is simulated for each molecule to obtain a better computational efficiency. For example the main peak of choline is made by the sum of the signals produced by nine magnetically equivalent protons. It is more convenient to simulate only one of those and rescale the results for the real multiplicity than simulating nine protons and do calculations with  $2^9 \times 2^9$  matrices.

```

SysName (2) : citrate - Name of spin system
NSpins (0) : 2 - Number of spins in spin system
Iso(0) (2) : 1H - Spin Isotope Type
Iso(1) (2) : 1H - Spin Isotope Type

PPM(0) (1) : 2.602 - Shift of spin 0 (PPM)
PPM(1) (1) : 2.708 - Shift of spin 1 (PPM)

J(0,1) (1) : 16.8 - Scalar coupling (Hz)

Omega (1) : 127.768332 - Spec. Freq. in MHz (1H based)

spin_system sys; // System "sys"
sys.read("metabolites/citrate.sys"); // Read citrate methylene AB system
spin_system sys1; // System "sys1"
sys1.read("metabolites/choline.sys"); //Read choline methyl proton
spin_system sys2; // System "sys2"
sys2.read("metabolites/creatine.sys"); // Read creatine methyl proton

```

Fig. 44: Text file containing information about magnetic properties of one of the two equivalent methylene groups of citrate (left). Piece of code used to load the metabolites files from directories (right).

Input spectrum is smoothed before the iterative fitting process starts. Noise filtering is fundamental to correctly analyze in vivo spectra, while it can be omitted in signals acquired from phantoms. Smoothing is achieved through Lorentzian apodization, many smoothing filters were tested but the one which preserved better the peaks of metabolites was this last one. Apodization is simply achieved by multiplying the FID with a negative exponential  $e^{-At}$ , like the one which naturally multiplies the signal due to spin-spin relaxation or field inhomogeneity.

---

### 2.3.2 MINIMIZATION OF THE COST FUNCTION

Once the FID and the spin systems are given, the effect of an ideal PRESS sequence is simulated with the function PRESS in Fig. 45. This function takes as arguments the echo time, the spin system, the sampling time and the needed resolution (usually 1024 or 2048 points). Since Philips did not provide us with detailed information about the sequences, we just used ideal  $90^\circ$  and  $180^\circ$  pulses in a standard PRESS sequence. FID is sampled at the end of the sequence by using real parameters of acquisition, like the sampling time  $dt$  (the inverse of the bandwidth) and the total acquisition time  $dt \cdot tpts$  (the inverse of the spectral resolution).

```
//PRESS SEQUENCE*****
row_vector PRESS(double TE,spin_system sys,double dt,int tpts)
{
row_vector fidq(tpts);// 1D-fid block storage

gen_op H = HJ(sys)+Hcs(sys);// Hamiltonian, strong coupling
gen_op sigma; // Working density matrices
gen_op D = Fm(sys); // F- detect. op.: 0 phase
sigma= sigma_eq(sys); // Equilibrium density matrix
sigma = Ixpuls(sys, sigma,90);// Apply pi/2 x-pulse
sigma = evolve(sigma, H, TE/4);// Evolve fro TE/4
sigma =Iypuls(sys,sigma,180);// Apply a 180 y-pulse
sigma = evolve(sigma, H, TE/2);//Evolve for TE/2
sigma =Iypuls(sys,sigma,180);// Apply a 180 y-pulse
sigma = evolve(sigma, H, TE/4);//Evolve for TE/4
FID(sigma, D, H, dt, tpts, fidq);// Acquisition of FID
return fidq;
}
//*****
```

Fig. 45: Simulated ideal PRESS sequence that uses classes of GAMMA library.

The code in Fig. 45 computes the spin Hamiltonian and the equilibrium density matrix associated with it. After the application of pulses and Hamiltonian evolution, the FID is sampled through the use of the total ladder operator Fm ( $F_-$ ), that is equivalent to  $F_+$  except for a global phase term. Once the simulated FIDs have been acquired the parameters optimization starts. The parameters taken into account for the optimization are:

1. Amplitude of Cit.
2. Amplitude of Cho.
3. Amplitude of Cr.
4.  $T_2^*$  of Cit.
5.  $T_2^*$  of Cho.

6.  $T_2^*$  of Cr.
7. Global shift of Cit.
8. Global shift of Cho.
9. Global shift of Cr.
10. Relative phase of Cit.
11. Relative phase of Cho.
12. Relative phase of Cr.
13. Polynomial baseline term of order 0.
14. Polynomial baseline term of order 1.
15. Polynomial baseline term of order 2.
16. Polynomial baseline term of order 3.
17. Polynomial baseline term of order 4.

Amplitudes are scalar values that multiply the FIDs,  $T_2^*$  constants determine the width of the peaks, global shifts adjust the metabolites' chemical shifts, relative phase is needed to correctly simulate the interference between spectra of different metabolites and the polynomial baseline allows correction for eddy-currents effects (35) (although the impact of these artifacts is really small in Philips Ingenia 3T due to internal corrections). These parameters are stored in the array *double param[17]* and are all initialized to zero. All the parameters will be changed, during the optimization, to minimize a cost function named *cost1*:

```
//COST FUNCTION*****
double cost1(double x1[],row_vector y1,row_vector y11,row_vector y111, double x2[],double y2[],double a,double b,double dt,double TE,double param[],int tpts,int precision)
```

Fig. 46: Declaration of the cost function.

For brevity the code relative to this function is not showed. The cost function takes as input the FIDs, the *param* array, the frequency interval of interest, the echo time, the sampling time and the resolution. In the cost function the FIDs are firstly damped through the decay function which is of *row\_vector* type (a class of GAMMA). This last function mentioned simply performs a Lorentzian smoothing of the metabolite spectrum in time domain, by multiplying the FID with a damped exponential (see Fig. 47).

```

//T2* decay*****
row_vector decay(double T2, double dt, row_vector fid,int tpts)
{
row_vector DampedFID(tpts);
for(int i=0;i<tpts;i++)

    DampedFID(i) = fid(i)*exp(-i*dt/T2);//insert T2*| decay in the fid
return DampedFID;
}

```

Fig. 47: This function simulate the T2\* decay.

Then the FIDs are shifted in frequency by multiplying each point  $FID(t_k)$  to an oscillating function  $e^{i\Delta\omega t_k}$ . After the FIDs are transformed by FFT the simulated spectrum is evaluated in this way:

$$S_l^{tot} = \left| \sum_{k=1}^3 S_k a_k e^{i\varphi_k} \right| + c_0 + c_1 x_l + c_2 x_l^2 + c_3 x_l^3 + c_4 x_l^4$$

Where  $S_k$  is the complex spectrum of the kth metabolite,  $a_k$  is its amplitude,  $\varphi_k$  its relative phase and the  $c_0 \dots c_4$  are the coefficients of the polynomial baseline. Consequently, the cost is evaluated by the sum of the square of the differences between the modulus of the simulated spectrum and the modulus of the acquired one; evaluating differences between absolute values allows to ignore the global phase of the system. To avoid binning errors in the computation of the cost, spline interpolation (36) was used and the differences were evaluated by oversampling the two distributions on  $3(b - a)/R$  points, where  $b$  and  $a$  define the frequency interval of the analysis in ppm and  $R$  is the resolution inserted into the starting window. Finally the cost1 function returns the cost as a *double* type variable.

## Starting values

Optimization of parameters starts with a rough exhaustive search of optimal amplitude values and relative phases, with the decay constants initially set to 200 ms and all the other parameters set to zero. This first rough optimization is crucial because changes in the gain of the spectrometer can make the recorded signals pass through many orders of magnitude. Starting values for amplitudes are computed by comparing the mean of the absolute value of the simulated metabolites to the mean of the input spectrum:

$$starting\ amplitude\ (i) = \frac{mean\ value\ of\ the\ acquired\ spectrum}{mean\ value\ of\ the\ simulated\ metabolite's\ spectrum} * 2^k$$

For each  $k$  and each metabolite the cost is evaluated in a loop of for-cycles as the one described in Fig. 48; the values that minimize the cost are chosen as starting values for amplitudes.

```

int prog=0;
for(int i=1;i<=12;i++)
{
start[2]=mean/mean1*pow(2,i-6.);
  for(int j=1;j<=12;j++)
  {
    start[3]=mean/mean2*pow(2,j-6.);
    for(int k=1;k<=12;k++)
    {
      start[12]=mean/mean3*pow(2,k-6.);

      prog++;

      progress1->value(double(prog/1728.));          // update progress bar with 0.0 ~ 1.0 value
      char percent[10];

      sprintf(percent, "%d%%", int((prog/1728.)*100.0));
      progress1->label(percent);                    // update progress bar's label
      FL::check();                                  // give fltk some cpu to update the screen
      //start[15]=mean*pow(4,l-4.);polyA
      cost_start=cost1(X,data,data1,data2,XTruedata,YTruedata,a,b,dt,TE,start,tpts,precision);
      if(cost_start<=cost_start1)
      {
        cost_start1=cost_start;
        for(int r=0;r<nparam;r++)
          param[r]=start[r];
      }
    }
  }
}
}

```

Fig. 48: Loop of for-cycles to evaluate a reasonable starting amplitude for each metabolite.

A similar approach was used to estimate the starting values of relative phases.

## Gradient Descent

Gradient descent (GD) is a common iterative minimization approach which uses the gradient of a cost function to move across the parameter space to reach a minimum. GD is a commonly chosen to search minima inside parameter spaces with several dimensions: for example, an exhaustive search in a space of 17 parameters (like the one we have), with each one varying among 100 different values requires something like  $100^{17}$  iterations, a number that it is not achievable in practice. Basic gradient descent algorithm works in this way:

$$\mathbf{param}_{i+1} = \mathbf{param}_i - \alpha \mathbf{G}_i$$

Where  $\mathbf{param}_{i+1}$  is the vector containing the parameters at iteration  $i + 1$ ,  $\mathbf{G}_i$  is the gradient of the cost function at iteration  $i$  and  $\alpha$  is a numeric constant that should satisfy the Wolfe conditions (37), these conditions usually imply that  $\alpha \ll 1$ . This approach did not give satisfying results since the gradient of the previously defined cost function is

really instable and might explode to unreasonable values. Since convergence was not guaranteed with standard approach we decided to use a preconditioned gradient descent:

$$param_{i+1}[k] = param_i[k] - \frac{G[k]_i}{|G[k]_i|} dparam_i[k]$$

( 38 )

In this way only the sign of the  $k^{\text{th}}$  component of the gradient is used, while the step of the descent is “preconditioned” by the step vector **dparam**<sub>*i*</sub>. Components of the step vector were chosen empirically and some of them change during the iteration. For example, step parameters related to polynomial baseline are constant and are chosen to produce weak changes in the spectrum (with Ingenia 3T there is almost no baseline in spectra unless there is fat in the selected voxel) their value is set to be a fraction of the mean value of the acquired spectrum (Fig. 49 left). Phase and shift step parameters are static too (Fig. 49 left), while the ones related to  $T_2^*$  decays and amplitudes of metabolites update themselves at each iteration, since they are a fixed ratio of their corresponding parameters (Fig. 49 right).

```
//polynomial baseline
dparam[4]=mean/5000;
dparam[5]=mean/200000;
dparam[6]=mean/1000000;
dparam[7]=mean/1000000;
dparam[8]=mean/1000000;

//parameters to adjust chemical shift
dparam[9]=0.05;
dparam[10]=0.05;
dparam[13]=0.05;

//phase
dparam[14]=0.08;
dparam[15]=0.08;
dparam[16]=0.08;

//T2*
dparam[0]=param[0]/300;
dparam[1]=param[1]/300;
dparam[11]=param[11]/300;

//Amplitude
dparam[2]=param[2]/200;
dparam[3]=param[3]/200;
dparam[12]=param[12]/200;
```

Fig. 49: Step parameters for preconditioned gradient descent.

Step parameters are sent as input for the function void costgradient1 (Fig. 50). This function computes the gradient of the cost function as follows:

$$param\_plus_i[k] = \begin{cases} param[k] & \text{for } k \neq i \\ param[k] + dparam[k] & \text{for } k = i \end{cases}$$

$$G[i] = cost(\dots, param\_plus_i, \dots) - cost(\dots, param\_minus_i, \dots)$$

And stores the result in an array which is passed by reference to the function.

```

//GRADIENT OF COST FUNCTION*****
void costgradient1(double G[], double x1[],row_vector y1,row_vector y11, double x2[],double y2[],double a,double b,double dt,double TE,double param[],double dparam[],int tpts,int
precision)
{
double param_plus[nparam],param_minus[nparam];
for (int i=0;i<nparam;i++)
{
param_plus[i]=param[i];
param_minus[i]=param[i];
}
for (int i=0;i<nparam;i++)
{
param_plus[i]=param[i]+dparam[i];
param_minus[i]=param[i]-dparam[i];
G[i]=(cost1(x1,y1,y11,x2,y2,a,b,dt,TE,param_plus,tpts,precision)-cost1(x1,y1,y11,x2,y2,a,b,dt,TE,param_minus,tpts,precision));
param_plus[i]=param[i];
param_minus[i]=param[i];
}
}

```

Fig. 50: The function “costgradient1” computes the gradient of the cost function.

Then, after the calculation of the gradient, the iterative process starts and the parameters are updated to minimize the cost function. The core-part of the minimization algorithm is pictured in Fig. 51.

```

//GRADIENT DESCENT*****
for(int i=0; i<900;i++)
{
progress->value((i/900.0)); // update progress bar with 0.0 - 1.0 value
char percent[10];
sprintf(percent, "%d%%", int((i/900.0)*100.0));
progress->label(percent); // update progress bar's label
Fl::check(); // give fltk some cpu to update the screen

costgradient1(gradient,X,data,data1,data2,XTruedata,VTruedata,a,b,dt,TE,param,dparam,tpts,precision);

for(int j=0;j<nparam;j++)
{
if(gradient[j]!= 0.00000)
param[j]=param[j]-gradient[j]/fabs(gradient[j])*dparam[j]*4000/(2.5*t+2000);
}

cout<<"iter n"<<i<<" cost function value: "<<cost1(X,data,data1,data2,XTruedata,VTruedata,a,b,dt,TE,param,tpts,precision)<<endl;

//T2*
dparam[0]=param[0]/300;
dparam[1]=param[1]/300;
dparam[11]=param[11]/300;

//Amplitude
dparam[2]=param[2]/200;
dparam[3]=param[3]/200;
dparam[12]=param[12]/200;
}

```

Fig. 51: Minimization algorithm code.

The step parameters of Eq.( 38 ) are multiplied to a discrete hyperbolic function, which depends on the iteration number, this weighting is carried out enlarge the steps at the beginning of the iteration and do a finer optimization at the end.

---

## 2.3.4 OUTPUT

At the end of the minimization process the simulated spectrum is stored in the text file specfile.asc, while the smoothed spectrum of the input file is stored in smoothdata.asc. A “residual spectrum”, made by absolute values of differences between the smoothed and the simulated one, is also calculated and stored in residue.asc. These files are automatically plotted with gnuplot. An example of the plotted output is showed in Fig. 52.

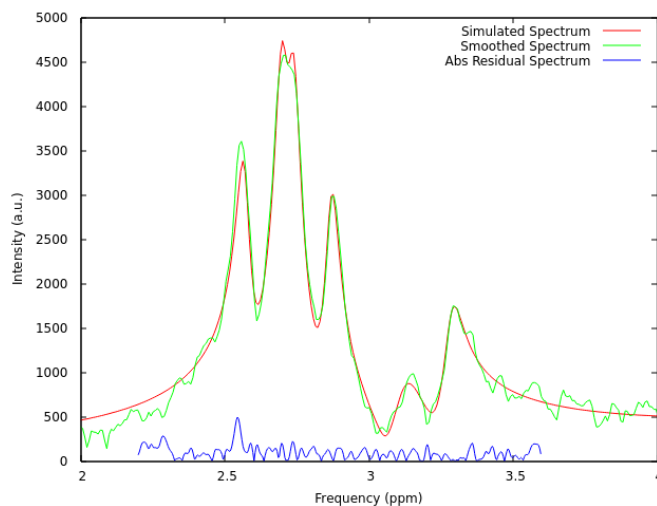


Fig. 52: Graphical output of the homemade software, quantification of an *in vivo* spectrum of a healthy volunteer with 2048 points in resolution.

Amplitudes,  $T_2^*$  decay constants and total signal (integral) of each metabolite are stored in another text file named *Results.txt* (example in Fig. 53). The amplitudes and the integral values are divided by the multiplicity of each chemical group in the metabolite of interest, to be comparable to their molar concentrations: the simulated methylene protons have a multiplicity of 2 since there are two methylene groups in a molecule of citrate, the simulated creatine and choline methyl protons have a multiplicity of 3 and 9 respectively.

```

Amplitude Citrate: 1.15816 +- 0.00579082
Amplitude Choline: 0.466458 +- 0.00233229
Amplitude Creatine: 0.584646 +- 0.00292323
T2* Citrate(ms): 46.9373 +- 0.156458
T2* Choline(ms): 52.4931 +- 0.174977
T2* Creatine(ms): 57.0803 +- 0.190268
integral Citrate= 0.145522
integral Choline= 0.0514296
integral Creatine= 0.0652462
K-S Test Output: 0.0205115 critical region around x(ppm): 3.19388
Test was done with 294 points in the interval using spline interpolation.
Critical value for 20% accord: 0.0624037

```

Fig. 53: The file *Results.txt* contains the output of the quantification process.

To assess the goodness of fit, the program uses Kolmogorov-Smirnov test (K-S Test) (38) in every quantification, which is a more robust estimate compared to the traditional Chi-square test. The maximum difference between the cumulative of the two normalized distributions, the D-Value of the K-S Test, is inserted in *Results.txt* file, accompanied by the number of points used to calculate the D-Value (equal to the ones used to evaluate the cost function) and the critical D-Value for 20% probability that differences between the two distribution might be produced by chance.



## 2.4 HOME-MADE PHANTOMS

To test the quality of the acquired spectra and to assess the accuracy of the quantifications several phantoms were built in the biological laboratories of the IRST research institute. At first we followed instruction from the report n°100 of the American Association of Physicists in Medicine (AAPM) (39) but for metabolite phantoms we encountered some unexpected technical problems and we followed other pathways.

### 2.4.1 WATER PHANTOMS WITH PARAMAGNETIC AGENT

First of all, to measure the effects of paramagnetic agents on water spectrum we realized four different water phantoms. The AAPM suggests to use NaCl concentration of  $\sim 4g/L$  to adjust solution conductivity and the paramagnetic salt  $CuSO_4$  to set the proper relaxation times. Suggested concentration of paramagnetic agent is of  $\sim 2g/L$  for copper sulphate pentahydrate  $CuSO_4 \cdot 5H_2O$ . We used four polyethylene bottles of 250 ml capacity containing a solution of 1g of NaCl in 250 ml of distilled water each. Then we set the paramagnetic salt concentration by inserting 1, 0.5, 0.25 and 0 g of paramagnetic salt as it is described in Table 5.

Phantom n°	NaCl (g)	$CuSO_4 \cdot 5H_2O$ (g)	$H_2O$ (ml)
1	1	1.00	250
2	1	0.50	250
3	1	0.25	250
4	1	0.00	250

Table 5: Characteristics of the phantoms used for preliminary analysis.



Fig. 54: Water phantoms with paramagnetic agent  $CuSO_4$ .

Measurements of spin-spin relaxation constants were done by using PRESS sequences with echo times of 50, 100, 150, 200 and 350 ms. Estimations of the  $T_2$  decay constant were obtained with three different methods:

- Linear regression between the echo times used and the logarithm of amplitude values given by AMARES of the jMRui package.
- Linear regression between the echo times used and the logarithm of the amplitude estimated with a homemade software based on the same functions of the one described in section 2.3 but designed for water.
- Linear regression between the echo times used and the logarithm of the maximum value of the water peak.

All these approaches are theoretically correct, since the water hydrogens are magnetically equivalent and their spectrum is described as follows:

$$S(\omega) = S_0 \frac{[-i(\omega - \omega_0) + \frac{1}{T_2^*}]}{(\omega - \omega_0)^2 + \left(\frac{1}{T_2^*}\right)^2}; \text{ with } S_0 \propto e^{-\frac{TE}{T_2}} \implies \ln(S_0(TE)) \propto -1/T_2$$

( 39 )

Results of these estimations are showed in section 3.1.1.

---

## 2.4.2 PHANTOMS WITH METABOLITES

### **First Trial: Metabolites with paramagnetic agents**

To correctly simulate the relaxation of water in the peripheral zone of the prostate, which is about 100 ms for cancerous tissue and 140 ms for healthy prostate (40), five different test phantoms were manufactured with  $\text{CuSO}_4$  and different concentrations of citrate, choline and creatine. Concentrations of metabolites were chosen to be in the order of magnitude of in vivo ones. We used choline chloride as a choline source, sodium citrate dihydrate as a citrate source and creatine monohydrate as a creatine source, all the substances were purchased from Sigma-Aldrich. As it is shown from results in section 3.1.1, 0.5g/250ml of  $\text{CuSO}_4 \cdot 5\text{H}_2\text{O}$  brings the  $T_2$  of water to approximately 140 ms, which is compatible with the relaxation time in the peripheral zone of the prostate (for water).

Metabolites were put in a 250 ml solution of distilled water with 0.5 g of  $\text{CuSO}_4 \cdot 5\text{H}_2\text{O}$  with the molarities shown in Table 6; pH was adjusted to 7.0, the mean physiological value for prostatic tissue (17).

Phantom n°	Cit (mM)	dCit (mM)	Cho (mM)	dCho (mM)	Cr (mM)	dCr (mM)
1	0.005	0.00008	0.0200	0.0002	0.0150	0.0002
2	0.0150	0.0001	0.0150	0.0002	0.0125	0.0002
3	0.0250	0.0002	0.0100	0.0002	0.0100	0.0002
4	0.0400	0.0003	0.0075	0.0002	0.0075	0.0001
5	0.0600	0.0005	0.0050	0.0001	0.0050	0.0001

Table 6: Concentrations of metabolites in homemade phantoms with paramagnetic agent.

The blue color of the solutions was deeper than color of the phantoms made with the same concentration of copper salt but without metabolites (as can be seen comparing Fig. 55 to Fig. 54). Moreover in the MR spectrum of phantom 5, the one with the greatest concentration of citrate, the peaks of the methylene protons of citrate are heavily suppressed, as can be seen from Fig. 56. Spectrum of citrate from this phantoms is not similar or at least comparable to the ones found by García-Martín et al (41) for phantoms with the same concentrations of choline, creatine and citrate but without paramagnetic salt. Although we did not see any precipitate, this phenomenon can indicate a possible interaction between citrate and  $\text{Cu}^{++}$  ions, to form temporary complexes of copper-citrate. Methylene protons, by staying closer to copper ions, perceive a stronger dephasing local field for a longer time compared to choline and creatine. Consequently, their spectrum is suppressed due to fast dephasing. Since further investigations of this excess of relaxation were not among the purposes of this work, we removed the paramagnetic salt from our recipes and we manufactured again the phantoms to test the accuracy of quantifications. By the way, this experience had to be mentioned since copper sulphate is commonly used as a relaxation agent for MRS test phantoms but it showed to be not suitable for the realization of phantoms containing citrate.

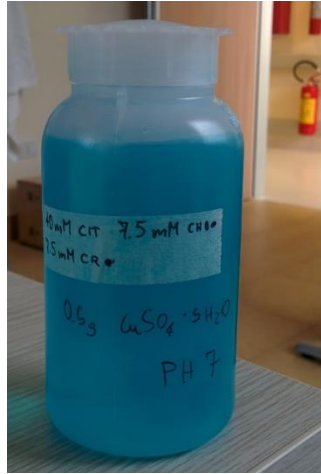


Fig. 55: Deep blue color of a metabolite phantom with  $\text{CuSO}_4$ .

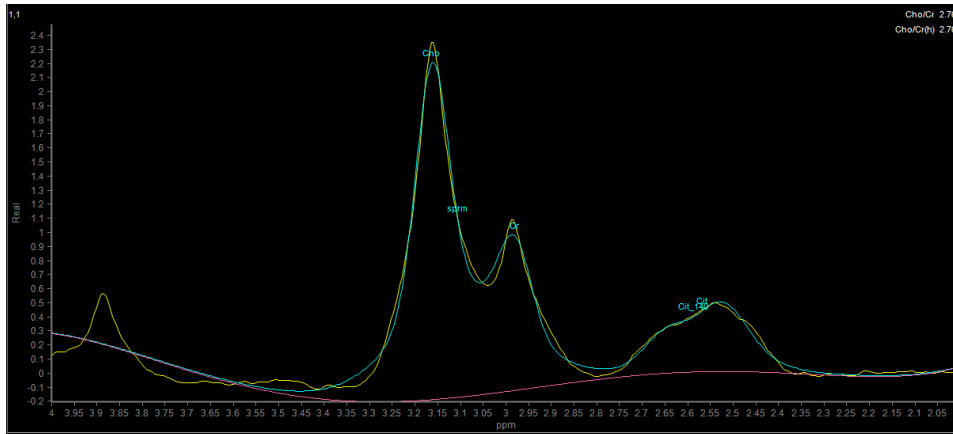


Fig. 56: Destructive effect of  $\text{CuSO}_4$  to the spectrum of citrate in a phantom with 5 mM creatine, 5 mM choline and 60 mM of citrate. Four peaks should have been observed around 2.5 ppm. Spectrum acquired using a PRESS sequence with 110 ms echo time.

## Phantoms with metabolites without paramagnetic agents

To avoid excessive relaxation of citrate we made new phantoms following the recipe provided by García-Martín et al (41) (except for zinc ions). Concentrations of the metabolites inside the phantoms are showed in Table 7. We used choline chloride as a choline source, sodium citrate dihydrate as a citrate source and creatine monohydrate as a creatine source, all the substances were purchased from Sigma-Aldrich. All the polyethylene bottles were filled with 250 ml of distilled water and contained 155 mM of NaCl each, to set an appropriate conductivity to the solutions. Values of pH were set to be physiological (pH=7) except for phantom n°6 which was at pH=5 to see possible changes of j-coupling constants and chemical shifts in the spectrum of citrate. Values of

pH were adjusted using diluted solutions of NaOH and HCl and were measured with the pH meter of the biological laboratories of the IRST research institute (Fig. 57).

Phantom n°	Cit (mM)	dCit (mM)	Cho (mM)	dCho (mM)	Cr (mM)	dCr (mM)	pH	dpH
1	0.005	0.00008	0.0200	0.0002	0.0150	0.0002	7.00	0.05
2	0.0150	0.0001	0.0150	0.0002	0.0125	0.0002	7.00	0.05
3	0.0250	0.0002	0.0100	0.0002	0.0100	0.0002	7.00	0.05
4	0.0400	0.0003	0.0075	0.0002	0.0075	0.0001	7.00	0.05
5	0.0600	0.0005	0.0050	0.0001	0.0050	0.0001	7.00	0.05
6	0.0600	0	0	0	0	0	5.00	0.05

Table 7: Concentrations of metabolites and pH values for the homemade test phantoms.



Fig. 57: Adjusting the pH of the homemade phantoms.

## 2.5 SEQUENCES USED

### 2.5.1 SEQUENCES USED FOR PHANTOM QUANTIFICATIONS

Homemade phantoms were acquired with the MR scanner using the head-coil showed in Fig. 32. Resolution parameters for sequences were chosen to be similar to the parameters used for in vivo acquisitions. In this sequences optimization of the exam time is an important feature, thus low resolutions (1024 points instead of 2048) and short repetition times were used despite the low quality of the spectra. STEAM sequences with the shortest possible echo time were used to obtain chemical shift and j-coupling parameters of citrate, while a PRESS sequence with a commonly used TE of 140 ms, with a repetition time of 1500 ms, was used to quantify metabolite concentrations in phantoms. To compute correct values of the ratio (Cho+Cr)/Cit, spectral corrections have to be done to compensate for different spin-spin relaxation times of the metabolites. Long TE values have to be used to measure correctly the  $T_2$  since there are no paramagnetic agents in the solution. To achieve echo times of 1, 1.5 seconds, unrealistic values for clinical practice, repetition times of 3 seconds were used. To make all the measurements comparable, we turned off the optimization of the receiver, which sets automatically a gain to the signal to optimize quantum efficiency, and set the attenuation coefficient for the receiver ( $1/\text{gain}$ ) to 8 dB for each acquisition.

### STEAM

A STEAM sequence was used to acquire Cit spectrum at very short echo time. Short echo times allow to see Cit spectrum almost in full absorption mode, since j-coupling evolution has few time to take place. Unfortunately this type of sequence is not very suitable for in vivo acquisition due to the poor SNR of typical prostate spectra. For phantom acquisitions a voxel of  $2 \times 2 \times 2.5 \text{ cm}^3$  was positioned in the center of the polyethylene bottle, as it is showed in Fig. 58.

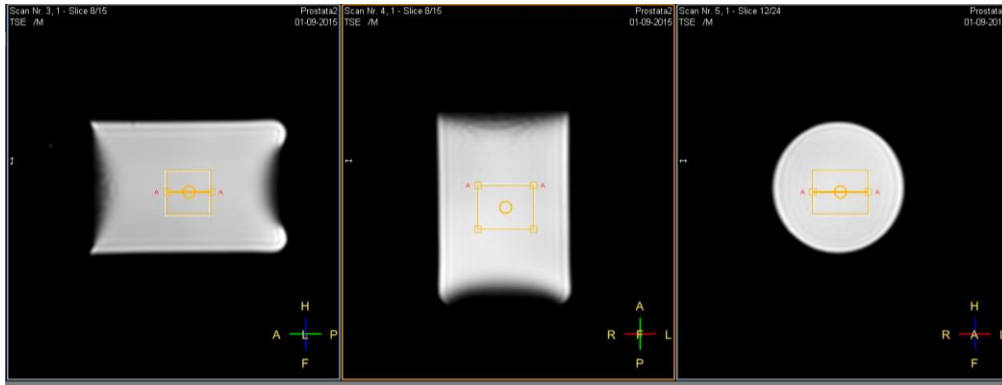


Fig. 58: Voxel placement in the homemade phantom.

Some important parameters of the STEAM sequence used are listed below:

- Iterative shimming
- TR=1500 ms (the repetition time of the sequence)
- TE=8.6 ms
- Mixing time=minimum
- Water suppression: CHES with 160 Hz of bandwidth
- SAR mode: high
- PNS mode: high
- Basing pulse: No
- Spectral bandwidth=2000 Hz
- Samples=1024
- NSA=192
- Gradient spoiling: yes
- N° phase cycles= 16
- Receiver optimization: OFF
- Receiver attenuation =8 dB
- Voxel size:  $2 \times 2 \times 2.5 \text{ cm}^3$

## PRESS

PRESS sequences were used to acquire spectra from phantoms with different concentration of metabolites, to measure their spin-spin relaxation times and their quantity. Since we did not use paramagnetic agents, we had to use long TR sequences (TR=3000) to achieve longer echo times for  $T_2$  measurements.

General features of the PRESS sequence:

- Iterative shimming
- TR=3000 ms
- TE=140, 400, 600, 800, 1000, 1200, 1500 ms
- Water suppression: CHESS with 160 Hz of bandwidth
- SAR mode: high
- PNS mode: high
- Basing pulse: water suppression
- Spectral bandwidth=2000 Hz
- Samples=1024
- NSA=192
- Gradient spoiling: yes
- Receiver optimization: OFF
- Receiver attenuation =8 dB
- Voxel size:  $2 \times 2 \times 2.5 \text{ cm}^3$

For phantom quantification a similar PRESS sequence with TE=140 ms and TR=1500 ms was used.

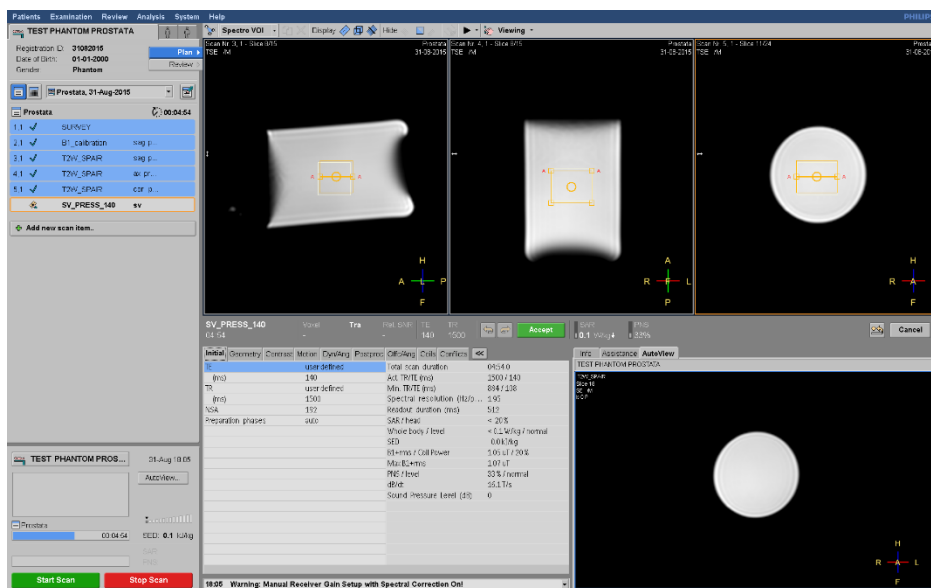


Fig. 59: Screenshot of the user interface at the scanner console. PRESS sequence for quantification was planned by considering commonly used parameters for in vivo acquisitions.



---

## 2.5.2 SEQUENCES USED FOR IN VIVO ACQUISITIONS

To test the fitting ability of the homemade software we acquired spectra from prostates of two middle-aged male subjects with different sequences based on PRESS, without using any endorectal coil. The volunteers could not be prepared as patients, so anticholinergics were not administered to diminish rectum movements. Since we wanted only to test the ability of the software to correctly fit the spectra we did not turn the receiver optimization off. Number of averaged signals was reduced from 192 to 32 to achieve a shorter exam time, while SAR and PNS modes were set to “low”. Healthy volunteers were selected not only to test MRS sequences but also to try other features of the new scanner Philips Ingenia 3T, so in that occasion there was not time to make measurements of the spin-spin relaxation time for in vivo metabolites. Spectra from two healthy volunteers were acquired, from subject 1 we took a single voxel and a MRSI acquisition with 1024 points in resolution, from subject 2 we took only a MRSI acquisition but with 2048 points in resolution. We used an echo time of 140 ms, suggested by Philips to see peaks of citrate approximately in-phase.

Single-voxel PRESS general parameters:

- Iterative shimming
- TR=1500 ms
- TE=140 ms
- Water suppression: CHESS with 160 Hz of bandwidth
- SAR mode: low
- PNS mode: low
- Basing pulse: water suppression
- Spectral bandwidth=2000 Hz
- Samples=1024
- NSA=32
- Gradient spoiling: yes
- N° phase cycles= 16
- Receiver optimization: ON
- Voxel size:  $1.5 \times 1.5 \times 1.5 \text{ cm}^3$

### 3D PRESS for MRSI

3D PRESS is a multi-voxel sequence used for magnetic resonance spectroscopy imaging. It is based on PRESS and repeats the sequence in a set of adjacent voxels to make a 3D map of spectra. We acquired, for the two healthy volunteers, five slices of 1.2 cm of thickness; in each slice there was a matrix of  $9 \times 7$  voxel of  $1 \times 1 \times 1.2 \text{ cm}^3$  of volume (for a total of 315 spectra). We used essentially the same parameters of the single-voxel sequence but for subject 2 we brought the resolution to 2048 points. An example of the geometry used for acquisition is showed in Fig. 60.

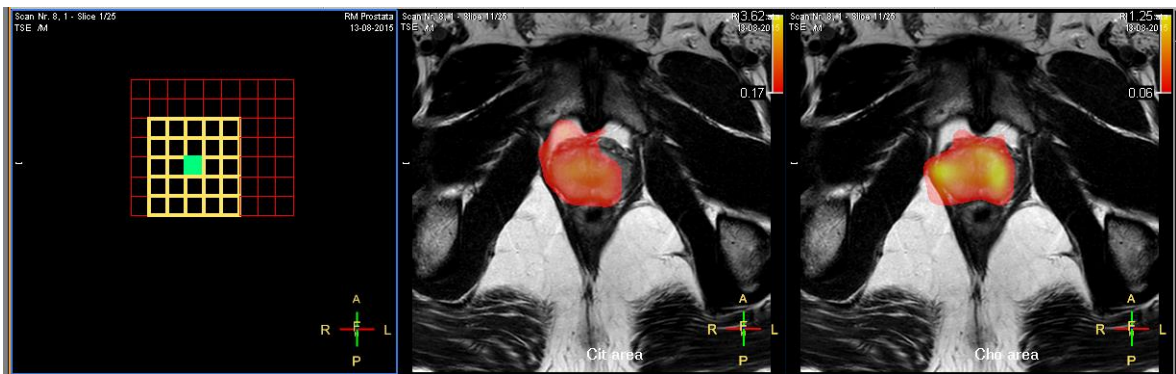


Fig. 60: Prostate MRSI acquisition of a healthy volunteer.

## 3 RESULTS

### 3.1 IN VITRO TESTS ON HOMEMADE PHANTOMS

#### 3.1.1 MEASURE OF THE $T_2$ OF WATER WITH PARAMAGNETIC AGENT $CuSO_4$

With reference to Eq. ( 39 ), the logarithm of the amplitude estimated by AMARES, the logarithm of the maximum value of the water peak and the logarithm of the amplitude estimated with the homemade software (SimWater) were compared with echo times used for the acquisitions for phantoms containing different quantities of  $CuSO_4 \cdot 5H_2O$ . For brevity only the parameters estimated through linear regression are shown from Table 8 to Table 11. Spectra were acquired using PRESS sequences with TE of 50, 100, 150, 200 and 350 ms, TR of 1500 ms and 1024 points in resolution. In the following tables “a” is the slope of the linear regression, “da” its uncertainty, “b” is the intercept, “db” the uncertainty of the intercept, “dy” is the error that can be assigned to the variables after the regression,  $T_2$  and  $dT_2$  are the estimated relaxation time and its uncertainty respectively and  $R^2$  is the Pearson’s correlation coefficient relative to the regression.

0g $CuSO_4$	a	b	da	db	dy	$T_2$ (ms)	$dT_2$ (ms)	$R^2$
AMARES	-0.0005	-1.9	0.0006	0.1	0.1	2000	2000	0.1796
Max. Peak	-0.0013	2.882	0.00012	0.013	0.03	790	80	0.9728
SimWater	-0.0008	-2.489	0.00013	0.013	0.03	1300	200	0.9282

Table 8: Estimated  $T_2$  for phantom containing 0g of  $CuSO_4 \cdot 5H_2O$ , using three different methods of quantification.

0.25 g $CuSO_4$	a	b	da	db	dy	$T_2$ (ms)	$dT_2$ (ms)	$R^2$
AMARES	-0.003	-0.78	0.0003	0.03	0.07	340	30	0.9727
Max. Peak	-0.0031	3.6	0.00006	0.006	0.01	320	6	0.9988
SimWater	-0.0033	-1.39	0.00004	0.004	0.01	305	4	0.9996

Table 9: Estimated  $T_2$  for phantom containing 0.25g of  $CuSO_4 \cdot 5H_2O$ , using three different methods of quantification.

0.5 g $CuSO_4$	a	b	da	db	dy	$T_2$ (ms)	$dT_2$ (ms)	$R^2$
AMARES	-0.0072	-0.7	0.0008	0.1	0.2	140	20	0.9612
Max. Peak	-0.0071	3.501	0.00004	0.005	0.01	141	1	0.9999
SimWater	-0.0071	-1.335	0.00004	0.004	0.01	140	1	0.9999

Table 10: Estimated  $T_2$  for phantom containing 0.5g of  $CuSO_4 \cdot 5H_2O$ , using three different methods of quantification.

1 g CuSO <sub>4</sub>	a	b	da	db	dy	T <sub>2</sub> (ms)	dT <sub>2</sub> (ms)	R <sup>2</sup>
AMARES	-0.0127	-0.71	0.00012	0.012	0.03	79	1	0.9997
Max. Peak	-0.0129	3.223	0.00002	0.002	0.004	77.3	0.1	1
SimWater	-0.0129	-1.354	0.00004	0.004	0.01	77.8	0.2	1

Table 11: Estimated T<sub>2</sub> for phantom containing 1g of CuSO<sub>4</sub>·5H<sub>2</sub>O, using three different methods of quantification.

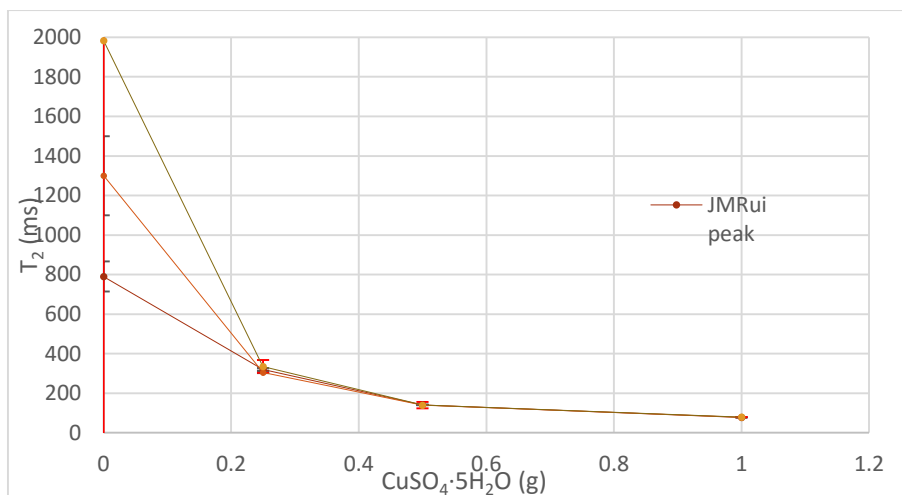


Fig. 61: Estimated T<sub>2</sub> values vs quantity of CuSO<sub>4</sub>·5H<sub>2</sub>O.

From Table 8 we can see lack of precision on the estimation of the T<sub>2</sub> decay parameter of distilled water without paramagnetic agents, this is due to the long relaxation time of pure water at room temperatures. Thus, much longer echo times should be used to perform measurements in pure water. From Pearson's correlation coefficient (the term R<sup>2</sup> in the tables) we see that stronger correlations are found in the estimations of the T<sub>2</sub> with the maximum value of peak (Max. Peak) and with the amplitude of the homemade software (SimWater) compared to results obtained using AMARES.

### 3.1.2 IN VITRO ESTIMATION OF CITRATE SPECTRAL PARAMETERS

To correctly simulate the Hamiltonian evolution of citrate, we measured the j-coupling constant and the chemical shift of the methylene protons from NMR spectra of the homemade phantoms.

Phantom n°	Cit (mM)	dCit (mM)	Cho (mM)	dCho (mM)	Cr (mM)	dCr (mM)	pH	dpH
5	0.0600	0.0005	0.0050	0.0001	0.0050	0.0001	7.00	0.05
6	0.0600	0	0	0	0	0	5.00	0.05

Table 12: Concentration values of the homemade phantoms used to estimate citrate spectral parameters.

Spectral parameters of citrate were measured at 3T using the formulae developed in section 1.3.4. FIDs were acquired from phantom 5 at pH 7 and from phantom 6 at pH 5 to see possible changes in j-coupling or in chemical shifts, caused by the acidification of the environment. Spectra were obtained using STEAM sequence on a  $2 \times 2 \times 2.5 \text{ cm}^3$  voxel with an echo time of 8.6 ms.

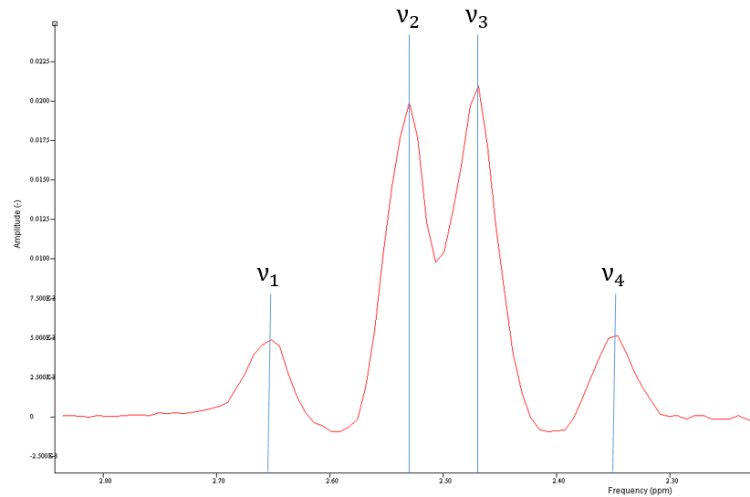


Fig. 62: Real part (absorption mode) of the MR spectrum of citrate at pH 7, using STEAM sequence with  $TE=8.6 \text{ ms}$  in a homemade phantom containing 60 mM of citrate in solution with other metabolites.

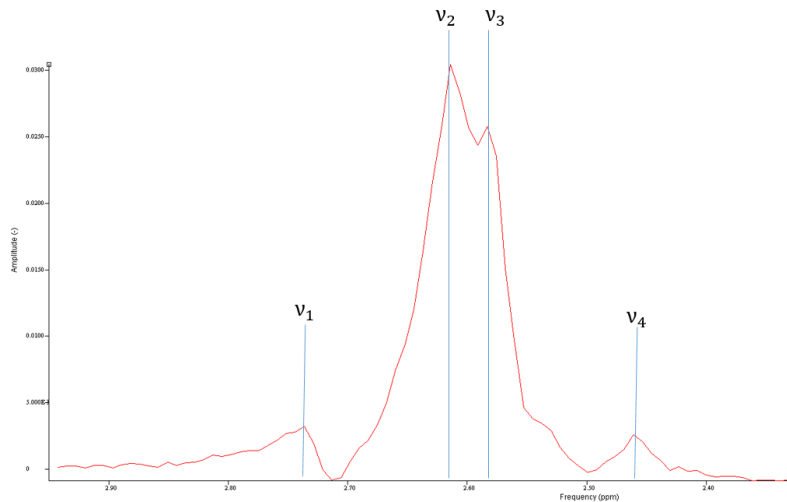


Fig. 63: Real part (absorption mode) of the spectrum of citrate at pH 5, using STEAM sequence with  $TE=8.6 \text{ ms}$  in a homemade phantom containing 60 mM of citrate in solution.

By taking into account Fig. 16, the following equations were used to calculate the parameters and estimate uncertainties:

$$j_{AB} = \frac{(v_1 - v_2) + (v_3 - v_4)}{2} \quad \delta = \frac{v_1 + v_2 + v_3 + v_4}{4} \quad dj_{AB} = d\delta = \frac{\sqrt{4dv^2}}{2} = dv$$

$$\Delta = v_A - v_B = \sqrt{(v_2 - v_3 + j_{AB})^2 - j_{AB}^2}; \quad d\Delta = \frac{(v_2 - v_3) \frac{dv}{\sqrt{2}}}{\sqrt{(v_2 - v_3 + j_{AB})^2 - j_{AB}^2}} + \frac{j_{AB} dj_{AB}}{\sqrt{(v_2 - v_3 + j_{AB})^2 - j_{AB}^2}}$$

( 40 )

Results of estimation are showed below in Table 13:

PH 5	j (Hz)	dj (Hz)	$\Delta$ (ppm)	d $\Delta$ (ppm)	$\delta$ (ppm)	d $\delta$ (ppm)
	16	2.00	0.09	0.07	2.604	0.002
PH 7	j (Hz)	dj (Hz)	$\Delta$ (ppm)	d $\Delta$ (ppm)	$\delta$ (ppm)	d $\delta$ (ppm)
	16	2.00	0.13	0.05	2.501	0.002

Table 13: measured parameters of in vitro citrate at pH=5 and at pH=7;

Values for j-coupling and chemical-shifts in Table 13 are consistent with the expected values but the uncertainties are too great to estimate univocally the parameters needed for simulations. This is due to the fact that a clinical spectrometer cannot reach adequate values of uniformity of the static field to determine these quantities, since the shimming volumes are really big compared to the ones commonly used in structural biology. Anyway also a rough estimate provides a range of values that can be adjusted empirically to fit acquired spectra with simulated ones.

### 3.1.3 MEASURE OF THE T<sub>2</sub> OF METABOLITES IN HOMEMADE PHANTOMS

To correct the parameters used for quantification, T<sub>2</sub> decay constants have to be measured. Estimation of the T<sub>2</sub> decay parameters was done by acquiring phantom n°5 with PRESS sequences, using a TR of 3000 ms and echo times of 140, 400, 600, 600, 1000, 1200 and 1500 ms, from a voxel of 2×2×2.5 cm<sup>3</sup>. Choline and creatine T<sub>2</sub> values were measured through linear regression between the logarithm of the maximum value of choline and creatine peaks. Since sequences based on spin-echo do not refocus the j-coupling evolution, spectrum of citrate changes dramatically varying the echo time. Consequently the only way we had to measure the T<sub>2</sub> correctly was to use amplitude estimation with the homemade quantification software. We used values compatible with the one found in

Table 13 to simulate citrate, and did small adjustments on the echo times used in the virtual sequence of the software to get reasonable values for the K-S test (for example by using a TE of 1510 ms instead of 1500 ms). Text file for citrate simulation is showed in Fig. 64, D-values for K-S test for each echo time are showed in Table 14 and linear regressions are depicted in Fig. 65 and in Fig. 66.

```

SysName (2) : citrate - Name of spin system

NSpins (0) : 2 - Number of spins in spin system

Iso(0) (2) : 1H - Spin Isotope Type
Iso(1) (2) : 1H - Spin Isotope Type

PPM(0) (1) : 2.44 - Shift of spin 0 (PPM)
PPM(1) (1) : 2.56 - Shift of spin 1 (PPM)

J(0,1) (1) : 15 - Scalar coupling (Hz)

Omega (1) : 127.768332 - Spec. Freq. in MHz (1H based)

```

*Fig. 64: Spectral parameters used for simulating citrate for the analysis of the homemade phantoms. Parameters were found empirically within the uncertainties of the ones showed in Table 13, for pH 7, which were measured using STEAM.*

D-Value crit. = 0.062	
TE (ms)	D-values
140	0.008
400	0.024
600	0.043
800	0.044
1000	0.060
1200	0.058
1500	0.033

*Table 14: D-values of K-S test obtained for the fit of the spectra with increasing echo times.*

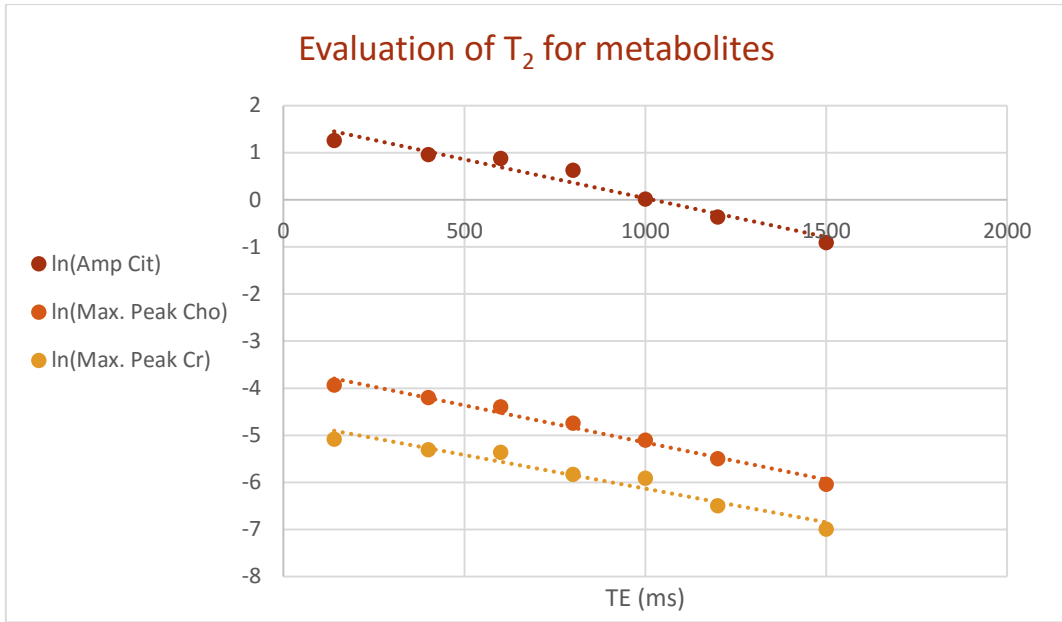


Fig. 65: Linear regression analysis to measure the transverse relaxation times of citrate, choline and creatine inside the homemade phantoms.

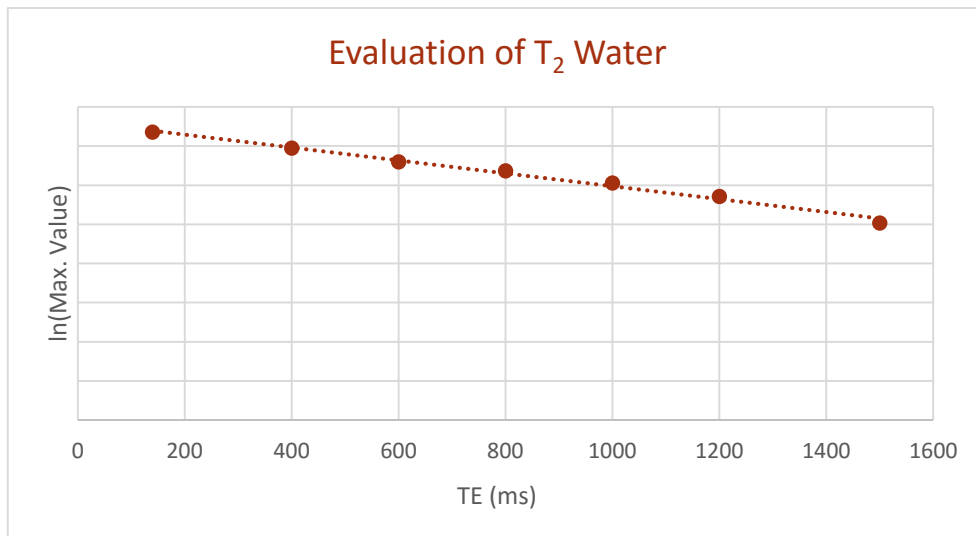


Fig. 66: Also the decay constant of water was measured to make signal corrections.

In Table 15, Table 16, Table 17 and Table 18 quantitative measurements of the relaxation constants are shown. In those tables “a” is the slope of the linear regression, “b” the intercept, “da” and “db” the uncertainties on the parameters, “dy” the estimated uncertainty of the points with the least square method, T<sub>2</sub> and dT<sub>2</sub> are the transverse relaxation time and its uncertainty.



a	b	da	db	dy	Cit T <sub>2</sub> (ms)	dT <sub>2</sub> (ms)
-0.0017	1.68	0.0002	0.07	0.2	610	60
R <sup>2</sup>	0.9566					

Table 15: Least squares parameters, T<sub>2</sub> value and Pearson's correlation coefficient for citrate.

a	b	da	db	dy	Cho T <sub>2</sub> (ms)	dT <sub>2</sub> (ms)
-0.00158	-3.6	0.0001	0.04	0.1	630	40
R <sup>2</sup>	0.9831					

Table 16: Least squares parameters, T<sub>2</sub> value and Pearson's correlation coefficient for choline.

a	b	da	db	dy	Cr T <sub>2</sub> (ms)	dT <sub>2</sub> (ms)
-0.00143	-4.7	0.0001	0.1	0.2	700	70
R <sup>2</sup>	0.9485					

Table 17: Least squares parameters, T<sub>2</sub> value and Pearson's correlation coefficient for creatine.

a	b	da	db	dy	Water T <sub>2</sub> (ms)	dT <sub>2</sub> (ms)
-0.00082	3.81	0.00003	0.02	0.04	1220	50
R <sup>2</sup>	0.9912					

Table 18: Least squares parameters, T<sub>2</sub> value and Pearson's correlation coefficient for water.

From the measured T<sub>2</sub> we can compute the correction factors for transverse relaxation, in particular for TE=140 ms, we obtain:

$$e^{TE/T_2Cit} = 1.26 \pm 0.03$$

$$e^{TE/T_2Cho} = 1.25 \pm 0.02$$

$$e^{TE/T_2Cr} = 1.22 \pm 0.03$$

$$e^{TE/T_2Water} = 1.12 \pm 0.01$$

( 41 )

### 3.1.4 QUANTIFICATION OF METABOLITES IN HOMEMADE PHANTOMS WITH HOMEMADE SOFTWARE

To correctly quantify the metabolites, we acquired spectra from each phantom with and without water suppression to compensate for different locations of voxel that might cause signal fluctuations. Acquisitions were performed using PRESS sequences with TE=140 ms and 1024 points in resolution in a voxel of 2×2×2.5 cm<sup>3</sup>. Spectra were analyzed with the homemade software from ppm 1.9 to ppm 3.6 for metabolites and from ppm 3 to ppm 7 for water. Simulation parameters used for metabolites are described in Fig. 67, Fig. 68

and Fig. 69. Parameters for simulating citrate were empirically chosen within the values previously measured from spectra.

```

SysName (2) : citrate - Name of spin system
NSpins (0) : 2 - Number of spins in spin system
Iso(0) (2) : 1H - Spin Isotope Type
Iso(1) (2) : 1H - Spin Isotope Type
PPM(0) (1) : 2.44 - Shift of spin 0 (PPM)
PPM(1) (1) : 2.56 - Shift of spin 1 (PPM)
J(0,1) (1) : 15 - Scalar coupling (Hz)
Omega (1) : 127.768332 - Spec. Freq. in MHz (1H based)

```

Fig. 67: Simulation parameters of citrate methylene protons, used for in vitro acquisitions.

```

SysName (2) : Choline - Name of the Spin System
NSpins (0) : 1 - Number of Spins in the System
Iso(0) (2) : 1H - Spin Isotope Type
Omega (1) : 127.768332 - Spec. Freq. in MHz (1H based)
PPM(0) (1) : 3.12 - Shift of spin 0 (PPM)

```

Fig. 68: Simulation parameters of choline methyl proton, used for in vitro acquisitions.

```

SysName (2) : Creatine - Name of the Spin System
NSpins (0) : 1 - Number of Spins in the System
Iso(0) (2) : 1H - Spin Isotope Type
Omega (1) : 127.768332 - Spec. Freq. in MHz (1H based)
PPM(0) (1) : 2.950 - Shift of spin 0 (PPM)

```

Fig. 69: Simulation parameters of creatine methyl proton, used for in vitro acquisitions.

The screenshot displays the 'GhostBuster Prostate' software interface. On the left, there are four selection panels: 'Select real part' (listing files like misura T2/previsioni/Re15ciPRESS.t), 'Select imaginary part' (listing files like invivo/ misura T2/previsioni/Im5ciPRESS.t), 'Select frequency file' (listing files like freq1024.txt), and 'Select interval from point A to point B for quantification' (with input fields for Point A (ppm) at 1.9 and Point B (ppm) at 3.6). Below these are input fields for Echo Time (ms) at 140, Bandwidth (Hz) at 2000, and Resolution (pts) at 1024, along with a 'Start quantification' button. On the right, the results of the quantification are displayed in a text box:

```

Amplitude Citrate: 1.15816 +- 0.00579082
Amplitude Choline: 0.466458 +- 0.00233229
Amplitude Creatine: 0.584646 +- 0.00292323
T2* Citrate(ms): 46.9373 +- 0.156458
T2* Choline(ms): 52.4931 +- 0.174977
T2* Creatine(ms): 57.0803 +- 0.190268
integral Citrate= 0.145522
integral Choline= 0.0514296
integral Creatine= 0.0652462
K-S Test Output: 0.0205115 critical region around x(ppm): 3.19388
Test was done with 294 points in the interval using spline interpolation.
Critical value for 20% accord: 0.0624037

```

Fig. 70: User interface of the homemade software used for quantifications (left). Results of the quantification are stored in Results.txt file (right).

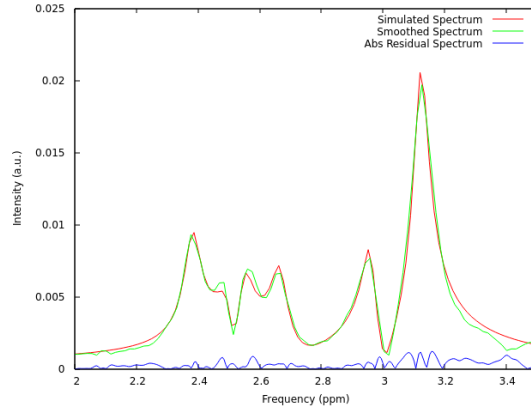


Fig. 71: Example of the graphical output of the homemade software, analysis of the spectrum of a phantom containing 25 mM of citrate, 10 mM of creatine and 10 mM of choline.

D-Value crit.	0.055	D-Value crit.	0.054
Phantom n°	D-Value Metabolites	Phantom n°	D-Value Water
1	0.029	1	0.034
2	0.046	2	0.031
3	0.028	3	0.029
4	0.021	4	0.027
5	0.014	5	0.032

Table 19: D-values of the K-S test used to assess the goodness of fit. All the D-Values are below the critical one for 20% probability that differences between distributions might have been produced by chance.

Fit of the acquired spectra was done successfully, as can be seen from the D-values estimated for all the phantoms showed in Table 19. Integral of the metabolites and their amplitudes were taken into account to search a correlation with real concentrations in phantoms. Before doing linear regression, integrals and amplitudes were corrected for transverse relaxation and signal fluctuations in the following way:

$$\text{Corrected Signal of } i\text{-th metabolite: } A_i = \frac{\frac{S_i}{N_i} * e^{\frac{TE}{T_2^i}}}{\frac{S_{Water}}{2} * e^{\frac{TE}{T_2^{Water}}}}$$

Where  $S_i$  is the signal (in terms of amplitudes or integrals) of the metabolite,  $T_2^i$  its relaxation time,  $N_i$  the multiplicity of the simulated chemical group (multiplicity correction is made inside the program), TE is the echo time used,  $S_{Water}$  is the signal of

water (in terms of amplitudes or integrals) and  $T_2^{Water}$  its relaxation time. Corrected values for amplitudes and integrals measured can be found below in Table 20. Uncertainties for the corrected amplitudes are only lower bounds of the real uncertainties, since they depend only on errors on the evaluation of the  $T_2$  decay constants.

Amp Cit	dAmp Cit	Amp Cho	dAmp Cho	Amp Cr	dAmp Cr
0.000186	0.000004	0.00064	0.00001	0.00067	0.00002
0.00045	0.00001	0.000457	0.000008	0.00046	0.00001
0.00075	0.00002	0.000297	0.000005	0.00034	0.00001
0.00117	0.00003	0.000230	0.000004	0.000289	0.000007
0.00172	0.00004	0.000165	0.000003	0.000233	0.000006

Table 20: Corrected amplitudes for the three metabolites inside test phantoms.

And here are the Plots relative to linear regressions:

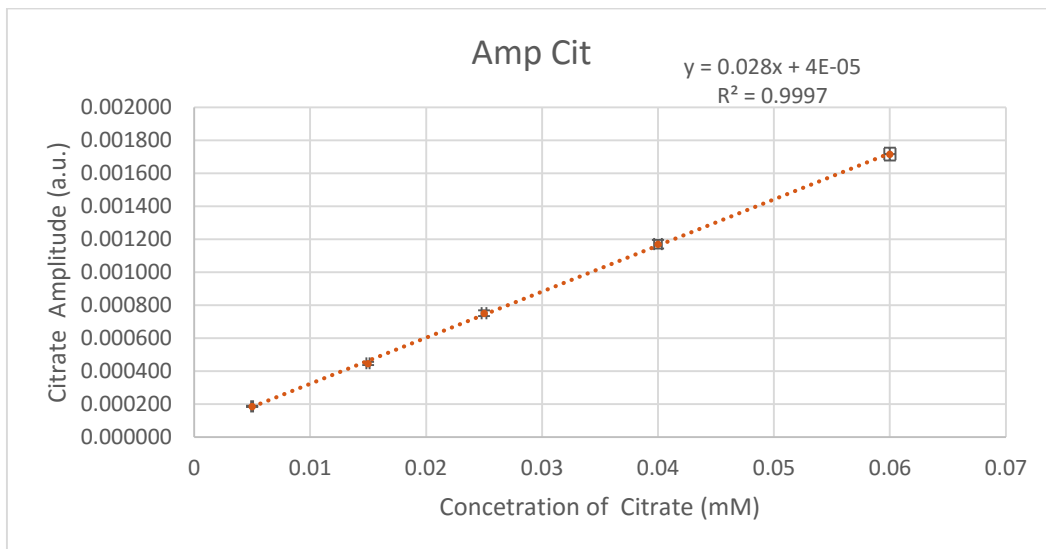


Fig. 72: Linear regression between estimated amplitudes of citrate and its real concentration inside phantoms.

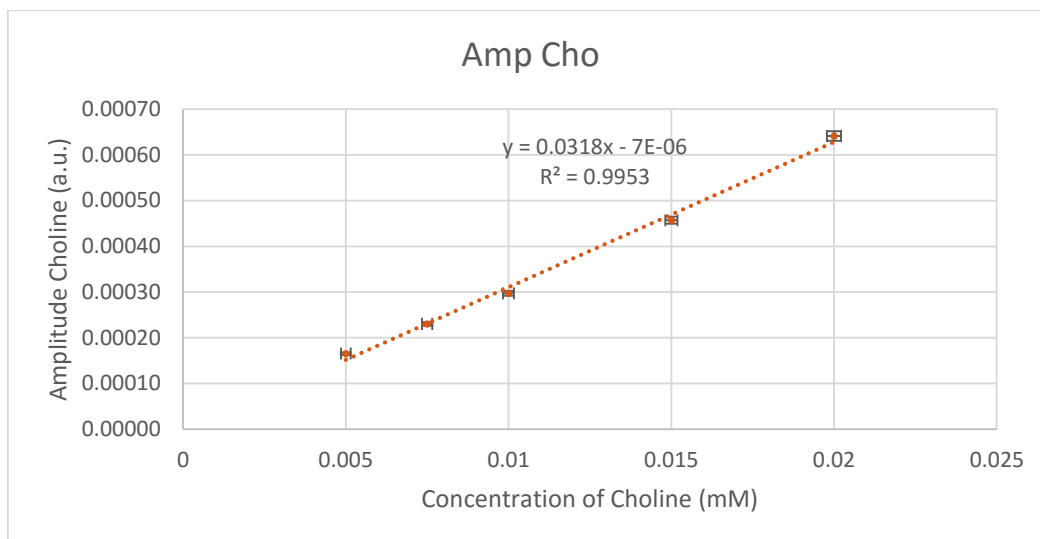


Fig. 73: Linear regression between estimated amplitudes of choline and its real concentration inside phantoms.

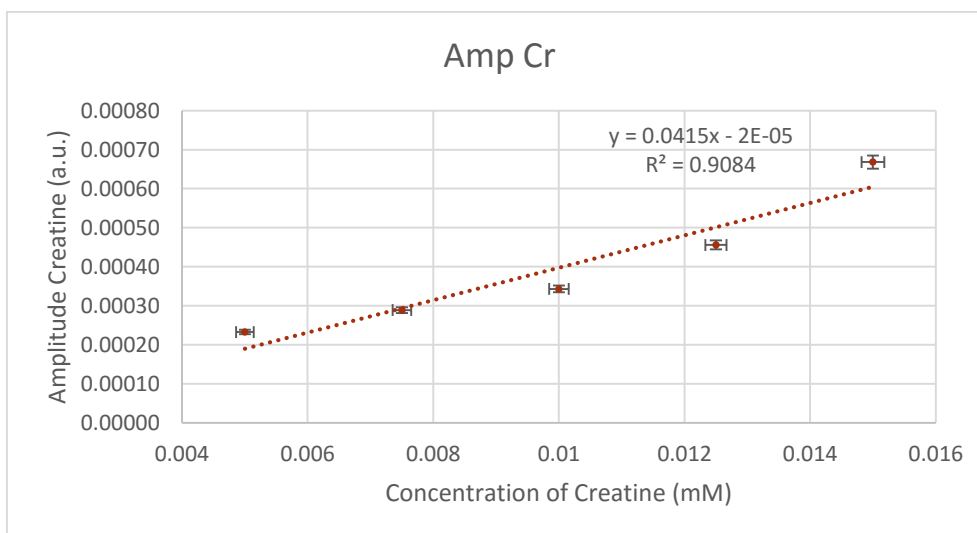


Fig. 74: Linear regression between estimated amplitudes of creatine and its real concentration inside phantoms.

Corrected values for the amplitudes of citrate and choline show a strong correlation with their respective molar concentration in the phantoms. Linear regression for creatine provides a weak correlation, probably because of its weak signal and small variations in its molarity inside the phantoms. For example, citrate is varying between 60 mM and 5 mM while creatine only between 5 mM and 15 mM, moreover signal of the methyl peak of creatine is produced by 3 magnetically equivalent protons while signals of citrate and choline are produced by 4 and 9 protons respectively. Quantity of creatine inside

phantoms was chosen to emulate physiological values in human prostate, following the recipe provided by García-Martín et al (41).

As we did for amplitudes, we corrected the integral values of metabolites for transverse relaxation and signal fluctuations, then we computed linear regressions between them and the real molarities of the metabolites in the phantoms (Table 21). As for amplitudes, errors on the integrals are lower bounds, since we have still to determine an accurate estimate for the uncertainty related to the fitting algorithm used (maybe based on the K-S test or the residual spectrum). Error analysis in metabolomics with NMR is still an open discussion (42) (43), the software used is a first prototype and several measurements are still needed to determine the real uncertainties of the estimated quantities.

Integral cit	dintegral Cit	Integral Cho	dIntegral Cho	Integral Cr	dIntegral Cr
0.00018	0.00000	0.00063	0.000011	0.000687	0.000017
0.00052	0.00001	0.00045	0.000008	0.000469	0.000012
0.00085	0.00002	0.00030	0.000005	0.000348	0.000009
0.00132	0.00003	0.00023	0.000004	0.000290	0.000007
0.00195	0.00004	0.00016	0.000003	0.000225	0.000006

Table 21: Corrected integral values of signal for the three metabolites inside test phantoms.

The plots relative to linear regression analysis between integral values and the molar concentration of the metabolites can be found below:

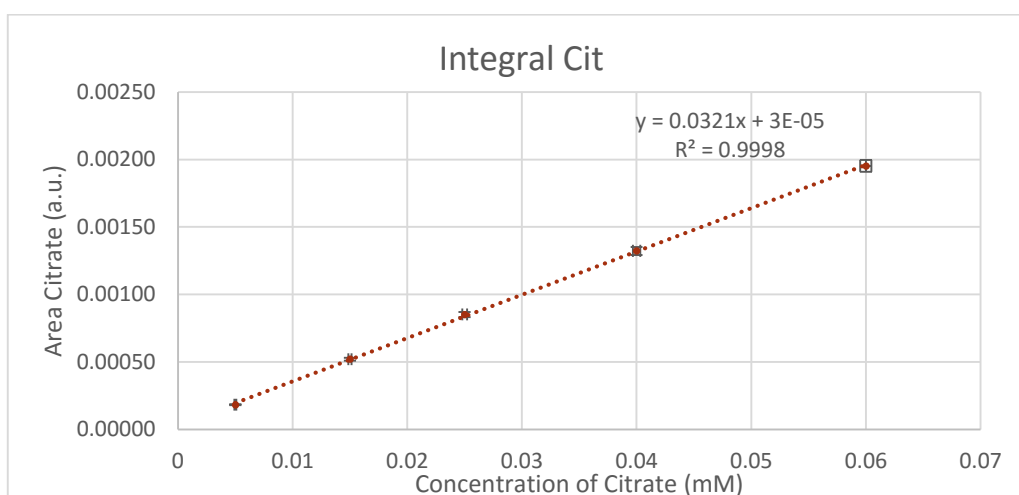


Fig. 75: Linear regression between estimated total signal (integral) of citrate and its real concentration inside phantoms.

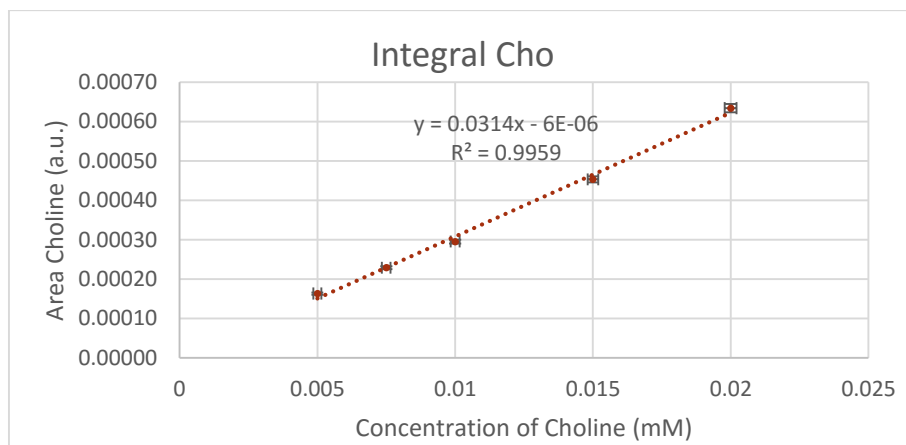


Fig. 76: Linear regression between estimated total signal (integral) of choline and its real concentration inside phantoms.

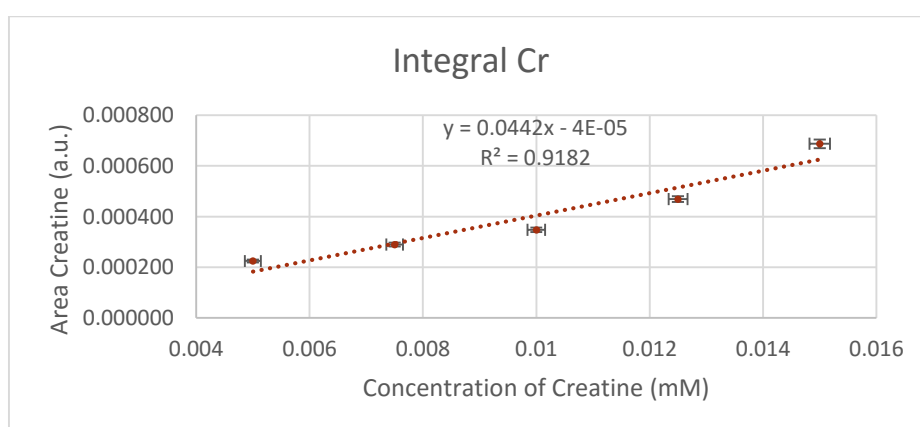


Fig. 77: Linear regression between estimated total signal (integral) of creatine and its real concentration inside phantoms.

Strong correlation between the estimated total signal and the real molarities was found for citrate and choline. Creatine quantification shows a Pearson's correlation coefficient lower than the other two metabolites, probably due to the small range of concentrations tested. Finally we computed the (Cho+Cr)/Cit ratio, which is the quantity of clinical relevance for MRS applied to PCa:

Amp (Cho+Cr)/Cit		Conc. (Cho+Cr)/Cit		Integral (Cho+Cr)/Cit	
value	dvalue	value	dvalue	value	dvalue
7.0	0.2	7.0	0.1	7.2	0.2
2.04	0.05	1.83	0.02	1.77	0.05
0.85	0.03	0.80	0.01	0.76	0.03
0.44	0.03	0.375	0.006	0.39	0.03
0.23	0.03	0.167	0.004	0.20	0.03

Table 22: (Cho+Cr)/Cit values computed with the real molarities, estimated amplitudes and total signal of metabolites.

The ratios evaluated with the estimated quantities are in agreement with the ratio estimated by known molar concentrations, considering also that uncertainties on the amplitudes and integral ratio are only lower bounds of the real ones. Linear regression analysis was also performed to confirm the agreement of these quantities, a plot of the regression is showed in Fig. 78, while the regression parameters for least squares and weighted least squares method are showed in Table 23 and Table 24. In those tables “a” is the slope of the linear regression, “b” the intercept, “da” and “db” the uncertainties on the parameters and “dy” is the estimated uncertainty of the points with the least square method (or the weighted one).

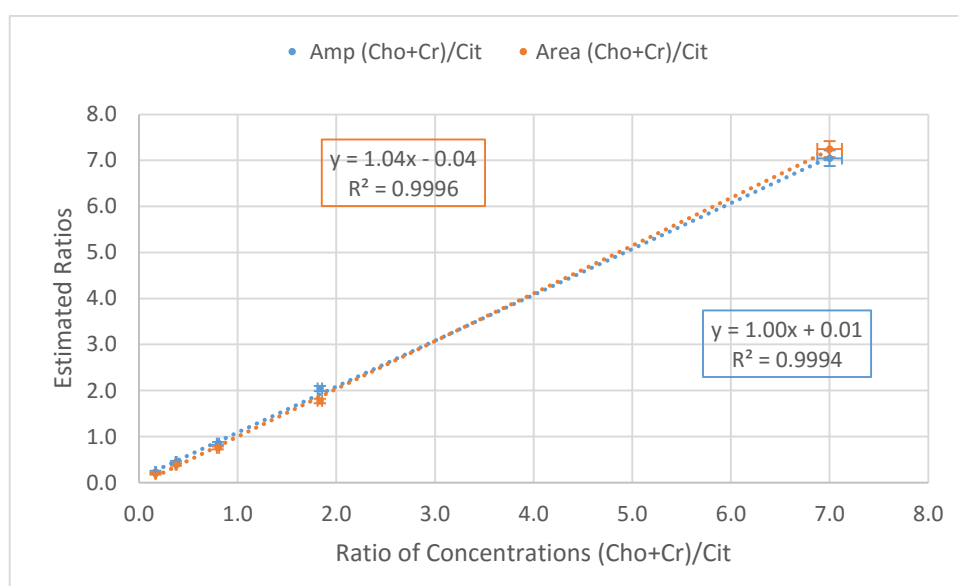


Fig. 78:  $(Cho+Cr)/Cit$  ratios estimated with amplitudes and total signal of fitted spectra compared to the ratio estimated with known molar concentrations of the metabolites.

Integral $(Cho+Cr)/Cit$		least squares parameters			weighted least squares parameters				
a	b	da	db	dy	a	b	da	db	dy
1.04	-0.04	0.01	0.04	0.07	1.02	0.06	0.02	0.02	0.01

Table 23: Least squares parameters and weighted least squares parameters of the linear regression analysis between  $(Cho+Cr)/Cit$  ratios estimated with integral values and real molar concentrations of metabolites.

Amp $(Cho+Cr)/Cit$		least squares parameters			weighted least squares parameters				
a	b	da	db	dy	a	b	da	db	dy
1.00	0.10	0.01	0.04	0.08	0.99	0.01	0.02	0.02	0.1

Table 24: Least squares parameters and weighted least squares parameters of the linear regression analysis between  $(Cho+Cr)/Cit$  ratios estimated with amplitude values and real molar concentrations of metabolites.



### 3.1.5 QUANTIFICATION OF METABOLITES IN HOMEMADE PHANTOMS WITH AMARES

To make a comparison we repeated the quantification with AMARES algorithm of the jMRui software package. Prior knowledge was inserted by pick-picking (selection of the top of the peaks and their FWHM). This approach is quite ill-posed for multiplets like citrate, so, we tried to overcome this problem by using four independent Lorentzian peaks to fit it (see Fig. 79 and Fig. 80). Since for the same echo time relative amplitudes of citrate's peaks should not vary, we took as reference the amplitude of a single peak, in particular peak 5, the one which seems to have the greatest signal. For creatine the methyl resonance of peak 3 was taken as reference instead.

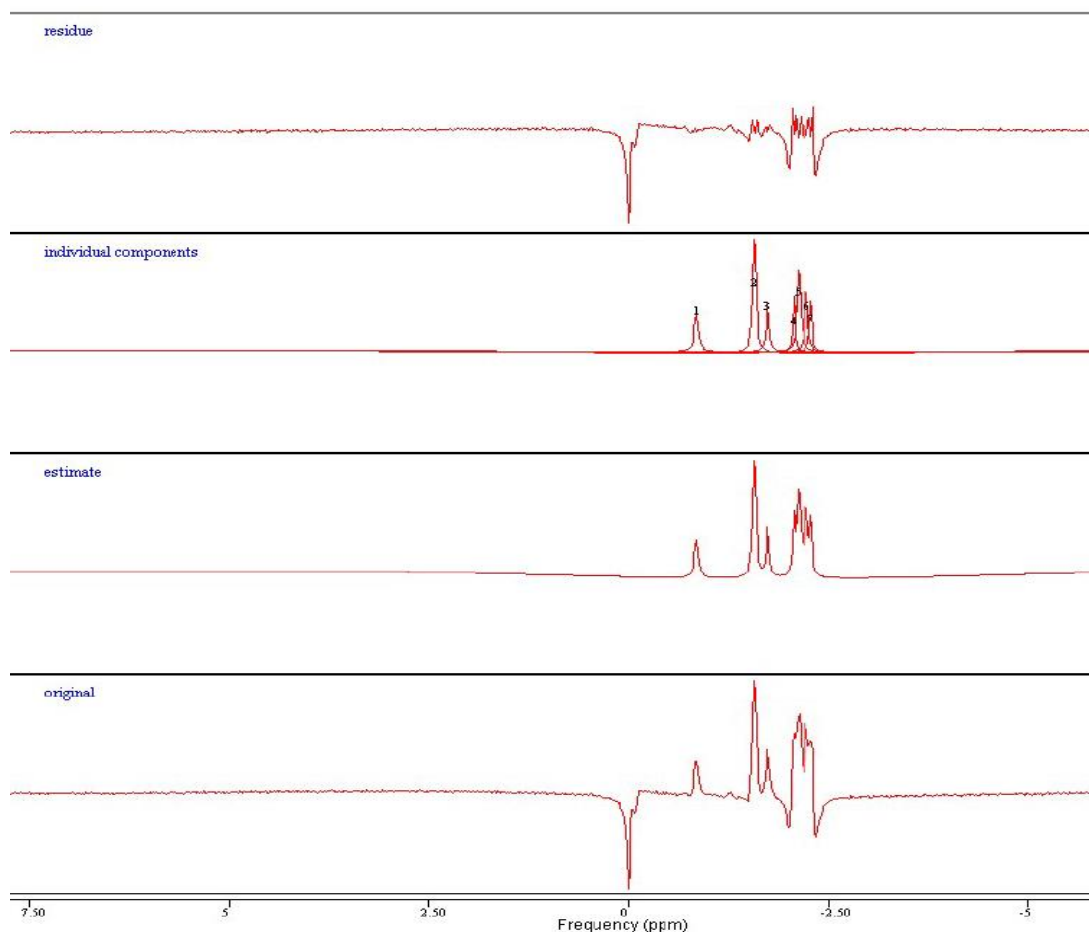


Fig. 79: Example of a quantification with AMARES. Single peaks are fitted quite correctly by Lorentzian functions; citrate, which has not a Lorentzian line-shape, is fitted by a combination of Lorentzian functions instead.

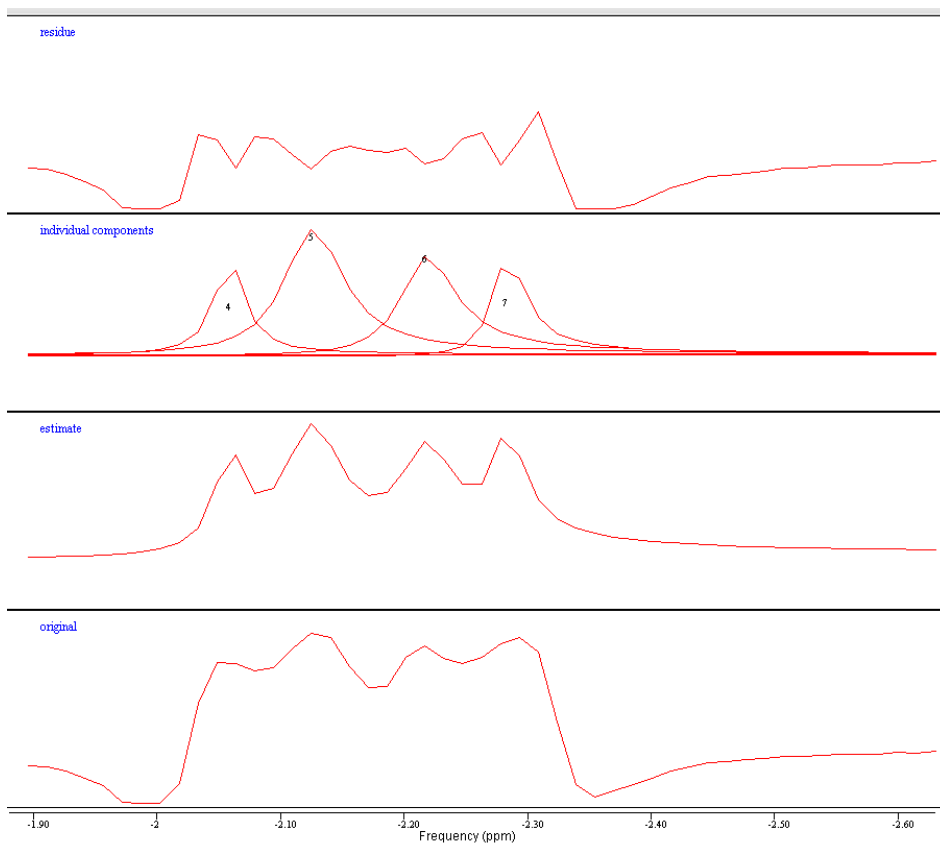


Fig. 80: Amplitude for citrate was taken from peak 5.

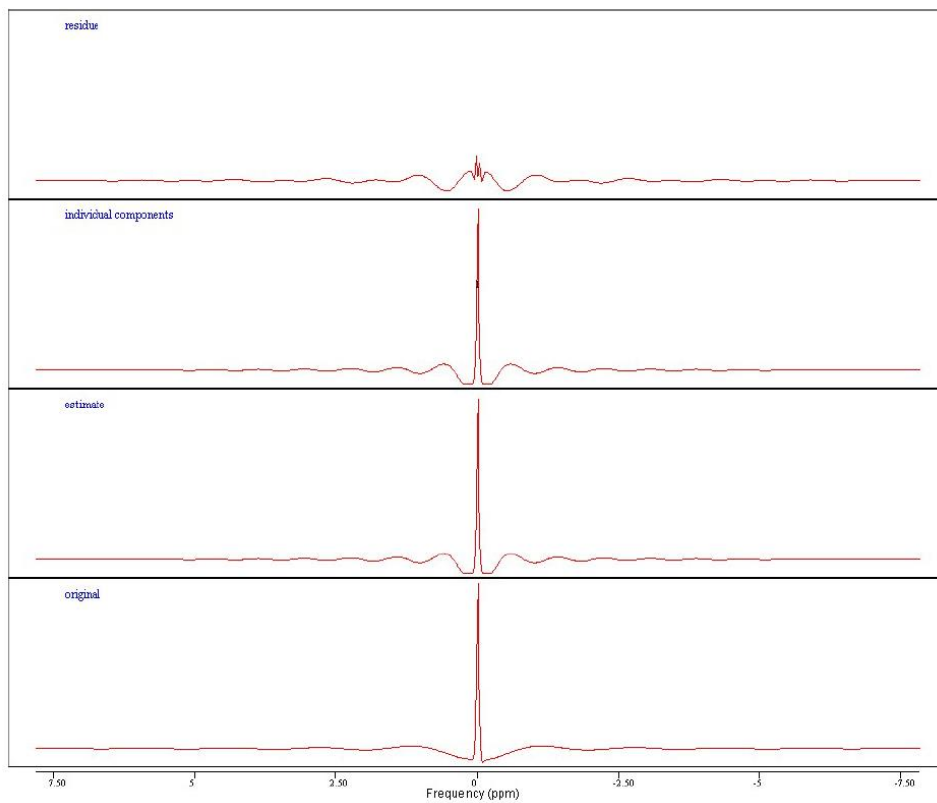


Fig. 81: Water amplitude estimation with AMARES. Automatic phase adjustment insert a first order term correction that is not needed and cannot be removed.

We immediately encountered some problems in this spectral analysis: water signals were automatically phase-corrected with first-order phase correction, introducing oscillations in the spectrum. This correction was not needed since the spectrum could be easily phased through a global phase-correction (zero-order term). We did not find solutions to remove this feature from the AMARES analysis.

Amplitude values were corrected for T<sub>2</sub>, signal fluctuations and multiplicity, as it was done for the homemade software:

Amp Cit	dAmp Cit	Amp Cho	dAmp Cho	Amp Cr	dAmp Cr
0.000096	0.000002	0.00064	0.00001	0.00044	0.00001
0.000136	0.000003	0.000393	0.000006	0.00030	0.000007
0.000232	0.000006	0.000245	0.000004	0.00024	0.000006
0.000349	0.000008	0.000185	0.000003	0.00019	0.000005
0.000536	0.000013	0.000132	0.000002	0.00015	0.000004

Table 25: Estimated amplitude values for metabolites using AMARES algorithm of jMRui, corrected for T<sub>2</sub> decay and for water concentration.

Linear regression analysis was performed between corrected amplitude values and molar concentrations in phantoms:

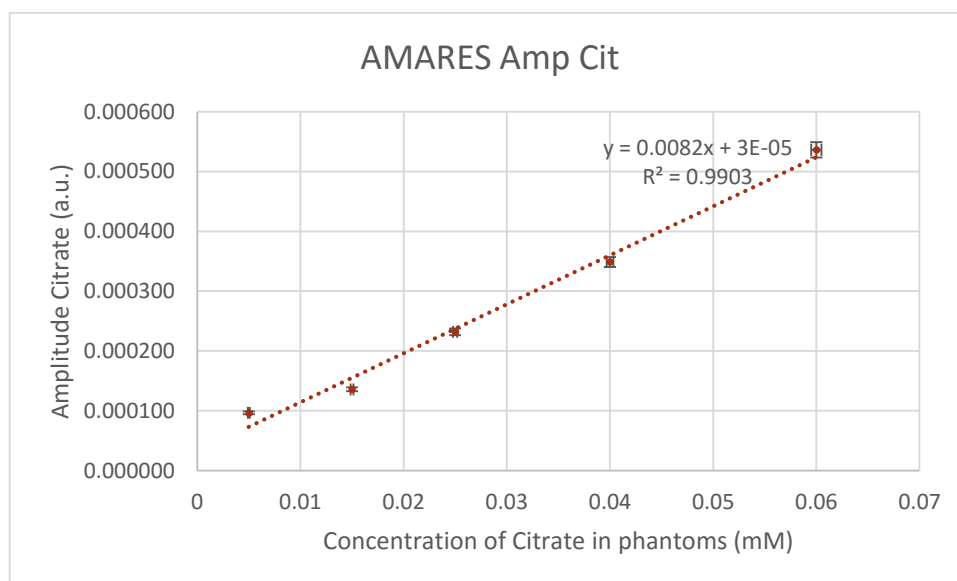


Fig. 82: Linear regression between concentration of citrate in phantoms and amplitude of peak 5 in AMARES analysis.

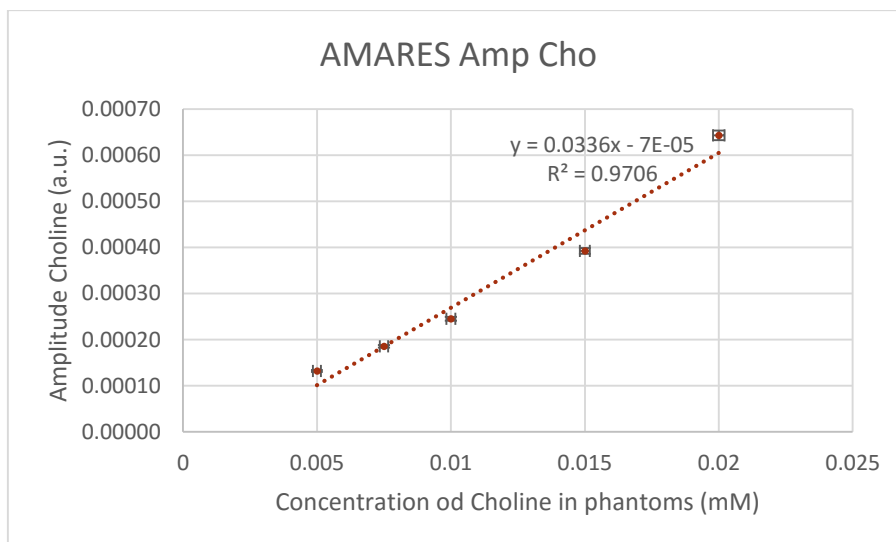


Fig. 83: Linear regression between concentration of choline in phantoms and amplitude of peak 2 in AMARES analysis.

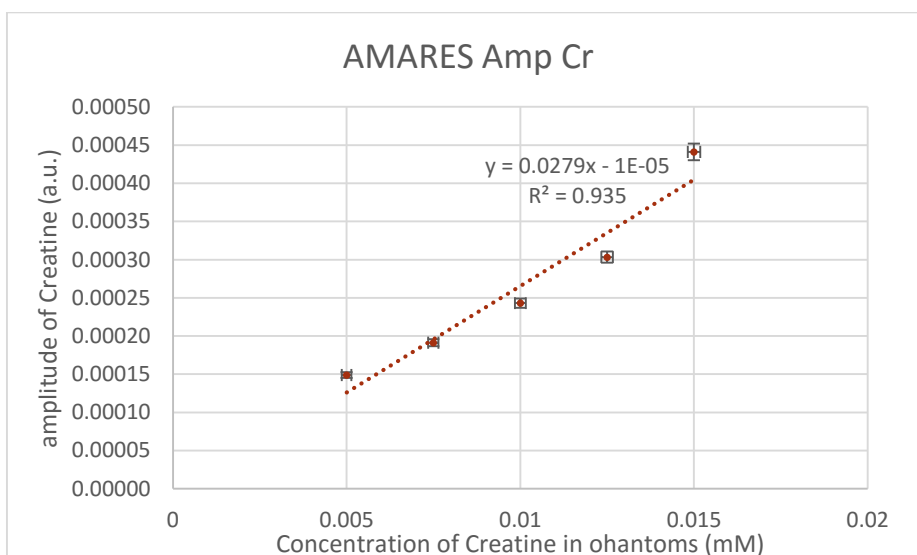


Fig. 84: Linear regression between concentration of creatine in phantoms and amplitude of peak 3 in AMARES analysis

Metabolite ratios were evaluated as we did in the previous section:

Amp (Cho+Cr)/Cit		Conc. (Cho+Cr)/Cit	
value	dvalue	value	dvalue
11.2	0.3	7.0	0.1
5.1	0.1	1.83	0.02
2.1	0.1	0.80	0.01
1.08	0.03	0.375	0.006
0.52	0.01	0.167	0.004

Table 26: Comparison between the estimated (Cho+Cr)/Cit ratios and the real ones for each phantom. The estimated values do not show a good accord to the ones estimated with the molarities of metabolites in solution.

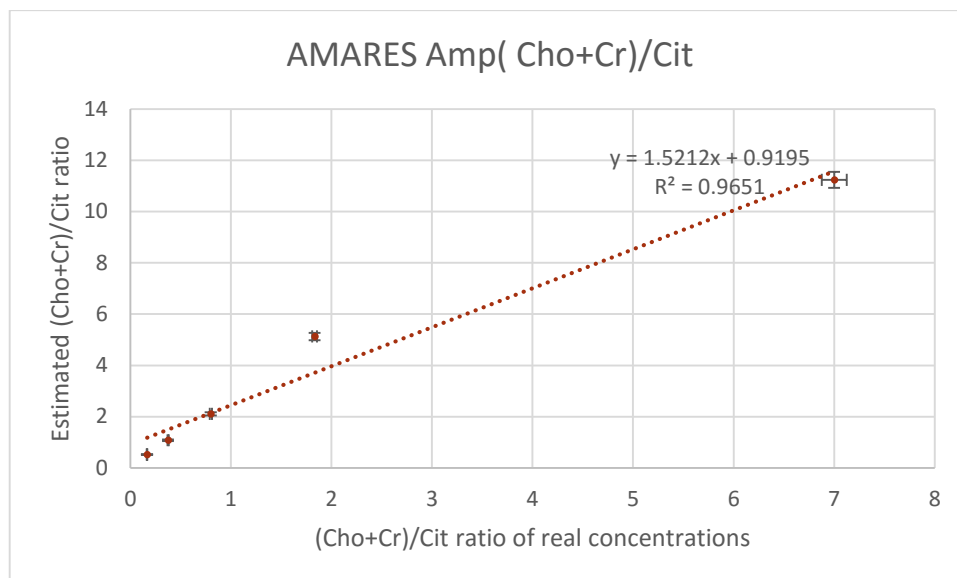


Fig. 85: Amplitude values for (Cho+Cr)/Cit ratio estimated with AMARES show poor correlation with the (Cho+Cr)/Cit ratios estimated with the concentrations of metabolites in phantoms.

Using AMARES we obtained smaller values of correlation coefficients compared to the ones we obtained with the homemade software. (Cho+Cr)/Cit ratios evaluated with AMARES amplitudes show poor agreement with the real ratios of metabolites inside the phantoms.

## 3.2 IN VIVO TESTS ON HEALTHY VOLUNTEERS

### 3.2.1 ASSESSING THE SNR RATIO

Evaluating SNR ratio in NMR spectra can be controversial because coupled spins can produce many peaks with different heights. Moreover background noise can be, not just “electronic noise”, but signal from nuclei not taken into account. One way to define an estimate for SNR is considering it referred to the signal of a peak and the noise of a region at the very beginning or at the end of the bandwidth (where there should not be signal from biological compounds). Another way is to acquire two spectra with the same sequence, one in the region of interest, where there the signal is present, and one outside in a region without signal, like the region outside the prostate next to the peripheral zone.

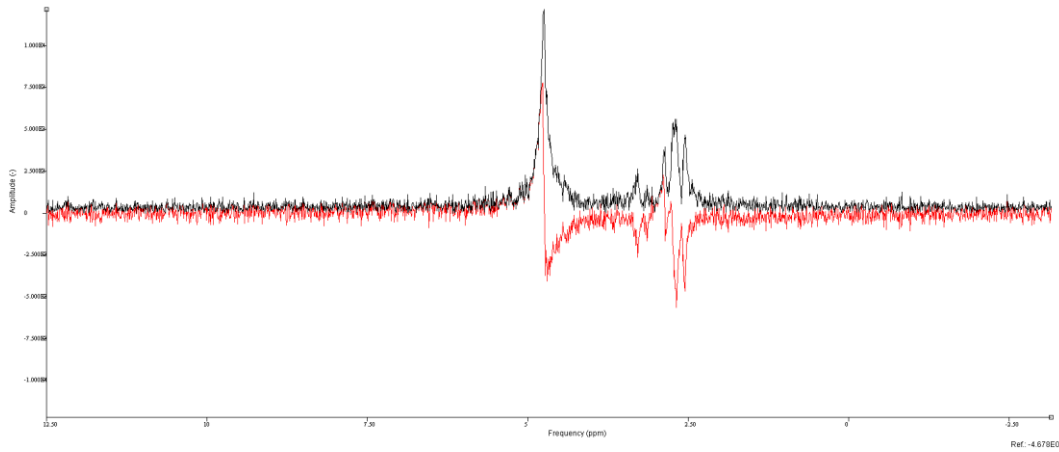


Fig. 86: Prostate NMR spectrum of a healthy volunteer taken from a multi-voxel sequence. The black line connects the points of the absolute value of the spectrum whereas the red one connects the points of the real part, the spectrum was acquired using PRESS sequence with 140 milliseconds echo time, 2000 Hz of bandwidth and 2048 points in resolution.

We can apply the first method and evaluate the noise in a “remote” region of the spectrum, for example the region of high frequencies at the left of the water peak in Fig. 86.

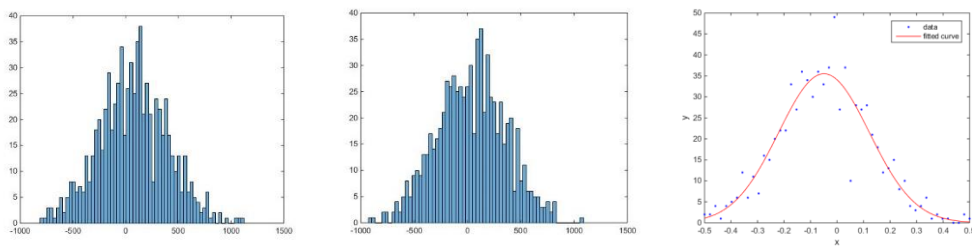


Fig. 87: On the left side, there is the histogram of the real part of the spectrum, evaluated from 5.88 ppm to the end of the spectrum (from channel 1300 to channel 2048). In the center, there is the histogram of the imaginary part evaluated on the same interval. Gaussian line-shape can be recognized from both images, on the right side there is an example of Gaussian fitting of the real part, “Gaussianity” was proved through Kolmogorov-Smirnov test ( $D$ -value  $\sim 0.033$ , critical value  $\sim 0.039$ ).

At first sight, the histograms of the noise in Fig. 87 seem Gaussian and centered on zero value, thus indicating that the region from 5.88 ppm can be suitable to evaluate the noise of the spectrum. Evaluating the same histogram on the modulus spectrum on Fig. 92 we find the so called Rayleigh distribution always found on the modulus of complex number where the real and imaginary part are normally distributed with equal variance and zero mean.

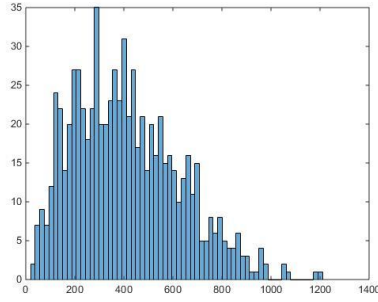


Fig. 88: Histogram of the absolute value of the spectrum, evaluated from 5.88 ppm to the end of the spectrum (from channel 1300 to channel 2048).

Standard deviations were evaluated in the selected interval and are reported below.

<i>St. Dev of the Real part (a.u.)</i>	<i>St. Dev of the Imaginary part (a.u.)</i>
325	322

Table 27: Standard deviations of the real and imaginary part of the spectrum.

The estimates in Table 27 are quite similar, as they differ for 1% of their values. Using the standard deviation of the real part to evaluate signal to noise ratio we find: SNR of 8.2 for total choline, 5.3 for total creatine and 17.0 for the top peaks of citrate, considering for signal, the top peak value of the in-phase real part, or the modulus. We can compare these results with the SNR evaluated with the second method. Taking a spectrum outside the prostate Fig. 89, as described before, it is possible to compute the standard deviation of the real and the imaginary part on 2048 points as pictured in Fig. 90.

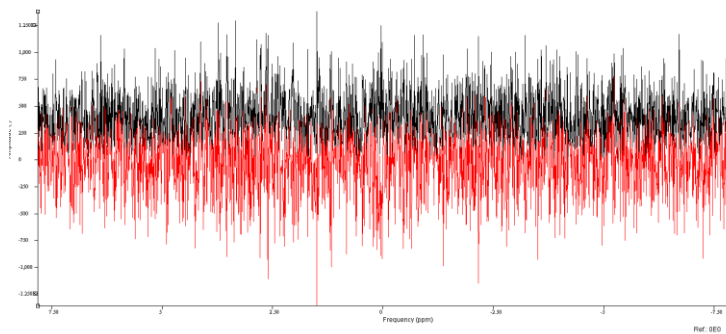


Fig. 89: Spectrum taken from a multi-voxel sequence in a region outside the prostate, without recognizable signals.

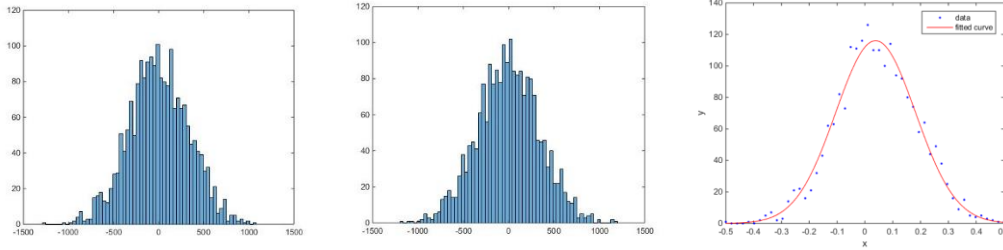


Fig. 90: histograms of the real(left) and the imaginary(center) part of the noise spectrum acquired outside the prostate, next to the peripheral zone, all the 2048 points were used. Gaussian line-shape can be recognized from both images and through Kolmogorov-Smirnov test ( $D$ -value  $\sim 0.016$ , critical value  $0.023$ ). Gaussian fit of the real part is shown on the right of the image.

The histograms seem Gaussian and centered on zero again. Another confirm of the “Gaussianity” of the noise is Fig. 91 in which can be recognized the Rayleigh distribution.

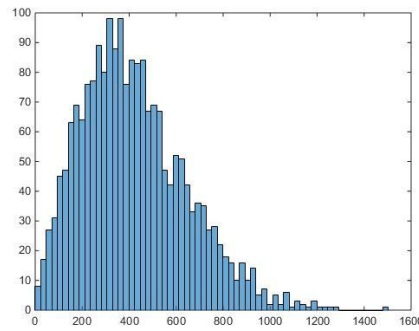


Fig. 91: histogram of the absolute value of the noise spectrum acquired outside the prostate, next to the peripheral zone all the 2048 points were used.

<i>St. Dev of the Real part (a.u.)</i>	<i>St. Dev of the Imaginary part (a.u.)</i>
332	341

Table 28: Standard deviations of the real and imaginary part of the spectrum evaluated in a spectrum without recognizable signal, outside the prostate, next to the peripheral zone.

Values of computed standard deviations in Table 28 are quite similar to the ones in Table 1 and similar to each other also because it is common practice to assign only the first significance figure to an error estimate. Then we find SNR equal to 8.0 for top peak of choline, 5.0 for top peak of creatine and 16.9 for top peaks of citrate, thus confirming the poor SNR ratio of acquired prostate spectra in common multi-voxel sequences.



### 3.2.2 MEASURE OF THE IN VIVO PARAMETERS OF CITRATE

Spectral parameters of citrate were measured from spectra acquired with a 3-D PRESS on a healthy volunteer with 2048 points in resolution, 2000 Hz of bandwidth, TE=140 ms and TR=1500. The spectra with the best SNR were averaged together to improve the precision of the estimation, six spectra were chosen from the 315 of the 3-D PRESS.

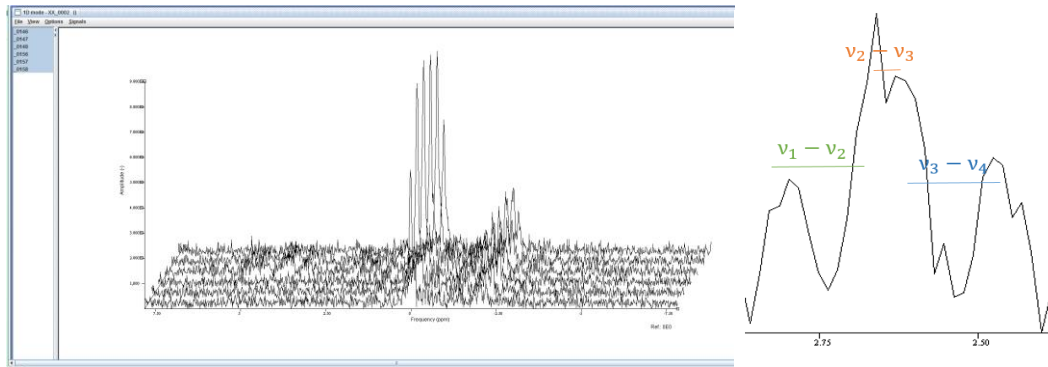


Fig. 92: Absolute value of the spectra with best SNR in a multi-voxel acquisition on a healthy volunteer (left). Selected signals were averaged to obtain a more robust estimate of the distances between peaks (right).

With 2048 points spectral resolution should be around 1 Hz, but because of experimental conditions it was impossible to discriminate signals within 4 Hz (~0.03 ppm), and thus uncertainty on the averaged peaks become:

$$\Delta v = \frac{0.03}{\sqrt{6}} = 0.012 \text{ ppm}$$

$v_1$ (ppm)	$v_2$ (ppm)	$v_3$ (ppm)	$v_4$ (ppm)	$dv$ (ppm)
2.770	2.645	2.614	2.468	0.012

Using the relations in Eq.( 40 ) we find:

$$\delta = (2.62 \pm 0.1) \text{ ppm} \quad v_A - v_B = (0.1 \pm 0.5) \text{ ppm} \quad j_{AB} = (17 \pm 2) \text{ Hz}$$

In agreement with the results of García-Martín et al (41).

---

### 3.3.3 FIT OF IN VIVO PROSTATE SPECTRA

From the first healthy volunteer we took a single-voxel scan and a 3-D PRESS with 1024 points in resolution, from the second one we took a 3-D PRESS with 2048 points, all the sequences were acquired with a TE=140 ms and a TR of 1500 ms. Since we can't confirm the goodness of previsions made by the homemade software on in vivo measurements (we could not make the biopsy of healthy volunteers' prostates), the main aim of this part of the work is to test the ability of the algorithm to fit prostate spectra of healthy volunteers in low SNR conditions (SNR not greater than 17 for top peak citrate, 9 for choline and 6 for creatine in multi-voxel acquisitions). Spectra were analyzed using QUEST, AMARES and the homemade software, in this section you will find overall considerations of the analyses and some examples of fitted spectra.

#### QUEST

Simulation parameters of Fig. 93 were used for citrate (it was not used the script file of the homemade software but the parameters inside it) chemical shift and multiplicities of choline and creatine where chosen to produce single peaks at frequencies of 2.27, 3.0 and 3.9 ppm (we considered also the second resonance of creatine). Pulse sequence was programmed to be an ideal sequence (Since Philips did not give us detailed and quantitative information about the sequences), parameters used in the simulation are shown in Fig. 94. Simulated spectra used for quantitation are showed in Fig. 95 instead.

```
SysName (2) : citrate - Name of spin system
NSpins (0) : 2 - Number of spins in spin system
Iso(0) (2) : 1H - Spin Isotope Type
Iso(1) (2) : 1H - Spin Isotope Type
PPM(0) (1) : 2.602 - Shift of spin 0 (PPM)
PPM(1) (1) : 2.708 - Shift of spin 1 (PPM)
J(0,1) (1) : 16.8 - Scalar coupling (Hz)
Omega (1) : 127.768332 - Spec. Freq. in MHz (1H based)
```

*Fig. 93: Simulation parameters for in vivo citrate.*

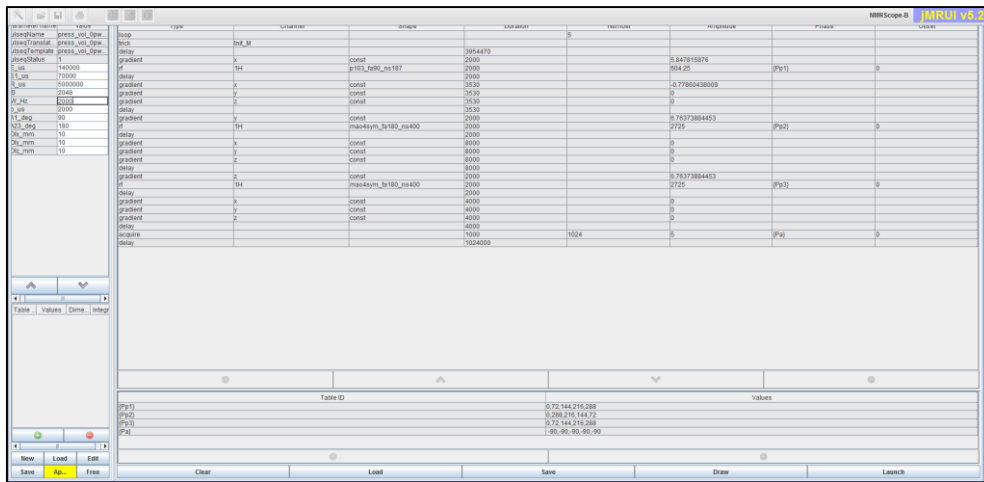


Fig. 94: Sequence parameters for NMRScopeB simulation: TR=1500 ms, TE=140 ms, bandwidth=2000 Hz, voxel size of  $1 \times 1 \times 1 \text{ cm}^3$ , ideal pulses.

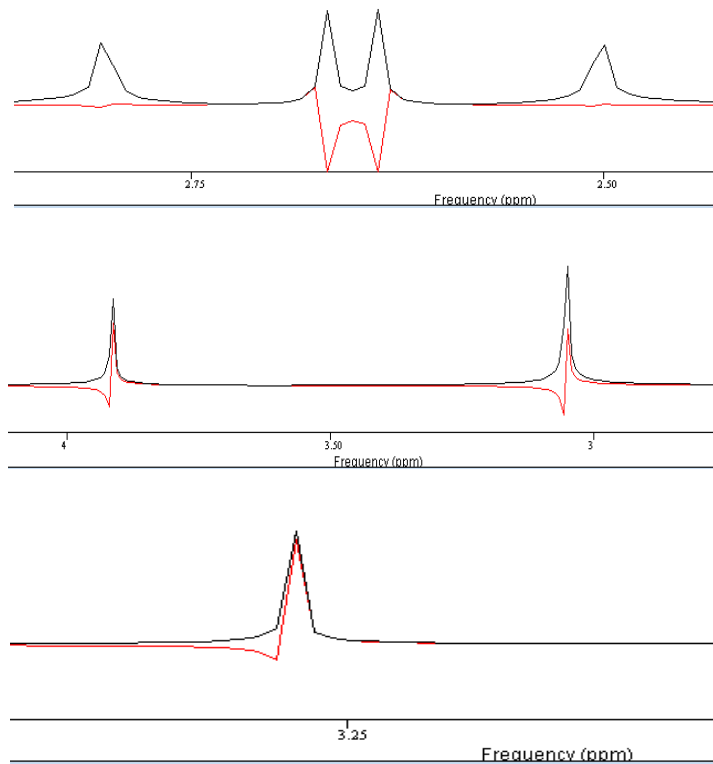


Fig. 95: Simulated basis for QUEST analysis, the red line is the real part of the spectrum while the black one is the absolute value.

QUEST analysis of the acquired spectra produced bad results, since after many attempts we did not obtain a single well fitted spectrum, the algorithm was able to recognize signals with “great” SNR like the one of citrate but ignored completely the presence of the other metabolites. Examples of this behavior are shown in Fig. 96 and in Fig. 97 in which creatine and choline were not fitted correctly.

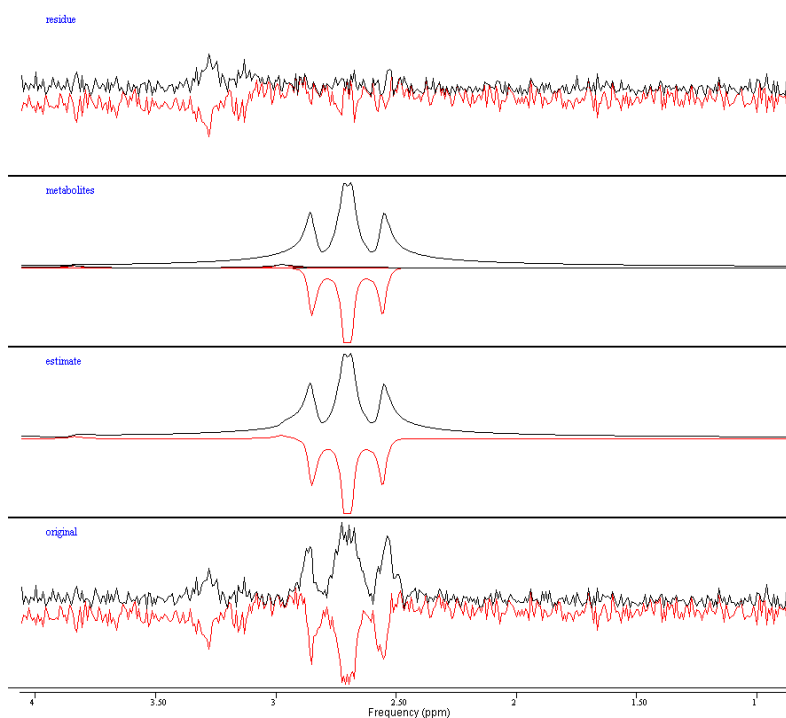


Fig. 96: Prostate spectrum taken from a multi-voxel acquisition (spectrum n° 166) of a healthy volunteer with 2048 points in resolution. The black line is the modulus of the spectrum, while the red one is its real part. Citrate was correctly fitted by the algorithm while choline and creatine were completely ignored.

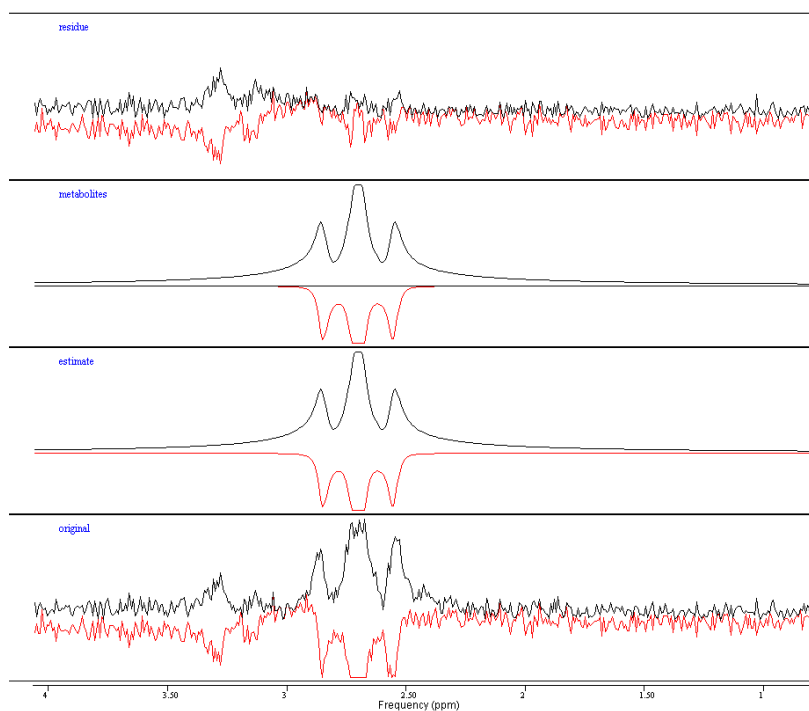


Fig. 97: Prostate spectrum taken from a multi-voxel acquisition (spectrum n° 157) of a healthy volunteer with 2048 points in resolution. The black line is the modulus of the spectrum, while the red one is its real part. Again citrate was correctly fitted by the algorithm while choline and creatine were completely ignored.

## AMARES

Although the use of AMARES is ill-posed for metabolites with coupled protons we made a trial by representing in vivo citrate with three peaks:

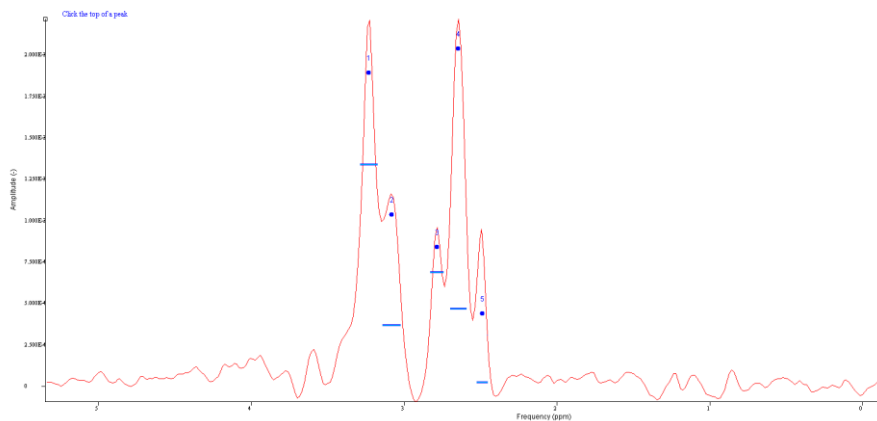


Fig. 98: Peak-picking in AMARES for a single-voxel spectrum (real part) with 1024 points in resolution. Apodization of 2.7 Hz was previously done to increase the SNR. Citrate was modeled with three peaks.

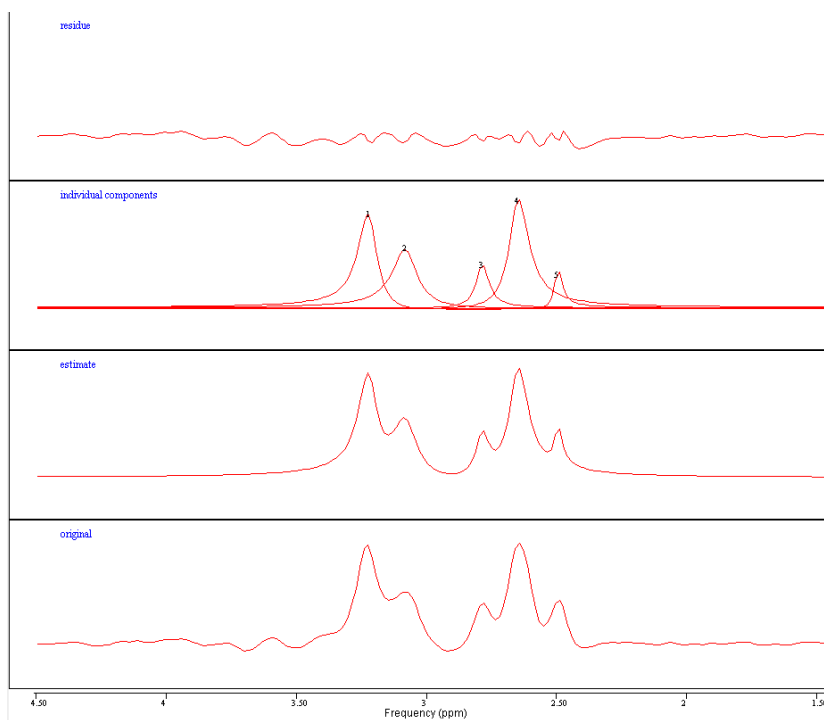
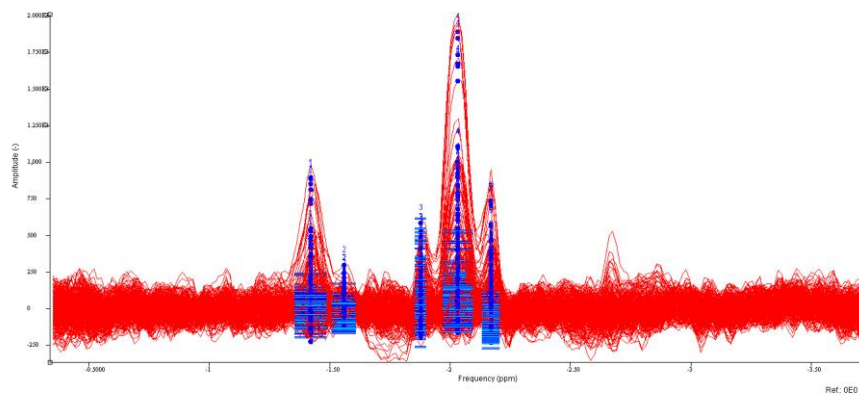


Fig. 99: single-voxel spectrum with 1024 points in resolution analyzed by AMARES, apodization of 2.7 Hz was previously done to increase the SNR. Low residue and a reasonable fit are achieved for this single-voxel spectrum.

In Fig. 99 is shown an example of quantifications performed by using AMARES on a spectrum taken from a single-voxel sequence. In general AMARES produced better

results than QUEST, since the residue of quantifications was lower than the ones obtained with QUEST. Proper pre-processing was needed to increase SNR: to produce acceptable results, in vivo spectra were filtered through Lorentzian smoothing (apodization) of two Hertz at least (see Fig. 99). Considering the spectra obtained with the 3-D PRESS, the great advantage of the jMRui package, respect to other software for MRS analysis, is the possibility to analyze all the signals from a multi-voxel at the same time, as can be seen from Fig. 100. Anyway we achieved satisfying modeling only for single-voxel spectra, while for multi-voxel signals (which have a lower SNR) fitting of the spectra was usually incomplete (Fig. 101 and Fig. 102).



*Fig. 100: Parallel analysis of the 315 spectra of a 3-D PRESS, using AMARES.*

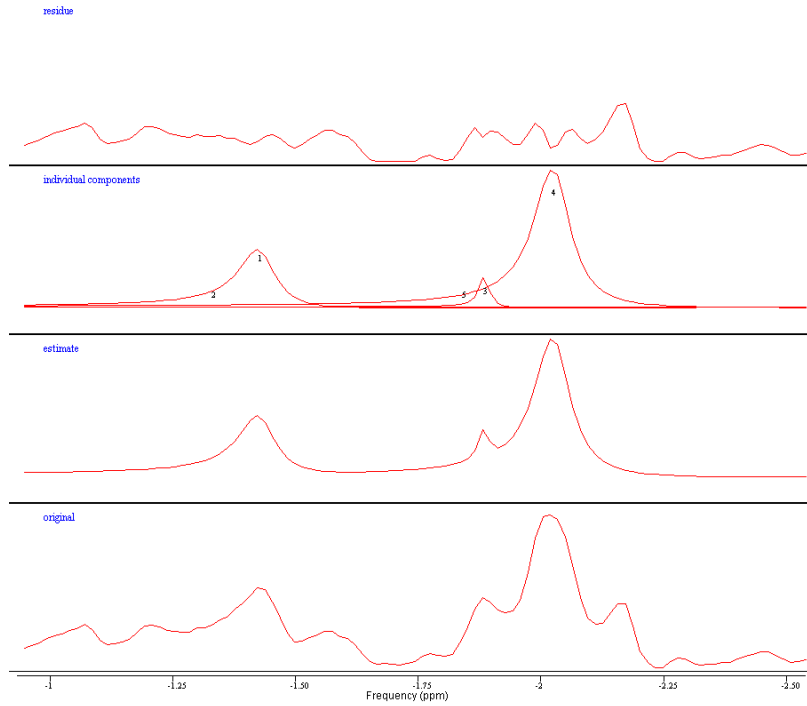


Fig. 101: Quantitation of one of the spectra taken from a multi-voxel sequence (spectrum n°157) with 2048 points, using AMARES. Only partial quantification is achieved, since one of the peaks of citrate and creatine were ignored in the analysis. Apodization of 2.3 Hz was previously done.

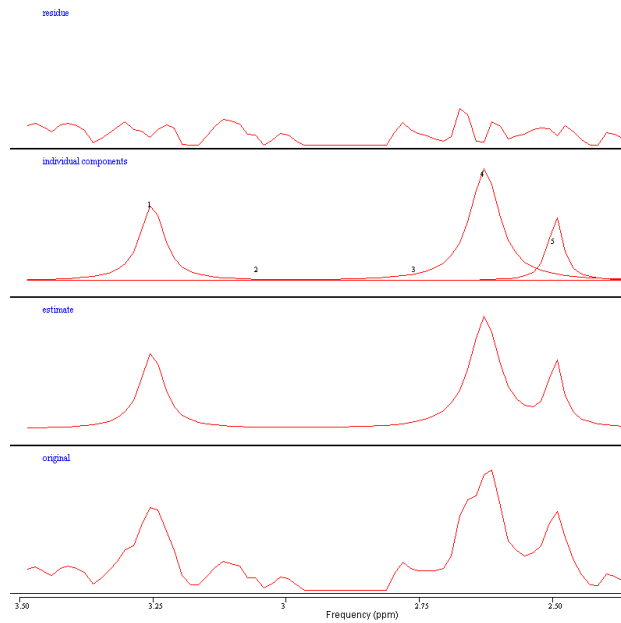


Fig. 102: Quantitation of one of the spectra taken from a multi-voxel sequence (spectrum n°139) with 1024 points, using AMARES. Only partial quantification is achieved, since one of the peaks of citrate and creatine were ignored in the analysis. Apodization of 3.15 Hz was previously done to improve SNR.

## Homemade software

Analysis of the in vivo spectra was done with the homemade software using the parameters for citrate described in Fig. 93, choline methyl proton was simulated as a single peak centered at 3.29 ppm while creatine methyl resonance was set to 3.1 ppm. Simulated PRESS sequence was programmed to have 140 ms of echo time, with acquisition parameters determined by the bandwidth and the resolution of the real acquisitions. All the spectra were analyzed between 2.1 and 3.6 ppm to exclude from the analysis residual water and fat peaks. The acquired FIDs were smoothed through the function *decay()* of Fig. 47 with a T2\* of 150 ms, that corresponds approximately to an apodization of 3.5 Hz for spectra with 1024 points and to 7.3 Hz for spectra with 2048 points. Some examples of quantification of in vivo spectra using the homemade software are shown below:

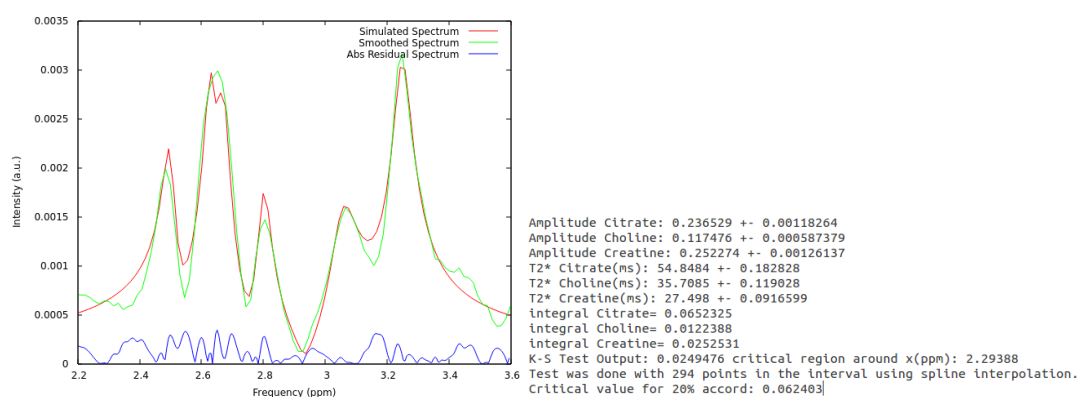


Fig. 103: Single-voxel spectrum with 1024 points in resolution analyzed with the homemade software. A  $D$ -value of 0.021 was achieved with critical value of 0.070 of 20% probability that differences between real and fitted spectrum might be produced by chance.

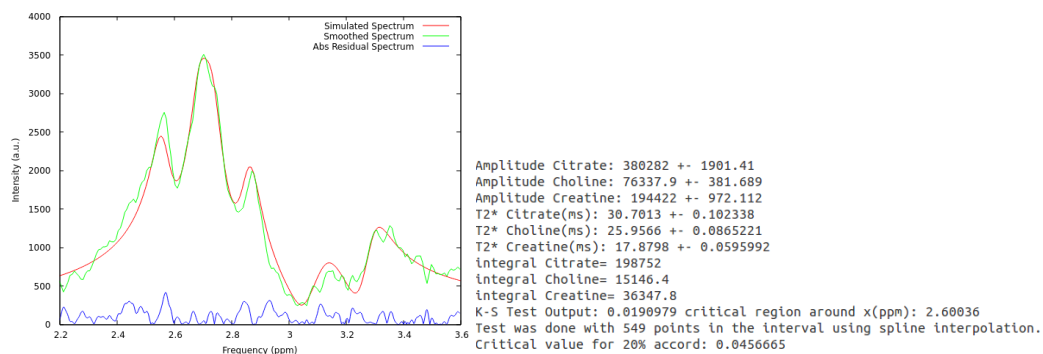


Fig. 104: Spectrum taken from a multi-voxel sequence (spectrum n°166) with 2048 points in resolution analyzed with the homemade software. A  $D$ -value of 0.019 was achieved with critical value of 0.046 of 20% probability that differences between real and fitted spectrum might be produced by chance.



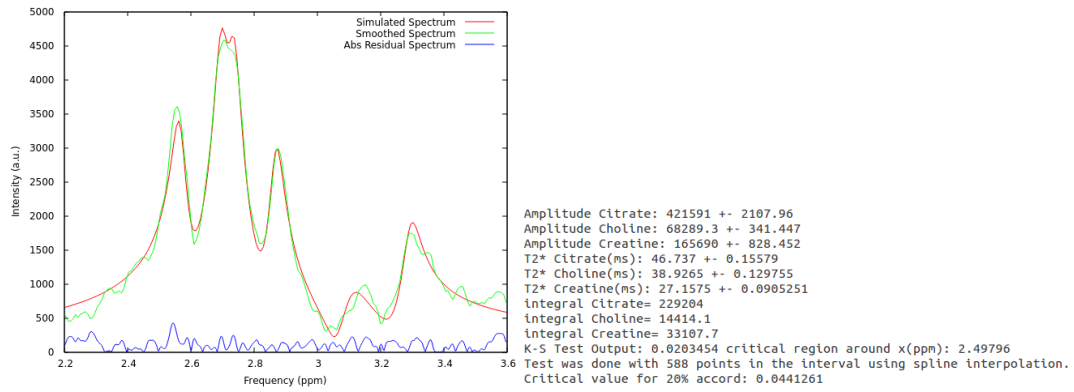


Fig. 105: Spectrum taken from a multi-voxel sequence (spectrum n°157) with 2048 points in resolution analyzed with the homemade software. A  $D$ -value of 0.020 was achieved with critical value of 0.044 of 20% probability that differences between real and fitted spectrum might be produced by chance.

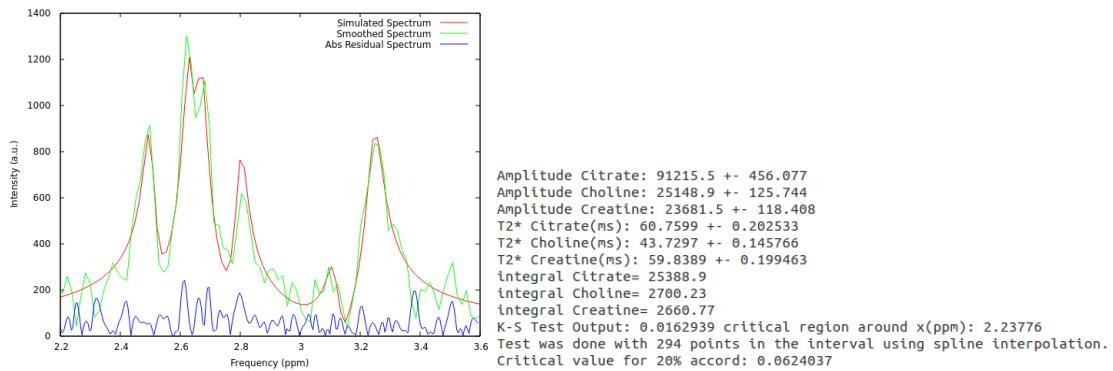


Fig. 106: Spectrum taken from a multi-voxel sequence (spectrum n°139) with 1024 points in resolution analyzed with the homemade software. A  $D$ -value of 0.016 was achieved with critical value of 0.062 of 20% probability that differences between real and fitted spectrum might be produced by chance.

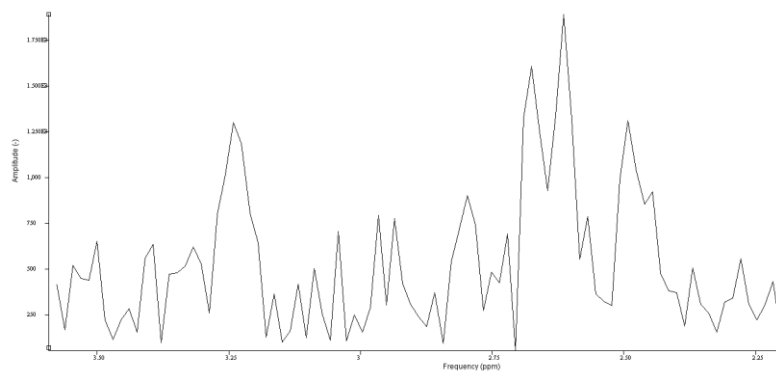


Fig. 107: Modulus of the spectrum n° 139, taken from a multi-voxel sequence with 1024 points in resolution, without proper smoothing. SNR for choline peak is  $\sim 6$ , for creatine is  $\sim 4$  and for the highest peak of citrate is  $\sim 9$  (SNR evaluated on the real part of the spectrum).

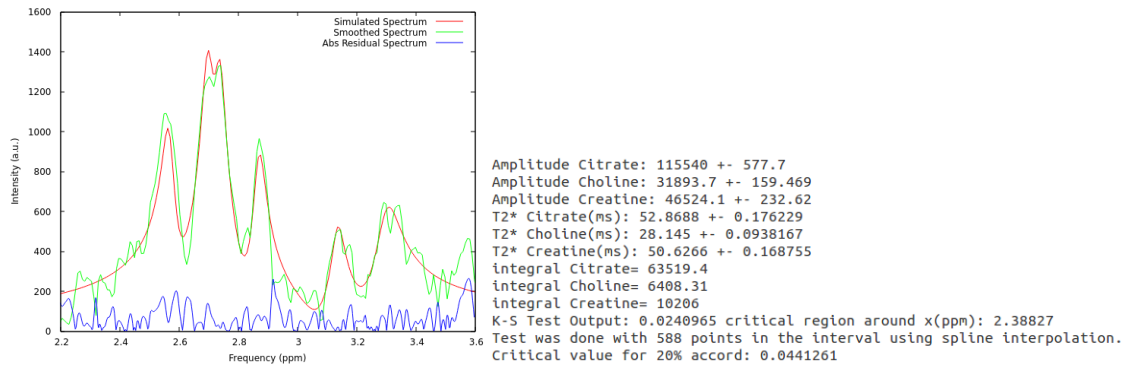


Fig. 108: Spectrum taken from a multi-voxel sequence (spectrum n°229) with 2048 points in resolution analyzed with the homemade software. A D-value of 0.024 was achieved with critical value of 0.062 of 20% probability that differences between real and fitted spectrum might be produced by chance.

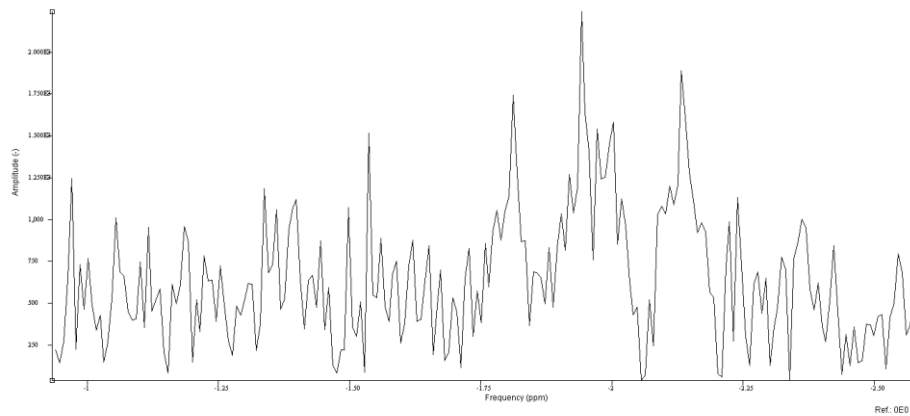


Fig. 109: Modulus of the spectrum n° 229, taken from a multi-voxel sequence with 2048 points in resolution, without proper smoothing. SNR for choline peak is ~3, for creatine is ~2 and for the highest peak of citrate is ~7(SNR evaluated on the real part of the spectrum).

The homemade software produced almost always good results in terms of fitting. D-values for the K-S test are smaller than critical values for all the examined spectra. Fitting of the spectra was achieved also for low SNR conditions, as it is showed in Fig. 106, Fig. 107, Fig. 108 and Fig. 109 where really noisy signals from multi-voxel spectra of 1024 and 2048 points were analyzed.

## 4 CONCLUSIONS

The main aim of this work was to propose a new strategy to quantify metabolites from prostate MR spectra to improve the power of non-invasive diagnostics for PCa. For this purpose a new homemade software, based on iterative MRS simulations provided by GAMMA, was firstly tested on phantoms made at IRST laboratories and then on spectra taken from healthy volunteers. At the beginning of the research the manufactured phantoms were made following the directives of AAPM by using  $\text{CuSO}_4$  to set a proper relaxation time to water. After having found the correct quantity of  $\text{CuSO}_4$  to reproduce the transverse relaxation time of water in the peripheral zone of the prostate we encountered problems while using it with metabolites. Addition of the paramagnetic salt to the phantoms containing a solution of metabolite degraded completely the spectrum of citrate (as can be seen from Fig. 56). This might be produced by cation binding between citrate and copper ions, but further investigations are needed. Waiting for tests with other relaxation agents, we decided not to add any paramagnetic salt to the homemade phantoms used for quantification tests. A rough estimate of spectral parameters of citrate was done by measuring the different frequencies of the peaks in its spectrum using the theory developed in chapter one. Significant differences in the coupling constant were not observed by changing the pH of the solution (from pH 7 to pH 5), conversely different line-shapes (Fig. 62 and Fig. 63) and different values of chemical shifts (Table 13) were observed. Because of the uncertainties of the estimated parameters (due to the resolution and field uniformity of a clinical MR scanner), the choice of j-coupling constants and Larmor frequencies for simulation was not univocal. Spectral parameters of methylene protons of citrate were then estimated empirically within the uncertainties of the measured quantities in Table 13. Relaxation times were then measured by the use of sequences with long repetition time (since no relaxation agent was inserted in the test phantoms) to determine the correction factors needed to compensate for transverse relaxation processes in metabolite quantifications. In section 3.1.4 we tested the ability of the MR scanner and the homemade software to quantify the MR spectra of the phantoms, subsequently we compared the results with the quantifications carried out using AMARES (section 3.1.5). We found strong correlations with the real molarity of the metabolite in the phantoms both for the amplitude and the total signal of citrate estimated with the homemade software, thus confirming the reliability of the model used to represent the molecules.

Moreover, correct values of the (Cho+Cr)/Cit ratio were obtained with the estimated quantities, both with amplitudes and total signal again. An analogue analysis was done using AMARES but weaker correlations were found (in terms of Pearson's correlation coefficients) and the estimated (Cho+Cr)/Cit ratios were not in agreement with the real molar concentrations in the phantoms. The last part of this work concerned in vivo tests on healthy volunteers. Only two 3-D PRESS and a single-voxel scan were acquired from two subjects. The limited number of acquisitions of prostate spectra was due to the fact that many features of the new Ingenia 3T had to be analyzed at the IRST institute, like imaging and diffusion techniques. So, as magnetic resonance examinations are time-consuming, this was the best we could do in this first part of the research. First of all, a rough estimate of the spectral parameters was performed, as we did in phantom tests, to find a range of values for in vivo citrate. Then the fitting ability of the homemade software was tested on common prostate spectra with low SNR. Low D-values for the K-S test were achieved (compared with the critical values), thus confirming the good agreement between the simulated spin systems and the real ones inside the prostate. Fitting capabilities of QUEST and AMARES of the jMRui package were also tested but the overall results were poor. In many occasions these algorithms ignored completely the presence of choline and creatine (or some peaks of citrate while using AMARES), moreover quantification of citrate by using AMARES have some controversial theoretical aspects: the FID has to be modeled with three or four independent damped oscillating functions (AMARES works on time-domain) ignoring the fact that it is a strong coupled 2(AB) system.

In conclusion we can say that the homemade software showed good quantification capabilities in phantom tests and that the fitting algorithm worked well for in vivo spectra in low SNR conditions. Quantification of citrate is one of the main problems concerning MRS of the prostate but the results we obtained seemed to be quite accurate using this approach. For example by comparing these results to the ones obtained by McLean et al. (44), a worse fit of citrate was achieved for in vivo spectra using LCModel. Further tests are certainly needed to assess if this kind of strategy could help the non-invasive diagnostics of PCa at an early stage, in particular the purposes for future research are:

- More phantom tests using relaxation agents different from  $\text{CuSO}_4$ , for example by using gadolinium to reproduce more realistic relaxation times of the metabolites.

- More in vivo test on healthy volunteers, increasing spectral resolution with a better preparation of the volunteer for the exam.
- The inclusion of spermine and other polyamines in the analysis, since the numerous peaks of this compounds are overlapped to the ones of choline and creatine.
- Make tests on patients, also comparing the output of the MRS analysis to the Gleason score of the biopsies of the prostate.
- Development of a phantom for multi-voxel analysis of the prostate capable of reproducing the correct line-shape of citrate, this might be achieved by inserting the physiological concentration of cations and giving a proper density by using agarose gel.

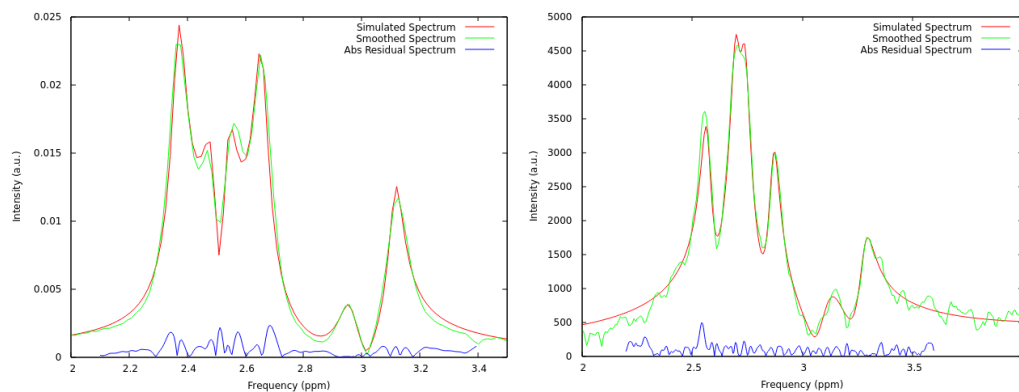


Fig. 110: The homemade software showed to be suitable for metabolite quantifications in phantom tests (left) and produced low  $D$ -values for  $K$ - $S$  Test on in vivo measurements (right).

Finally, I wish to comment, by the impressions I had in my short experience, that magnetic resonance spectroscopy is a powerful technique capable of determining the presence and the quantity of a variety of compounds inside human body without invasive procedures. MRS is also a complex subject and controversial results can actually be found without doing it properly, for example by running black-box programs for analysis and looking only at their numerical output without checking if signal acquisition was done correctly (for example a bad water suppression can produce artifacts interpretable as metabolite signals). Thus, more research is still needed for prostate MRS, but it is also important to give information about the theoretical principles of this technique to radiologists and technicians who use it in clinical practice.

## BIBLIOGRAPHY

1. *Cancer statistics*. Siegel R., Naishadham D. and Jemal A., 2012, CA: A Cancer Journal for Clinicians, Vol. 62, pp. 10–29.
2. *A Meta-Analysis of the Accuracy of Prostate Cancer Studies Which Use Magnetic Resonance Spectroscopy as a Diagnostic Tool*. Peng Wang, You-min Guo, Min Liu, Yong-qian Qiang, Xiao-juan Guo, Yi-li Zhang, Xiao-Yi Duan, Qiu-Juan Zhang, Weifeng Liang. 2008 Sep-Oct, Korean Journal of Radiology, Vol. 9(5), pp. 432–438.
3. *Three-Dimensional Magnetic Resonance Spectroscopic Imaging of Brain and Prostate Cancer*. John Kurhanewicz, Daniel B. Vigneron and Sarah J. Nelson, 2000 Jan, Neoplasia, Vol. 2, pp. 1-2.
4. *Prostate cancer in magnetic resonance imaging: diagnostic utilities of spectroscopic sequence*. Rocchina Caivano, Patrizia Cirillo, Antonio Balestra, Antonella Lotumolo, Giovanna Fortunato, Luca Macarini, Alexis Zandolino, Giulia Vita and Aldo Cammarota. 2012, Journal of Medical Imaging and Radiation Oncology, Vol. 56, pp. 606–616.
5. *Validation of multiparametric magnetic resonance imaging and spectroscopy (DWI/MRSI) to assess prostate cancer aggressiveness*. T. Kobus, T. Hambroek, C. Hulsbergen - Van de Kaa, J. Barentsz, A. Heerschap and T. Scheenen. 2010, Proc. Intl. Soc. Mag. Reson. Med., Vol. 10, p. 477.
6. Gleason grading system. [Online] Wikimedia Foundation, Inc. [https://en.wikipedia.org/wiki/Gleason\\_grading\\_system#cite\\_note-urlMale\\_Genital\\_Pathology-1](https://en.wikipedia.org/wiki/Gleason_grading_system#cite_note-urlMale_Genital_Pathology-1).
7. *Ultra high field NMR spectroscopic studies on human seminal fluid, seminal vesicle and prostatic secretions*. Lynch MJ, Masters J, Pryor JP, Lindon JC, Spraul M, Foxall PJ, Nicholson JK. 1994, J Pharm Biomed, Vol. 12, pp. 5–19.
8. *Citrate metabolism of normal and malignant prostate epithelial cells*. Costello LC, Franklin RB. 1997, Urology, Vol. 50, pp. 3-12.
9. *Detection of increased choline compounds with proton nuclear magnetic resonance spectroscopy subsequent to malignant transformation of human prostatic epithelial*

cells. Ackerstaff E, Pflug BR, Nelson JB, Bhujwala ZM. 2001, *Cancer Res*, Vol. 61, pp. 3599–3603.

10. *Intracellular compartmentation, structure and function of creatine kinase isoenzymes in tissues with high and fluctuating energy demands: The 'phosphocreatine circuit' for cellular energy homeostasis.* Wallimann T, Wyss M, Brdiczka D, Nicolay K, Eppenberger HM. 1992, *Biochem J*, Vol. 281, pp. 21-40.

11. *Polyamines and prostatic cancer.* Schipper RG, Romijn JC, Cuijpers VMJI, Verhofstad AAJ. 2003, *Biochem Soc T*, Vol. 31, pp. 375–380.

12. *Quantitation of magnetic resonance spectroscopy signals: the jMRUI software package.* D. Stefan, F. Di Cesare, A. Andrasescu, E. Popa, A. Lazariiev, E. Vescovo, O. Strbak, S. Williams, Z. Starcuk, M. Cabanas, D. van Ormondt and D. Graveron-Demilly. 10, 2009, *Measurement Science and Technology*, Vol. 20, p. 104035.

13. *Automatic quantitation of localized in vivo 1H spectra with LCModel.* Stephen W. Provencher. 2001, *NMR in Biomedicine*, Vol. 14, pp. 260–264.

14. *An algorithm for the automated quantitation of metabolites in in vitro NMR signals.* Greg Reynolds, Martin Wilson, Andrew Peet and Theodoros N. Arvanitis. 6, 2006, *Magnetic Resonance in Medicine*, Vol. 56, pp. 1211–1219.

15. *Evaluation of short-TE 1H MRSI for quantification of metabolites in the prostate.* Meer Basharat, Maysam Jafar, Nandita M. deSouza and Geoffrey S. Payne. 2014, *NMR Biomed*, Vol. 27, pp. 459–467.

16. *Quantitative 1H MR Spectroscopic Imaging of the Prostate Gland Using LCModel and a Dedicated Basis-Set: Correlation with Histologic Findings.* M. L. García-Martín, M. Adrados, M. P. Ortega, I. Fernández González, P. López Larrubia, J. Viano, and J. M. García-Segura. 2011, *Magnetic Resonance in Medicine*, Vol. 65, pp. 329–339.

17. *Effect of cation binding on the proton chemical shifts and the spin-spin coupling constant of citrate.* Van der Graaf M, Heerschap A. 1996, *J Magn Res B*, Vol. 112, pp. 58-62.

18. *Density functional theory calculations of the nuclear magnetic resonance spin-Hamiltonian parameters for two polyamines of prostate tissue: spermidine and spermine.*

- Z. Atieh, A. R. Allouche, D. Graveron-Demill, F. Fauvelle and M. Aubert-Frecon. 2009, *Measurement Science and Technology*, Vol. 20, p. 104024 (8pp).
19. Becker, Edwin D. *High Resolution NMR, Theory and Chemical Applications, Third Edition*. Academic Press, 2000.
20. Lamb, W E. 1941, *Phys. Rev.*, Vol. 60, p. 817.
21. Ramsey, N. F. 1950, *Phys. Rev.*, Vol. 78, p. 699.
22. Graaf, Robin A. de. *In Vivo NMR Spectroscopy – 2nd Edition: Principles and Techniques*. John Wiley & Sons, 2007.
23. *Spin Echo Measurements of Nuclear Spin Coupling in Molecules*. E. L. Hahn and D. E. Maxwell, 1952, *Physical Review*, Vol. 8, pp. 1070-1083.
24. *Quantitative measurement of small through-hydrogen-bond and 'through-space' <sup>1</sup>H-<sup>113</sup>Cd and <sup>1</sup>H-<sup>199</sup>Hg J couplings in metal-substituted rubredoxin from Pyrococcus*. Blake PR, Lee B, Summers MF, Adams MW, Park JB, Zhou ZH, Bax A. 5, 1992, *Journal of Biomolecular NMR*, Vol. 2, pp. 527-533.
25. Keeler James. *Understanding NMR Spectroscopy, 2nd Edition*. Wiley & Sons, April 2010.
26. Gordon S. Rule, T. Kevin Hitchens. *Foundamentals of Protein NMR Spectroscopy*. Springer, 2006.
27. Levitt, Malcolm H. *Spin Dynamics: Basics of Nuclear Magnetic Resonance, 2nd Edition*. Wiley and Sons, March 2008.
28. *Fast Fourier transform*. [Online]  
[https://en.wikipedia.org/wiki/Fast\\_Fourier\\_transform](https://en.wikipedia.org/wiki/Fast_Fourier_transform).
29. Donald W. McRobbie, Elizabeth A., Moore Martin, J. Graves and Martin R. Prince. *MRI From Picture to Proton: Second edition*. Cambridge University Press, 2006.
30. Nietlispach, Daniel. *Phase Cycling and Field Gradient Pulses for Coherence Selection in NMR*. [Online] Department of Biochemistry, University of Cambridge, July 17, 2007. [http://www.nmr2.buffalo.edu/resources/edu/matr/DN\\_HandoutGrad.pdf](http://www.nmr2.buffalo.edu/resources/edu/matr/DN_HandoutGrad.pdf).



31. *Improved method for accurate and efficient quantification of MRS data with use of prior knowledge.* Vanhamme L., van den Boogaart A., Van Huffel S. I, 1997, *Journal of Magnetic Resonance*, Vol. 129, pp. 35–43.
32. *Simulation of coupled-spin systems in the steady-state free-precession acquisition mode for fast magnetic resonance (MR) spectroscopic imaging.* Z Starcuk Jr, J Starcukova, O Strbak and D Graveron-Demilly. 10, 2009, *Meas. Sci. Technol.* , Vol. 20.
33. *Time-domain semi-parametric estimation based on a metabolite basis set.* H. Ratiney, M. Sdika, Y. Coenradie, S. Cavassila, D. van Ormondt and D. Graveron-Demilly. 1, 2005, *NMR in Biomedicine*, Vol. 18, pp. 1-13.
34. *Computer Simulations in Magnetic Resonance. An Object Oriented Programming Approach.* S.A. Smith, T.O. Levante, B.H. Meier, and R.R. Ernst, J. I, 1994, *Journal of Magnetic Resonance, Series A*, Vol. 106, pp. 75-105.
35. *Analysis of eddy currents in nuclear magnetic resonance imaging.* Cho C., B. Ahn and Z. H. I, 1991, *Magnetic Resonance in Medicine*, Vol. 17, pp. 149-163.
36. *Spline interpolation.* [Online] [https://en.wikipedia.org/wiki/Spline\\_interpolation](https://en.wikipedia.org/wiki/Spline_interpolation).
37. Bertolazzi, Enrico. *Unconstrained minimization Lectures for PhD course on Numerical optimization.* Trento : DIMS – Università di Trento, 2011.
38. William H. Press, Saul A. Teukolsky, William T. Vetterling, Brian P. Flannery. *NUMERICAL RECIPIES: The Art of Scientific Computing, Third Edition.* Cambridge University Press, 2007.
39. *MR Subcommittee Task Group 1. Acceptance Testing and Quality Assurance Procedures for Magnetic Resonance Imaging Facilities.* AAPM report n°100. American Association of Physicists in Medicine, December 2010.
40. *Characterization of prostate cancer using T2 mapping at 3 T: A multi-scanner study.* A. Hoang Dinh, R. Souchon, C. Melodelima, F. Bratan, F. Mège-Lechevallier, M. Colombel and O. Rouvière. 4, 2014, *Diagnostic and Interventional Imaging*, Vol. 96, pp. 365-372.
41. *Quantitative 1H MR Spectroscopic Imaging of the Prostate Gland Using LCModel and a Dedicated Basis-Set: Correlation with Histologic Findings.* M. L. García-Martín,

*M. Adrados, M. P. Ortega, I. Fernández González. 2011, Magnetic Resonance in Medicine, Vol. 65, pp. 329–339.*

*42. Characterization of the measurement error structure in 1D <sup>1</sup>H NMR data for metabolomics studies. Tobias K. Karakacha, Peter D. Wentzellb, John A. Waltera. 2009, Analytica Chimica Acta, Vol. 636, pp. 163-174.*

*43. Error Analysis and Propagation in Metabolomics Data Analysis. Moseley HN, 2013, Computational and Structural Biotechnology Journal, Vol. 4, pp. 1-12.*

*44. Prostate Cancer Metabolite Quantification Relative To Water In <sup>1</sup>H-MRSI In Vivo At 3 Tesla. Mary A. McLean, Tristan Barrett, Vincent J. Gnanapragasam, Andrew N. Priest, Ilse Joubert, David J. Lomas, David E. Neal, John R. Griffiths, and Evis Sala. 4, 2011, Magnetic Resonance in Medicine, Vol. 65, pp. 914–919.*

*45. Keeler, James. Understanding NMR Spectroscopy. University of Cambridge, Department of Chemistry : Keeler, James, 2004.*

## RINGRAZIAMENTI

Non è facile stilare una lista di tutte le persone che vorrei ringraziare per la realizzazione di questo lavoro, tra quelle che hanno contribuito materialmente al progetto e tutte quelle che mi hanno aiutato a riprendermi dopo i mesi passati tra letto ed ospedale, a causa della malattia che mi colpì ormai più di un anno fa.

In primo luogo vorrei ringraziare i miei genitori Gianni e Gabriela per avermi sempre assistito nei momenti più difficili e per avermi fornito i mezzi necessari per conseguire i miei studi fuori sede. Ringrazio la mia fidanzata Chiara, per avermi sempre aiutato con il suo amore e la forza d'animo che la contraddistingue, e i suoi genitori Marco e Carla per avermi sempre fatto sentire a casa da loro. Un grazie speciale va a tutta la mia famiglia: mia sorella Lucia, la mia nonna Gina, i miei zii Sergio, Barbara, Stefano, Maddalena e le mie cugine Carlotta e Costanza.

Ringrazio il Prof. Romano Zannoli che mi ha sempre motivato e supportato sia nella malattia, sia nel percorso di tesi, dandomi preziosi consigli per lo svolgimento del mio lavoro e per il mio futuro. Ringrazio il Dott. David Bianchini per avermi dato modo di svolgere tutto il lavoro di tesi in un istituto prestigioso come l'IRST e per la fiducia che ha sempre dato alle mie idee e proposte. Ringrazio il Dott. Francesco Marcocci per il supporto tecnico nelle misure ma soprattutto per le conoscenze che mi ha trasmesso nel campo dell'NMR. Ringrazio il Dott. Vincenzo D'Errico per avermi fatto compagnia nelle ore di lavoro in ufficio e per avermi insegnato nuove terminologie come "stilita" ed "artato". Un ringraziamento sentito va a tutti gli altri fisici dell'IRST: Anna, Enrico, Emilio ed il Prof. Benassi che mi hanno sempre aiutato e trattato come un loro pari durante i mesi di tirocinio. Ringrazio anche tutti i tecnici, in particolare Alex, Giamba e Francesco, con i quali spesso ho trascorso delle pause al bar a prendere un ottimo caffè "chinato". Ringrazio Sara e gli altri biologi del laboratorio che mi hanno permesso di usufruire delle loro attrezzature per la realizzazione dei fantocci.

Un ringraziamento va certamente all'ospedale di Perugia e specialmente al reparto di ematologia, per il percorso di terapia che mi ha permesso di riprendermi dalla malattia e di poter poi svolgere il lavoro di tesi; in particolare un immenso grazie al Dott. Flenghi,

alla Dott.ssa Bonifacio ed al Prof. Falini che tuttora mi seguono nei controlli periodici. Ringrazio anche la Prof.ssa Aristei e tutto il reparto di radioterapia oncologica.

Ringrazio gli amici di Perugia: Andrea G., Andrea R., Alfredo, Filippo, Lucrezia, Elisa, Alessandro, Aurora, Sara, Gabu, Lorenzo B., Daniele, il Nik, Matteo e specialmente il mio amico d'infanzia Dario per essermi sempre stato vicino da ventuno anni a questa parte.

Ringrazio i miei cari amici della triennale, Raffaele, Nia, Saida, Francesco e Manu.

Un grazie speciale va poi a tutti i membri dei Lumberjack: Andrea, Guido, Danny e Rod, per quello che mi hanno dato da amici veri e per la musica fatta insieme, con la speranza di completare il demo in ottobre.

Grazie agli amici di Bastia: Pietro, Marco, Luca, Daniele, Paolino e a tutti gli altri amici del fantacalcio.

Ringrazio tutti gli amici di Bologna, in primo luogo il mio compagno di studi di sempre Andrea C., la sua ragazza Sara e Giacomo. Un grazie ai compagni di corso: Francesca, Nicola, Daniele, Francesco, Celeste, Manami, Arianna, Laura, Mariagrazia e tutti gli altri colleghi della magistrale. Un grazie al gruppo della Champions League, in particolare a Luca e Richi per tutte le sciabolate di Piccinini che abbiamo sentito insieme. Infine ringrazio con affetto i miei coinquilini Giulio, Luca e soprattutto Pio con cui ho passato dei bellissimi anni nella casa di Via del Borgo di San Pietro.